Università degli Studi di Bergamo
Facoltà di Ingegneria
Dipartimento di Ingegneria Industriale

Dottorato in Tecnologie per l'Energia e l'Ambiente
XX ciclo

Higher Order Discontinuous Galerkin Methods for the Navier-Stokes Equations

Nicoletta Franchina

Supervisor

Prof. Francesco BASSI

February 2008

Acknowledgements

Great thanks first of all to Professor Francesco Bassi for the fruitful collaboration, many interesting discussions and advices are to be mentioned along with the support provided. The time dedicated to implementation issues, trials and reflections on different subjects has surely been really valuable.

I am also grateful to Professor Stefano Rebay for the help during the work we carried on together, for the hours spent trying to develop new ideas and coding, for the quantity of information, comments and suggestions I got.

Many thanks to Andrea Crivellini, Pierangelo Conti, Antonio Ghidoni for their effective collaborations and for their helpfullness for the realization of the overall work during these years.

Special thanks to my dear father and mother, and even to my brother for their considerable, unvaluable support through all these years, the nonesuch patience and understanding they have shown and that I sometimes risked neither to resognise. Precious moments spent along with my dear friends Francesca and Fabrizio can not be forgotten. During this years course funny moments have not been to be asked, they came on their own, as this regards an unforgettable thought to 'Asking'.

This work is dedicated to all these important people to me.

The sponsorship within the European project *ADIGMA*, 'Adaptive Higher-Order Variational Methods for Aerodynamic Applications in Industry', for the definition of higher order schemefor hybrid grids, is also acknowledged.

Abstract

This thesis is devoted to the achievement of numerical methods for the solution of the Navier-Stokes equations, both compressible and incompressible, for fluid dynamics applications. The main objective has been to establish a fair trade-off between the accuracy requirement and the computational cost, since although the higher resolution methodologies can proven to supply advantages as regards the quality of the solution provided, in fact they are often claimed to be excessively costly.

This work can be divided into two parts. First we present the implementation of a *spectral* discontinuous Galerkin methods for the compressible Navier-Stokes set. The co-location strategy in gaussian nodes along with the tensorial computation of the approximating functions has been implemented, for an effective assembly of the discrete operators. This approach has also been joined with a *p-multigrid* method achieving an overall quite interesting performance enhancement. An extensive numerical validation is provided in order to investigate both the accuracy and the efficiency of the scheme.

The second part is dedicated to the solution of the incompressible Navier-Stokes equations. A new semi-implicit algorithm has been devised through a procedure of minimization of the *implicitness* level necessary to achieve the solvability of the problem. Such an aim required to additively split the system to outline and distinguish the implicitly considered parts from those evaluated explicitly. This scheme clearly takes advantage in term of the memory requirement.

Contents

List of Figures

List of Tables

Chapter

1 Introduction

Computational fluid dynamics methods are currently employed in a wide variety of fields as a powerful tool to perform design, optimization and prediction. The basic idea in numerics is to transform the continuum field to a finite discrete one and to solve the approximating problem by means of a calculator. The kind of conditions we try to satisfy in order to implement such a procedure defines the method itself. The quality of the discretization can be evaluated either by theoretical means or numerical assessments, two properties that allow the characterization of a scheme are the accuracy and the stability. The former feature defines the rate of change of the error for a refinement process, therefore it indicates how well the solution has been computed, the latter is instead worth to tell if possible oscillations can be controlled or they otherwise can cause the blow up of the computation.

The modelization of a certain phenomenon requires first of all the deep understanding of its physical behaviour and at this aim the transport and transfer mechanisms are of main importance to express the conservation or the changes of relevant quantities, such as the mass, the momentum and the energy. 'Practical problems in which convection plays an important role arise in many applications as diverse as meteorology, weather-forecasting, oceanography, gas dynamics, turbomachinary, turbulent flows, granular flows, oil recovery simulation, modeling of shallow waters, transport of contaminant in porous media, viscoelastic flows, semiconductor device simulation, magnetohydrodynamics, and electro-magnetism, among many others. This is why devising robust, accurate and efficient methods for numerically solving these problems is of considerable importance'. Another important mechanism involved in the fluid motion description process is that of diffusive kind, as the mean towards the homogeneity of the considered field.

This work is devoted to the resolution of the Navier-Stokes equations, both compressible and incompressible, for fluid dynamics applications. Therefore we devote the next sections of this introducing chapter to the presentation of all the ingredients necessary to achieve the approximated solution of this problem. In detail we first recall the governing equations, partially follow-

ing the [44], then we define the main features characterizing the numerical schemes in use, the finite volume approach, the finite element method and the spectral method, with particular attention to our solution strategy.

1.1 Navier-Stokes Equations

The Navier-Stokes (NS) equations are the governing partial differential equations for the motion af many fluids, they entail the conservation principle for the mass, the momentum and the energy; in differential conservative form they read:

$$\begin{aligned} \frac{\partial \rho \mathbf{u}}{\partial t} + \mathrm{div}(\rho \mathbf{u} \otimes \mathbf{u}) &= \mathrm{div}\boldsymbol{T} + \rho \boldsymbol{f} \\ \frac{\partial \rho}{\partial t} + \mathrm{div}\rho \mathbf{u} &= 0 \\ \frac{(\rho e + \frac{1}{2}\rho|\mathbf{u}|^2)}{\partial t} + \mathrm{div}\Big[\Big(\rho e + \frac{1}{2}\rho|\mathbf{u}|^2\Big)\mathbf{u}\Big] &= \mathrm{div}(\boldsymbol{T}\cdot\mathbf{u}) - \mathrm{div}\boldsymbol{q} + \rho \boldsymbol{f}\cdot\mathbf{u} + \rho r. \end{aligned} \tag{1.1.1}$$

The $\mathbf{u}$ denotes the velocity of the fluid, ρ its density, e its internal energy per unit of mass, $\mathbf{u}\otimes\mathbf{u}$ the tensor $\{u_i u_j\}$, $\boldsymbol{T} = \boldsymbol{T}(\mathbf{u}, \hat{p})$ the stress tensor, $\hat{p}$ the pressure, $\boldsymbol{q} = \boldsymbol{q}(\theta)$ the heat flux, θ the absolute temperature and finally $\boldsymbol{f}$ and r stand for the external force field per unit mass and for the heat supply per unit mass per unit time. The behaviour of any particular fluid is characterized by its constitutive law:

$$\begin{aligned} T_{ij} &= \Big[-\hat{p} + \Big(\zeta - \frac{2\mu}{d}\Big)\mathrm{div}\mathbf{u}\Big]\delta_{ij} + 2\mu D_{ij} \\ \boldsymbol{q} &= \chi \nabla\theta, \end{aligned} \tag{1.1.2}$$

where $\boldsymbol{D} = \boldsymbol{D}(\mathbf{u})$ is the deformation tensor whose components are given by

$$D_{ij} = \frac{1}{2}(D_j u_i + D_i u_j),$$

μ and ζ are the shear and the bulk viscosity coefficients respectively and χ the heat conductivity coefficient while the δ_{ij} defines the Kronecker tensor. Alternatively the system (1.1.1) can be written in non-conservative formulation, by exploiting the mass equation also known as continuity we can write

$$\begin{aligned} \rho\Big[\frac{\partial \mathbf{u}}{\partial t} + \mathbf{u}\cdot\boldsymbol{\nabla}\mathbf{u}\Big] &= \boldsymbol{\nabla}\boldsymbol{T} + \rho\boldsymbol{f} \\ \rho\Big[\frac{\partial e}{\partial t} + \mathbf{u}\cdot\boldsymbol{\nabla}e\Big] &= \boldsymbol{T} : \boldsymbol{D} - \boldsymbol{\nabla}\cdot\boldsymbol{q} + \rho r \end{aligned} \tag{1.1.3}$$

with $\boldsymbol{T} : \boldsymbol{D} = \sum_{i,j=1}^{d} T_{ij} D_{ij}$. Either the system (1.1.1) or the (1.1.3) can be closed by means of thermodynamic principles which result to depend on the compressibility level of the fluid, therefore we proceed on distinguishing between compressible and incompressible flows.

1.1.1 Compressible Flows

The following state equations can be used if the density ρ and the temperature θ are chosen to be the unknowns

$$\begin{aligned} &\widehat{p} = P(\rho, \theta) \\ &e = E(\rho, \theta) \\ &\mu = \mu^*(\rho, \theta), \quad \zeta = \zeta^*(\rho, \theta), \quad \xi = \xi^*(\rho, \theta), \end{aligned} \tag{1.1.4}$$

where $P, E, \mu^*, \zeta^*, \xi^*$ are known functions subjected to the thermodinamic restrictions called Clausius-Duhem inequalities,

$$\mu^* \geq 0, \quad \zeta^* \geq 0, \quad \xi^* \geq 0.$$

From the well-known relation

$$\mathrm{d}E = \theta \, \mathrm{d}S - P \, \mathrm{d}(\rho^{-1}),$$

with S defining the specific entropy, we have that E and P must satisfy the compatibility condition

$$E_\rho = \rho^{-2}(P - \theta P_\theta),$$

the subscripts define the partial derivatives with respect the indicated variable.

1.1.2 Incompressible Flows

The incompressibility feature requires that any quantity of fluid does not change its volume during time along the motion, namely

$$\operatorname{div} \mathbf{u} = 0, \tag{1.1.5}$$

as it can be observed from the mass conservation entailed by the second equation of the system (1.1.1). The pressure is no more related to thermodynamic unknowns and therefore it can be computed through the momentum equation, meantime the thermodynamic relations are the followings

$$e = E(\theta), \quad \mu = \mu^*(\theta), \quad \chi = \chi^*(\theta). \tag{1.1.6}$$

The Navier-Stokes equations under the incompressibility requirement read as follows

$$\begin{aligned} \mathrm{div}\mathbf{u} &= 0 \\ \rho\Big[\frac{\partial \mathbf{u}}{\partial t} + (\mathbf{u}\cdot\nabla)\mathbf{u}\Big] &= -\nabla\hat{p} + \sum_{j=1}^{d} D_j(\mu^* D_j\mathbf{u} + \mu^*\nabla u_j) + \rho\boldsymbol{f} \\ \rho E_\theta\Big(\frac{\partial \theta}{\partial t} + \mathbf{u}\cdot\nabla\theta\Big) &= \frac{\mu^*}{2}\sum_{i,j=1}^{d}(D_i u_j + D_j u_i)^2 + \mathrm{div}\chi^*\nabla\theta + \rho r. \end{aligned} \tag{1.1.7}$$

The problem must clearly be endowed of the suitable initial and boundary conditions, which are to be constrained as the equation (1.1.5) suggests. On solid walls the velocity is usually imposed to be zero, the so called *no-slip* condition which provides a mechanism for the boundary to introduce vorticity in the fluid.
The solution of the incompressible Navier-Stokes equations is inherently more complicated than that of the compressible version, the difficulty is mainly due to the continuity constraint which couples the velocity and the pressure field. The equations are of incomplete parabolic kind with an elliptic part which causes the instantaneous transmission of pressure signals through the whole domain. In addition many phenomena, such as reverse flow, large gradient in p and $\mathbf{u}$ near sharp corners, inherent instability at very high Reynolds (Re) number, can occour increasing the complexity of the motion and the computational cost of the algebraic problem associated to the NS system itself.

1.2 Numerical Methods

The main peculiarities of some numerical methods are here recalled, in particular we consider the finite volume method (FVM), the finite element method (FEM), the spectral element method (SEM) and finally the main protagonist of this thesis, the discontinuous finite element method by a Galerkin approach.

1.2.1 Finite volume method

The finite volume method is the numerical resolution approach which shows the most physical point of view among those presented. The solution is

defined as the mean value assumed by the variable in each element of the discretized domain Ω_h. For the sake of presentation we consider a simple hyperbolic equation in divergence form

$$\frac{\partial u}{\partial t} + \boldsymbol{\nabla} \cdot f(u) = 0 \tag{1.2.1}$$

with f defining the flux vector related to the equation in exam. The relaxation of the continuity requirement is a typical procedure adopted in order to reach solutions that could not be otherwise computed. This weakening of the equations is got by means of the Green divergence theorem, which performs a reduction of the order of the maximum derivative of the discrete problem. This process provides the so called *weak* form of the equations which is obtained just by their multiplication by a suitably chosen test function ϕ and integrating by parts the resulting equation,

$$\int_\Omega \frac{\partial u_h}{\partial t} \, \mathrm{d}\mathbf{x} + \int_{\partial\Omega} \widehat{f}_n(u_h) \, \mathrm{d}\sigma = 0. \tag{1.2.2}$$

The exact solution u is then replaced by the discrete u_h taken to be a piecewise constant function inside each element. The normal numerical flux function $\widehat{f}_n(u_h)$ used in place of the physical flux defines the value to be imposed on the boundary of each element. The computation of this vector resorts to the solution of a Riemann problem, either exact or approximated. The physical relevant solution, called the entropy solution since it is obtained by means of the satisfaction of an entropy condition, can be achieved only by monotone schemes which are but first order accurate. The higher order representations require the use of reconstruction procedures and of flux or slope limiters to cure the generation of spurious oscillations around discontinuities, in fact a quite cumbersome, if not difficult, procedure to implement.

1.2.2 Finite element methods

The finite element method originally developed for structural mechanic applications has been successively also extendend to fluid dynamics. In this kind of discretization the numerical solution is assumed to be expressed by a finite number of functions of local nature. The appealing related to such a kind of methods is also due to the mathematical foundation of which they are endowed of. As a matter of fact the finite element methods have recognised as a form of the Rayleigh-Ritz problem, as it resorts to a finite number

of global functions to perform the approximation $u(x) = \sum_{i=1}^{N} q_i \phi_i(x)$. The weights q_i are the unknown to be computed in order to somehow minimize the error associated to the discrete problem to be solved. The presentation of the finite element methods following a Galerkin approach can be led starting from the weighted residual formulation. At this purpose we consider a linear differential equation,

$$\mathbb{L}(u) = 0, \quad \text{in } \Omega \tag{1.2.3}$$

provided of suitable boundary and initial conditions whose exact solution u_e is approximated by the following expansion

$$u_h = u_0(\mathbf{x}, t) + \sum_{i=1}^{\text{Ndof}} \widehat{u}_i(t)\phi_i(\psi), \tag{1.2.4}$$

where the ϕ_i-s are called *trial* or *expansion* functions and $\widehat{u}_i$ the unknown Ndof coefficients. Ndof defines the number of the degrees of freedom necessary to span the space accomodating the solution, the value u_0 accounts instead for the initial data. The substitution of the numerical solution inside the original problem (1.2.3) gives a non-zero residual

$$\mathbb{L}(u_h) = R(u_h), \tag{1.2.5}$$

the required coefficients are searched as the values that minimize the inner product of the residual itself tested against a *weight* function v,

$$(v_j(\mathbf{x}), R) = 0, \quad j = 1, ..., \text{Ndof}, \tag{1.2.6}$$

in the limit of the u_h approaching the exact solution u_e, the residual goes to zero. The choice of the expansion functions $\phi_i(\mathbf{x})$ and of the test function $v_j(\mathbf{x})$ determines the kind of the method, in particular the Bubnov-Galerkin methods are recovered for trial and test functions chosen to be one another coincident. A broader class of the Galerkin method known as Petrov-Galerkin method uses only similar test and trial functions.

Finite element Definitions

Some finite element definitions which can be advised as the building blocks of such a kind of methods are here provided in accordance with Ciarlet, see [12].

Definition 1 (FE) *A finite element is defined as a triplet* $\{K, P, \Sigma\}$ *where:*

- K *is a compact, connected, Lipschitz subset of* $\mathbb{R}^d$ *with non-empty interior*

- P *is a vector space of functions* $p : K \to \mathbb{R}^m$ *for some positive integer* m, $m = 1$ *or* $m = d$.

- Σ *is a set of linearly indipendent linear forms* ϕ_i, $1 \leq i \leq N$ *defined over the space* P. *The set* Σ *is* P*-unisolvent: given any real scalar* α_i *there exists a unique function* $p \in P$ *such that* $\phi_i(p) = \alpha_i$. *The linear forms* ϕ_i *are called the local degree of freedom of the element, while* p_i *are the basis functions of the element.*

We consider a bounded domain Ω with a Lipschitz-continuous boundary which is approximated by a computational domain Ω_h whose boundary is taken to be piecewise-polynomial.

Definition 2 (FE mesh) *The set* $\{K_1, K_2, .., K_n\}$ *over a domain* Ω_h *with a piecewise-polynomial boundary defines a geometrical division of* Ω_h *into a finite number of non-overlapping open polygonal cells* K_i *such that*

$$\Omega_h = \bigcup_{i=1}^{n} \bar{K}_i.$$

Each cell K_i *has a polynomial order* p_i.

Definition 3 (Finite element interpolant) *Given a unisolvent finite element* (K, P, Σ), *let* $\mathcal{B} = \{\varphi_1, \varphi_2, .., \varphi_n\}$ *be the basis that spans the space* P. *Let* $v \in V$, *where* $P \subset V$, *be a function for which the linear forms* $\phi_1, \phi_2, .., \phi_n$ *are defined. We define the local interpolant as*

$$\mathcal{I}_K(v) = \sum_{i=1}^{n} \phi_i(v)\varphi_i. \tag{1.2.7}$$

From the linearity of the forms ϕ_i *it follows the linearity of the interpolation operator* $\mathcal{I}_K(v)$.

1.2.3 Spectral element methods

Global spectral methods use a unique representation of the numerical solution in the domain by means of a truncated series expansion,

$$u(x) \approx u_{\mathrm{N}}(x) = \sum_{n=0}^{N} \widehat{u}\, \phi_n. \tag{1.2.8}$$

The basical strategy can be summarized through these two steps: first the substitution of the approximation u_{N} into the original equation suitably manipulated, then the minimization of the residual is still to be entailed. Pseudo-spectral collocation and modal Galerkin methods have been elaborated in this framework. The spectral collocation applied to the problem (1.2.3) requires to look for a function u_{N} supposed mainly to be of polynomial kind, such that

$$\mathbb{L}_{\mathrm{N}} u_{\mathrm{N}} = 0 \quad \text{at } x_i \in \Omega,$$

where the x_i are the collocation points in which the unknown field is to be computed; the Gauss-Lobatto set is the classical choice. The $\mathbb{L}_{\mathrm{N}}$ is the discrete counter-part of the operator $\mathbb{L}$, obtained by replacing any derivative by the pseudo-spectral derivative, namely the derivative of the interpolant computed at the nodes x_i.

The key feature of these schemes is the exponential convergence they provide, also called *spectral* convergence. This property requires the solution to be smooth enough and the same must be true even for the domain. The spectral element method introduced by Patera [] joined the finite element method peculiarities with those related to spectral element method into an hybrid scheme: higher order polynomials within each element and convergence got by either *p*-type or *h*-type refinement or both. The comparison between standard finite element and spectral *hp* element, see *e.g.* [20], shows that the latter achieves an exponential convergence in the polynomial order, although observed only when the solution is captured spatially. This result comes along with an error per unit of computational work smaller than that associated to the finite element approach itself. Hence if we need high accuracy the spectral *hp* strategy it allows to get it at a lower cost, as Sherwin and Karniadakis extensively show in their works, *e.g.* see [31], [46].

1.2.4 Discontinuous Galerkin methods

The discontinuous element methods was originally introduced by Reed and Hill in 1973 and successively analyzed by Lesaint and Raviart for the solution of the linear neutron transport equation. This method has received by now the attention of many people either belonging to the mathematical field or to the computational one because of some peculiarities we are going to outline. DG methods join the key features of the finite volume methods with those related to the finite element methods, from the latter the accuracy achievement has been mutuated. This valuable property is obtained by using high-order polynomial functions within each element to approximate the solution field, a quite easy procedure to implement especially in view of the not trivial interpolation on wider stencil typical of the FVM. On the other hand DG mantains the discontinuous functional representation as the finite volume approach does, this leads to the boundary treatment through the numerical fluxes and the resolution of a Riemann problem, this endows the method of the physical upwinding. Therefore such a scheme is particularly suitable for the accurate resolution of hyperbolic problems, although meantime the application of this discontinuous treatment to the elliptic part of the NS equations has not been so straighforward to get. The truly accomodation of this second order operator into the discontinuous approximation space is due to the work of Bassi and Rebay [3] who made a 'breakthrough in the framework of the compressible Navier-Stokes equations', [16]. The way this result has been achieved is presented in the next chapter, here we limit ourselves to briefly introduce the DG method approach for the NS system solution. Take the conservative form of the problem, the two dimensional case is here considered for semplicity,

$$\frac{\partial \mathbf{u}}{\partial t} = \boldsymbol{\nabla} \cdot \boldsymbol{\mathcal{F}}_c(\mathbf{u}) - \boldsymbol{\nabla} \cdot \boldsymbol{\mathcal{F}}_v(\mathbf{u}, \boldsymbol{\nabla}\mathbf{u}) = 0, \tag{1.2.9}$$

with $\boldsymbol{\mathcal{F}}_c(\mathbf{u})$ defining the convective flux vector and $\boldsymbol{\mathcal{F}}_v(\mathbf{u}, \boldsymbol{\nabla}\mathbf{u})$ the viscous flux. Their components can be obtained by comparison with the system (1.1.1), in particular the unknown vector and the convective flux vector componentwise read as follows

$$\mathbf{u} = \left\{ \begin{array}{c} \rho \\ \rho u \\ \rho v \\ \rho e \end{array} \right\}, \quad \boldsymbol{\mathcal{F}}_{\mathbf{c,x}} = \left\{ \begin{array}{c} \rho u \\ \rho u^2 + p \\ \rho vu \\ \rho hu \end{array} \right\}, \quad \boldsymbol{\mathcal{F}}_{\mathbf{c,y}} = \left\{ \begin{array}{c} \rho v \\ \rho uv \\ \rho v^2 + p \\ \rho hv \end{array} \right\}, \tag{1.2.10}$$

while for the viscous vector $\boldsymbol{\mathcal{F}}_v$ we have

$$\boldsymbol{\mathcal{F}}_{\mathbf{v},\mathbf{x}} = \left\{ \begin{array}{c} 0 \\ 2u_x + \lambda(u_x + u_y) \\ v_x + u_y \\ u[2u_x + \lambda(u_x + u_y)] + v(v_x + u_y) + \gamma/\mathrm{Pr}\, e_x \end{array} \right\}, \qquad (1.2.11)$$

$$\boldsymbol{\mathcal{F}}_{\mathbf{v},\mathbf{y}} = \left\{ \begin{array}{c} 0 \\ v_x + u_y \\ 2v_x + \lambda(u_x + v_y) \\ u(v_x + u_y) + v[2v_y + \lambda(u_x + v_y)] + \gamma/\mathrm{Pr}\, e_y \end{array} \right\}, \qquad (1.2.12)$$

where Pr stands for the Prandtl number, γ for the ratio between the specific heats of the fluid, $h = e + p/\rho$ and $p = (\gamma - 1)\rho[e - (u^2 + v^2)/2]$. Multipling the equation (1.2.9) by a *test* function $\mathbf{v}$ we get the weighted residual formulation,

$$\int_\Omega \mathbf{v} \frac{\partial \mathbf{u}}{\partial t}\, \mathrm{d}\mathbf{x} + \int_\Omega \mathbf{v}\, \boldsymbol{\nabla} \cdot \boldsymbol{\mathcal{F}}(\mathbf{u}, \boldsymbol{\nabla}\mathbf{u})\, \mathrm{d}\mathbf{x} = 0, \qquad \forall \mathbf{v} \qquad (1.2.13)$$

and integrating it by parts, element by element in view of the discontinuous treatment, we obtain the weak formulation

$$\sum_{K \in \mathcal{T}} \int_K \mathbf{v} \frac{\partial \mathbf{u}}{\partial t}\, \mathrm{d}\mathbf{x} + \sum_{K \in \mathcal{T}} \int_{\partial K} \mathbf{v} \boldsymbol{\mathcal{F}}(\mathbf{u}, \boldsymbol{\nabla}\mathbf{u}) \cdot \boldsymbol{n}\, \mathrm{d}\sigma - \sum_{K \in \mathcal{T}} \int_K \boldsymbol{\nabla}\mathbf{v} \cdot \boldsymbol{\mathcal{F}}(\mathbf{u}, \boldsymbol{\nabla}\mathbf{u})\, \mathrm{d}\mathbf{x} = 0. \qquad (1.2.14)$$

The discrete form of the (1.2.14) is then achieved by substituting the exact solution with an approximation of polynomial kind like that provided by the relation (1.2.7) in Def. 3, without global continuity requirements, as

$$\int_K \mathbf{v}_h \frac{\partial \mathbf{u}_h}{\partial t}\, \mathrm{d}\mathbf{x} + \int_{\partial K} \mathbf{v}_h \widehat{\boldsymbol{\mathcal{F}}}(\mathbf{u}_h, \boldsymbol{\nabla}\mathbf{u}_h) \cdot \boldsymbol{n}\, \mathrm{d}\sigma - \int_K \boldsymbol{\nabla}\mathbf{v}_h \cdot \boldsymbol{\mathcal{F}}(\mathbf{u}_h, \boldsymbol{\nabla}\mathbf{u}_h)\, \mathrm{d}\mathbf{x} = 0, \qquad (1.2.15)$$

for each element K belonging to the triangulation $\mathcal{T}_h$. The numerical flux $\widehat{\boldsymbol{\mathcal{F}}}$ has been introduced to establish the coupling between adjacent elements that would be otherwise completely missing and moreover to weakly prescribe the boundary conditions. The choice of this vector resorts to different ideas either the inviscid or the viscous part is considered, more details on this and on the numerical flux properties in the devoted following chapter.

The distinguishing features of DG methods are closely related to the discontinuous functional approximation of the solution itself, in particular these

schemes are characterized by an high degree of locality, each element interchanges information only with a limited number of neighbouring elements. The discontinuous representation allows to use different order of approximation for adjacent elements or to use non-conforming mesh with hanging nodes with no difficulty, therefore the *hp* adaptivity can be exploited quite directly. The greatest geometrical flexibility and the easy handling of complex geometries and boundaries are appealing and valuable properties of discontinuous methods that prompted a lot of studies and interest towards them. In addition the discrete formulae are very compact and this aspect can lead to the easy implementation of implicit and parallel code. DG schemes are also known for their robustness. Unfortunately this strategy is not without weak points, the computational cost is often claimed to be the serious limit to its development. Further understanding and details on DG methods can be found *e.g.* in [2], [4]-[6], [13]-[15] and many more works not cited here.

1.3 Outline

This work can be ideally divided into two main parts, the first is the implementation of an higher order DG code for the solution of the compressible Navier-Stokes equations, while the second part is related to the definition of a new semi-implicit algorithm for the solution of the incompressible set. We focused on the achievement of accurate results along with a computation as efficient as possible, in order to mitigate the unconvenience refered precedingly. Detailing the remainder of this thesis we have that the second chapter is devoted to the description of our DG method applied to the NS system, the chapter three deals with the definition of highly accurate solution in effective way. A spectral DG scheme has been devised, both the classical collocation approach and a variant accomplish the result; numerical assessments are presented. Chapter four is instead the summary of the work we did for the solution of the incompressible NS system, a first part for the sake of the introduction of the existing strategies mainly based on the splitting of the pressure-velocity fields computation. After this acknowledgement the semi-implicit algorithm is described together with numerical tests. Finally the conclusions related to the overall work.

Chapter

2 DG method for the NS eqs

Discontinuous Galerkin methods originally developed for advective problems have been successively extended to advection-diffusion cases and even to pure elliptic problems. In the following the compressible Navier-Stokes system, written in conservative form as in the (1.2.9), is considered and discretized in accordance to our DG finite element method. The presentation is performed accounting first for the inviscid part and secondarily for the viscous contribution. The end of chapter is reserved to the DG scheme application to the incompressible NS equations, INS.

2.1 The inviscid Navier-Stokes equations

We move from the inviscid part of the Navier-Stokes equations written in compact conservative form

$$\frac{\partial \mathbf{u}}{\partial t} + \mathrm{div}\boldsymbol{f}_c(u) = 0, \tag{2.1.1}$$

suitably endowed with boundary and initial conditions. The weak form is reported below

$$\int_K v\frac{\partial \mathbf{u}}{\partial t}\,\mathrm{d}\mathbf{x} - \int_K \boldsymbol{\nabla} v \cdot \boldsymbol{f}_c\,\mathrm{d}\mathbf{x} + \int_{\partial K} v\boldsymbol{f}_c(u^*)\cdot\boldsymbol{n}\,\mathrm{d}\sigma = 0 \quad \forall v, \tag{2.1.2}$$

for each element $K \in \Omega$. Since we approximate the solution by means of a piecewise function with no global continuity requirements, we need to compute a value u^* that eliminates the ambiguity due to the double value on each interface. The coupling between adjacent elements, that would be otherwise completely missing, is established by means of a numerical flux vector $\hat{f}_c$. Its value depends on the internal interface state u^-, on the neighboring element interface state u^+, also called external, and on the normal direction, $\hat{f}_c = \hat{f}_c(u^-, u^+; \boldsymbol{n})$. Boundaries are treated exactly as internal faces with the external data replaced by the conditions to be entailed, the BCs are refered to be weakly prescribed. This flux vector can be computed starting from

physical consideration of upwinding, therefore any flux function used in the upwind finite volume methods can be exploited. Many choices are available, among them we recall the Godunov, the Engquist-Osher, the Lax-Friedrichs, and the Van Leer flux functions. The discontinuous formulation can be obtained as follows; consider the functional space

$$V_h := \{v \in L^{d+2}(\Omega_h) : v|_e \in \mathbb{P}^k(e)\ \forall e \in \mathcal{T}_h\}, \tag{2.1.3}$$

where $\mathbb{P}^k(e)$ is the space of polynomial functions of degree at most k in each element e and $\mathcal{T}_h = \{e\}$ the triangulation of the discrete $d-$dimensional domain Ω_h. Assume the test and the expansion basis to be chosen inside V_h, coincident one another, therefore the DG discretization of (2.1.2) is then given by

$$\sum_{e\in\mathcal{T}_h}\int_{\Omega_e} v_h\frac{\partial u_h}{\partial t}\,\mathrm{d}\mathbf{x} - \sum_{e\in\mathcal{T}_h}\int_{\Omega_e}\boldsymbol{\nabla} v_h\cdot\boldsymbol{f}_c(u_h)\,\mathrm{d}\mathbf{x} + \sum_{e\in\mathcal{T}_h}\int_{\partial\Omega_e} v_h\hat{f}_c(u_h^-,u_h^+;\boldsymbol{n})\,\mathrm{d}\sigma = 0, \tag{2.1.4}$$

for each test function $v_h \in V_h$. The summation over all the elements of the contour integrals in eq. (2.1.4) can be substituted with the summation over each interface, either of internal or boundary kind, as

$$\sum_{i\in\mathcal{I}_h}\int_{\Sigma_b}\left[v_h^-\hat{f}_c(u_h^-,u_h^+;\boldsymbol{n}^-) + v_h^+\hat{f}_c(u_h^+,u_h^-;\boldsymbol{n}^+)\right]\mathrm{d}\sigma + \sum_{b\in\mathcal{B}_h}\int_{\Gamma_i} v_h\boldsymbol{f}_c(u_h^*)\cdot\boldsymbol{n}\,\mathrm{d}\sigma, \tag{2.1.5}$$

where $\mathcal{I}_h$ and $\mathcal{B}_h$ denote the set of interface and boundary faces and Σ_h and Γ_h the corresponding geometrical locii. While the $(\cdot)^-$ and the $(\cdot)^+$ define the values of the trace of any quantity $(\cdot)$ evaluated on the two neighboring elements sharing the interface i, the u^* depends on the boundary data. The DG form of the Euler equation we are dealing with is finally reported joining the eq.s (2.1.4) and (2.1.5),

$$\begin{aligned}\int_{\Omega_e} v_h\frac{\partial u_h}{\partial t}\,\mathrm{d}\mathbf{x} - \int_{\Omega_e}\boldsymbol{\nabla} v_h\cdot\boldsymbol{f}_c(u_h)\,\mathrm{d}\mathbf{x} + \int_{\Sigma_h}(v_h^- - v_h^+)\hat{f}_c(u_h^+,u_h^-;\boldsymbol{n}^-)\,\mathrm{d}\sigma \\ + \int_{\Gamma_h} v_h\boldsymbol{f}_c(u_h^*)\cdot\boldsymbol{n}\,\mathrm{d}\sigma = 0 \qquad \forall v_h \in V_h.\end{aligned} \tag{2.1.6}$$

The convective numerical flux $\hat{f}_c$ adopted in the numerical tests presented in this work is the Godunov one, known to be the better strategy for non-linear

problems since it produces the smallest amount of artificial viscosity, even if the higher the order of approximation the lower the differences related to the various flux choices. We next describe the treatment of the viscous contribution.

2.2 Viscous part of the Navier-Stokes equations

The discontinuous discretization approach for both convection-diffusion and elliptic problems greatly resort to the work by Bassi and Rebay, (see [2], 1997). They reinterpreted the second order laplacian operator as a first order system and then they applied the discontinuous discretization technique to it, suitably accounting for the nature of the original operator. We report the main ideas with reference to the Helmoltz problem:

$$\begin{aligned} -\Delta u - \alpha u &= f \quad \text{in } \Omega, \\ u = u_b \quad \text{on } \Gamma^0, &\quad \partial_n u = \sigma_b \quad \text{on } \Gamma^n, \end{aligned} \tag{2.2.1}$$

let αu be a reaction term and $\Gamma^0 \cup \Gamma^n = \partial\Omega$ be the boundary of Dirichlet and Neumann kind respectively. The useful equivalent form of the (2.2.1) reads

$$\begin{aligned} \boldsymbol{\sigma} = \boldsymbol{\nabla} u, \quad u = u_b \quad \text{on } \Gamma^0 \\ -\boldsymbol{\nabla}\cdot\boldsymbol{\sigma} - \alpha u = f, \qquad \boldsymbol{\sigma}\cdot\boldsymbol{n} = \sigma_b \quad \text{on } \Gamma^n, \end{aligned} \tag{2.2.2}$$

with the auxiliary vector $\boldsymbol{\sigma}$ taken to belong to $\mathbb{R}^d$ and the solution u to $\mathbb{R}$. We consider the DG form of the mixed system (2.2.2):

$$\begin{aligned} \sum_{e\in\mathcal{T}_h}\int_{\Omega_e} \boldsymbol{\sigma}_h\cdot\boldsymbol{\tau}_h \,\mathrm{d}\mathbf{x} &= -\sum_{e\in\mathcal{T}_h}\int_{\Omega_e} u_h \boldsymbol{\nabla}\cdot\boldsymbol{\tau}_h \,\mathrm{d}\mathbf{x} + \sum_{e\in\mathcal{T}_h}\int_{\partial\Omega_e} \widehat{u}_h\boldsymbol{\tau}_h\cdot\boldsymbol{n}\,\mathrm{d}\sigma \\ -\sum_{e\in\mathcal{T}_h}\int_{\Omega_e} \boldsymbol{\nabla} v_h\cdot\boldsymbol{\sigma}_h \,\mathrm{d}\mathbf{x} + \sum_{e\in\mathcal{T}_h}\int_{\partial\Omega_e} v_h\widehat{\boldsymbol{\sigma}}_h\cdot\boldsymbol{n}\,\mathrm{d}\sigma &+ \alpha\sum_{e\in\mathcal{T}_h}\int_{\Omega_e} v_h u_h \,\mathrm{d}\mathbf{x} = s, \end{aligned} \tag{2.2.3}$$

for arbitrary test functions $\boldsymbol{\tau}\in\boldsymbol{G}_h$ and $v_h\in Q_h$,

$$\begin{aligned} \mathbf{G}_h &= \left\{\boldsymbol{\tau}_h \in \left[L^2(\Omega)\right]^N \,:\, \boldsymbol{\tau}_h\,|_e \in [\mathbb{P}_k(e)]^N \,,\ \forall e\in\mathcal{T}_h\right\}, \\ Q_h &= \{v_h\in L^2(\Omega) \,:\, v_h\,|_e\in\mathbb{P}_k(e) \,:\, \forall e\in\mathcal{T}_h\}, \end{aligned} \tag{2.2.4}$$

where $s = \sum_{e\in\mathcal{T}_h}\int_{\Omega_e} v_h f \,\mathrm{d}\mathbf{x}$ stands for the forcing contribution. As we have already mentioned the numerical flux functions $\widehat{u}_h$ and $\widehat{\boldsymbol{\sigma}}_h$ have the role to

ensure the coupling between adjacent elements and to weakly prescribed the boundary conditions. Another important aspect related to the choice of this kind of functions is that they strongly affect the stability and accuracy properties of the method as well as the computational efficiency. For semplicity of notation the summations over the different elements in equations (2.2.3) will be written as the integrals over the whole computational domain. To easily handle at least formally the interface discontinuity we introduce some trace operators accounting for some relevant quantities such as the *jump* and the *average* of the variables of interest. In detail for a vector quantity $\mathbf{v}$ and a scalar q we have:

$$[\![\mathbf{v}]\!] = \mathbf{v}^+ \otimes \mathbf{n}^+ + \mathbf{v}^- \otimes \mathbf{n}^-, \qquad [\![q]\!] = q^+\mathbf{n}^+ + q^-\mathbf{n}^-, \tag{2.2.5}$$

$$\{\mathbf{v}\} = \frac{1}{2}(\mathbf{v}^+ + \mathbf{v}^-), \qquad \{q\} = \frac{1}{2}(q^+ + q^-), \tag{2.2.6}$$

notice that the jump of a vector is a scalar while the jump of a scalar gives a vector, meantime for boundary faces the operators read

$$[\![q]\!] = qn, \quad \{\mathbf{v}\} = \mathbf{v}. \tag{2.2.7}$$

The surface integral of the equations (2.2.3) can be modified using the following identity that exploits the definitions we have just introduced,

$$\int_{\partial\Omega_e} \widehat{u}_h \boldsymbol{\tau}_h \cdot \boldsymbol{n} \, \mathrm{d}\sigma = \int_{\Gamma} \widehat{u}_h [\![\boldsymbol{\tau}_h]\!] \, \mathrm{d}\sigma + \int_{\Gamma^b} \widehat{u}_h \boldsymbol{\tau}_h \cdot \boldsymbol{n} \, \mathrm{d}\sigma \tag{2.2.8}$$

as the integral summations of the equations (2.2.3) can now be rewritten

$$\int_{\Omega_h} \boldsymbol{\sigma}_h \cdot \boldsymbol{\tau}_h \, \mathrm{d}\mathbf{x} = -\int_{\Omega_h} u_h \boldsymbol{\nabla} \cdot \boldsymbol{\tau}_h \, \mathrm{d}\mathbf{x} + \int_{\Sigma_h} \widehat{u}_h [\![\boldsymbol{\tau}_h]\!] \, \mathrm{d}\sigma + \int_{\Gamma_h^0} u_b \boldsymbol{\tau}_h \cdot \boldsymbol{n} \, \mathrm{d}\sigma \tag{2.2.9}$$

$$-\int_{\Omega_h} \boldsymbol{\nabla} v_h \cdot \boldsymbol{\sigma}_h \, \mathrm{d}\mathbf{x} + \int_{\Sigma_h} \widehat{\boldsymbol{\sigma}}_h [\![v_h]\!] \, \mathrm{d}\sigma + \int_{\Gamma_h^0} \boldsymbol{\sigma} \cdot \boldsymbol{n} v_h \, \mathrm{d}\sigma - \alpha \int_{\Omega_h} v_h u_h \, \mathrm{d}\mathbf{x} = \int_{\Omega_h} v_h f \, \mathrm{d}\mathbf{x} \tag{2.2.10}$$

where the boundary Γ_h has been assumed to be only of Dirichlet kind Γ_h^0. The numerical flux $\widehat{u}_h$ is chosen to correspond to the simple centered numerical flux in accordance with the elliptic nature of the problem, *i.e.* $\widehat{u}_h = \{u_h\}$. Hence if we exploit the divergence theorem along with the next identity

$$\begin{aligned} \int_{\Omega_h} \left(v_h \boldsymbol{\nabla} \cdot \boldsymbol{\tau}_h + \boldsymbol{\tau}_h \cdot \boldsymbol{\nabla} v_h \right) \mathrm{d}\mathbf{x} = \int_{\Sigma_h} \left(\{v_h\} [\![\boldsymbol{\tau}_h]\!] + \{\boldsymbol{\tau}_h\} [\![v_h]\!] \right) \mathrm{d}\sigma \\ + \int_{\Gamma_h} v_h \boldsymbol{\tau}_h \cdot \boldsymbol{n} \, \mathrm{d}\sigma, \end{aligned} \tag{2.2.11}$$

we can replace the equation (2.2.9) with

$$\int_{\Omega_h} \boldsymbol{\sigma}_h \cdot \boldsymbol{\tau}_h \, \mathrm{d}\mathbf{x} - \int_{\Omega_h} \boldsymbol{\tau}_h \cdot \boldsymbol{\nabla} u_h \, \mathrm{d}\mathbf{x} + \int_{\Sigma_h^0} \{\boldsymbol{\tau}_h\} \cdot [\![u_h]\!] \, \mathrm{d}\sigma = 0 \qquad (2.2.12)$$

being $\Sigma_h^0 = \Sigma_h \cup \Gamma_h^0$.
The numerical flux $\widehat{\boldsymbol{\sigma}}_h$ of the second equation (2.2.10) of the mixed form of the Helmoltz equation is simply chosen as the average too, *i.e.* $\widehat{\boldsymbol{\sigma}}_h = \{\boldsymbol{\sigma}_h\}$, this makes the second equation of the mixed system reads

$$-\int_{\Omega_h} \boldsymbol{\nabla} v_h \cdot \boldsymbol{\sigma}_h \, \mathrm{d}\mathbf{x} + \int_{\Sigma_h^0} \{\boldsymbol{\sigma}_h\} \cdot [\![v_h]\!] \, \mathrm{d}\sigma - \alpha \int_{\Omega_h} v_h u_h \, \mathrm{d}\mathbf{x} = \int_{\Omega_h} v_h f \, \mathrm{d}\mathbf{x}. \quad (2.2.13)$$

The resolution scheme given by the equations (2.2.12) and (2.2.13) has been named the first Bassi and Rebay method BR1 in the well-known paper by Brezzi *et al.* [1], which provides a complete survey on DG methods for the solution of elliptic problems. In particular the BR1 has been proven to be only weakly stable although consistent; it is moreover claimed of an enlarged computational molecula responsible for the higher computational cost. Both these problems have been solved and the new scheme named BR2 is now being outlined, at this aim we first introduce the *lifting-operator*, a useful mean for the discontinuity handling. Observing the role of the auxiliary variable $\boldsymbol{\sigma}_h$ in the equation (2.2.12) it is evident that it corresponds to the internal gradient plus an additional contribution which accounts for the jumps of u_h at the interfaces,

$$\int_{\Omega_h} \boldsymbol{\tau}_h \cdot \underbrace{(\boldsymbol{\sigma}_h - \boldsymbol{\nabla} u_h)}_{\boldsymbol{\mathcal{R}}_h([\![u_h]\!])} \, \mathrm{d}\mathbf{x} = -\int_{\Sigma_h^0} \{\boldsymbol{\tau}_h\} \cdot [\![u_h]\!] \, \mathrm{d}\sigma. \qquad (2.2.14)$$

The approximated gradient, defined by the operator $\boldsymbol{\mathcal{R}}_h$, is therefore computed by means of these contributions, the latter of which transfering the effect of a discontinuity into the domain. The auxiliary variable and the related numerical vector can now be written as

$$\boldsymbol{\sigma}_h = \boldsymbol{\mathcal{R}}_h[\![u_h]\!] + \boldsymbol{\nabla} u_h \Rightarrow \widehat{\boldsymbol{\sigma}}_h = \{\boldsymbol{\mathcal{R}}_h[\![u_h]\!]\} + \{\boldsymbol{\nabla} u_h\}. \qquad (2.2.15)$$

This expression shows the dependence of the numerical flux $\widehat{\boldsymbol{\sigma}}_h$ on the jumps related to all edges belonging to the two elements which share the generic edge, hence *e.g.* for a triangular grids the support for each edge contains

twelve elements, the cited enlarged molecula. The problem has been fixed by introducing a *local lifting operator* $\boldsymbol{r}_h^e$ for each edge e, both of interface or boundary kind, which is non-zero only for the two elements, or just the only element, containing the edge itself,

$$\int_{\Omega_h^e} \boldsymbol{\tau}_h \cdot \boldsymbol{r}_h^e([\![u_h]\!])\ \mathrm{d}\mathbf{x} = -\int_e \{\boldsymbol{\tau}_h\} \cdot [\![u_h]\!]\ \mathrm{d}\sigma, \qquad \forall e \in \Sigma_h^0 \tag{2.2.16}$$

where Ω_h^e is the support of the edge e. The link between the global and local approach is directly provided by the lifting operator definitions (2.2.14) and (2.2.16),

$$\boldsymbol{\mathcal{R}}_h([\![u_h]\!]) = \sum_{e \in \Sigma_h^0} \boldsymbol{r}_h^e([\![u_h]\!]). \tag{2.2.17}$$

The numerical flux associated to the auxiliar variable $\boldsymbol{\sigma}$ is now defined as $\widehat{\boldsymbol{\sigma}}_h\ |_e = \{\boldsymbol{r}_h^e([\![u_h]\!])\} + \{\boldsymbol{\nabla} u_h\}_e$, meantime the scheme given by eqs. (2.2.12) and (2.2.13) becomes

$$\begin{aligned} \int_{\Omega_h} \boldsymbol{\sigma}_h \cdot \boldsymbol{\mathcal{R}}_h([\![u_h]\!])\ \mathrm{d}\mathbf{x} &= \int_{\Sigma_h^0} \{\boldsymbol{\sigma}_h\} \cdot [\![u_h]\!]\ \mathrm{d}\sigma \\ &= \sum_{e \in \Sigma_h^0} \int_{\Omega_h^e} \boldsymbol{\sigma}_h \cdot \boldsymbol{r}_h^e([\![u_h]\!])\ \mathrm{d}\mathbf{x} \end{aligned} \tag{2.2.18}$$

$$\begin{aligned} -\int_{\Omega_h} \boldsymbol{\nabla} v_h \cdot \Big(\boldsymbol{\nabla} u_h + \boldsymbol{\mathcal{R}}_h([\![u_h]\!])\Big)\ \mathrm{d}\mathbf{x} + \int_{\Sigma_h^0} \{\boldsymbol{\nabla} u_h\} \cdot [\![v_h]\!]\ \mathrm{d}\mathbf{x} + \\ + \sum_{e \in \Sigma_h^0} \int_e \{\boldsymbol{r}_h^e([\![u_h]\!])\} \cdot [\![v_h]\!]\ \mathrm{d}\sigma - \alpha \int_{\Omega_h} v_h u_h\ \mathrm{d}\mathbf{x} = \int_{\Omega_h} f v_h\ \mathrm{d}\mathbf{x}. \end{aligned} \tag{2.2.19}$$

2.3 DG for the INS

The incompressible Navier-Stokes equations discretized by a DG approach are presented for the sake of completness. The equations written in conservative form read as follows

$$\frac{\partial \mathbf{u}}{\partial t} + \nabla \cdot \mathbf{F}(\mathbf{u}, p) = \nabla \cdot \nu \nabla \mathbf{u} \tag{2.3.1}$$

where the inviscid flux $\mathbf{F}$ is given by

$$\mathbf{F}(\mathbf{u}, p) = \mathbf{u} \otimes \mathbf{u} + p\mathbf{I} := u_i u_j + p\delta_{ij}.$$

The domain Ω is approximated by Ω_h and this one is partitioned in order to get a triangulation $\mathcal{T}_h = \{K\}$, where K is a set of non-overlapping elements. The discrete solution $(\mathbf{u}_h, p_h)$ is assumed to belong to the space $\mathbb{P}^k$ of piecewise polynomial functions up to degree k on each element K, not necessarily continuous on element interfaces,

$$\begin{aligned} \mathbf{u}_h \in \mathbf{V}_h &= \left\{ \mathbf{v}_h \in \left[L^2(\Omega) \right]^d \, : \, \mathbf{v}_h \mid_K \in [\mathbb{P}_k(K)]^d \, , \, K \in \mathcal{T}_h \right\}, \\ p_h \in Q_h &= \{ q_h \in L^2(\Omega) \, : \, q_h \mid_K \in \mathcal{T}_h(K) \, : \, K \in \mathcal{T}_h \}, \end{aligned} \tag{2.3.2}$$

being d the number of space dimension. We first rewrite the integral form (2.3.1) in weak form by means of test functions taken in the same functional spaces the solution is assumed to belong to. Then we couple the adjoining elements by means of numerical fluxes which for the advective components still resorts to the solution of a Riemann problem, while for the diffusive term, the BR2 scheme is exploited. This setting leads to the DG Navier-Stokes approximation of the INS equations as follows

$$\begin{aligned} &\int_{\Omega_h} \frac{\partial \mathbf{u}_h}{\partial t} \cdot \mathbf{v}_h \, \mathrm{d}\mathbf{x} + \int_{\Omega_h} \nu \nabla_h \mathbf{u}_h : \nabla_h \mathbf{v}_h \, \mathrm{d}\mathbf{x} \\ &\quad - \int_{\Gamma_h} \left(\nu ([\![\mathbf{u}_h]\!] : \{ \nabla_h \mathbf{v}_h \} + [\![\mathbf{v}_h]\!] : \{ \nabla_h \mathbf{u}_h \}) + \alpha(\mathbf{u}_h, \mathbf{v}_h) \right) \mathrm{d}\sigma \\ &\quad - \int_{\Omega_h} \nabla_h \mathbf{v}_h : \mathbf{F}(\mathbf{u}_h, p_h) \, \mathrm{d}\mathbf{x} \\ &\quad + \int_{\Gamma_h} [\![\mathbf{v}_h]\!] : \widehat{\mathbf{F}}(\mathbf{u}_h^+, p_h^+, \mathbf{u}_h^-, p_h^-) \, \mathrm{d}\sigma = \mathbf{0}, \\ &- \int_{\Omega_h} \nabla_h q_h \cdot \mathbf{u}_h \, \mathrm{d}\mathbf{x} + \int_{\Gamma_h} [\![q_h]\!] \cdot \widehat{\mathbf{u}}(\mathbf{u}_h^+, p_h^+, \mathbf{u}_h^-, p_h^-) \, \mathrm{d}\sigma = 0, \end{aligned} \tag{2.3.3}$$

the jump and average operators are those we refered to previously. The interior penalty term α reads

$$\alpha(\mathbf{u}_h, \mathbf{v}_h) = \sum_{e \in \mathcal{E}_h} \eta_e \int_{\Omega} \nu \mathbf{r}_e([\![\mathbf{u}_h]\!]) : \mathbf{r}_e([\![\mathbf{v}_h]\!]) d\sigma, \tag{2.3.4}$$

where e is the generic face, $\mathcal{E}_h$ the set of boundary and internal element faces, $\mathbf{r}_e : [L^2(e)]^{d^2} \rightarrow \Sigma_h$ is the lift operator defined as the solution of

the (2.2.16). The η_e parameter belonging to $\mathbb{R}^+$ should be chosen owing to stability requirements, the lower bound has been demonstrated to be equal to four for quadrilater elements and three for triangles, although lower values do also work.

Chapter

3 Spectral DG

This chapter is devoted to the definition of an higher order discontinuous Galerkin scheme for the compressible NS equations solution, the key words throughout the whole path are going to be accuracy and efficiency.

Numerical simulations of practical engineering problems are usually satisfied with a relative error of order 10%, sometimes even more, therefore a second-order or at most a third-order accurate scheme is exploited and nothing more. Higher order methods have usually been employed only for direct numerical simulations of turbulent flows, however it has recently recognised that more accurate approaches can provide significant better resolution and results, see *e.g.* [46], [22], [23]. This feature may be particularly relevant when a *long time integration* is required, on this matter the analysis of Kreiss and Oliger reported in [31]. It is shown that the higher the order of approximation the lower the dependency of the computational work on the time of integration even if a stronger operation count is involved. Relations linking the accuracy, the work load and the time of integration, showing such a behaviour, are defined as follows

$$W^{(n)} \propto M^{1/n},$$

with W being the work and M the integration time for an accuracy of order $n+1$. In addition for lower admissible error it is possible to prove that the higher accuracy becomes competitive even for short integration time.

The accuracy feature results to be of main importance for the resolution of turbulent flows, with vortices, eddies rotating flows, structures not well-localized in the domain. Jamenson outlines this scenario, (see [34]), and substantiates the relevance of accurate solutions resorting to the approximation theory. He moved from the fact that any solution may be represented in terms of its Fourier series. The leading error which is assumed to be due merely to the spatial contribution and in particular to the derivatives themselves has been there defined with the form

$$\text{T.E.} = C(\Delta x)^{p-1} k^p,$$

where p is the order of the numerical scheme, Δx the discretization step and k the k-th Fourier mode. It can be observed that for increasing order of approximation the error greatly decreases. The magnitude of the error is strongly linked to the final time of integration, the longer the latter, the higher the first, $\mathrm{E}^k_{\mathrm{leading}} = T_{\mathrm{end}}\mathrm{T.E.}^k$. As we have already anticipated the high accurate solution gives an exponential decay of the error, a more detailed description in the next paragraph.

Spectral convergence

The convergence theory of the h-version of the finite element methods states that the numerical error decays algebraically by refining the mesh, therefore the higher accuracy is achieved in the limit of a 'vanishing' discrete step. The p-type refinement typical of the spectral schemes resorts instead to mantain the discretization parameter fix and meantime to increase the order of the approximating functions. For *smooth* enough solution the p-refinement allows to get the so called spectral convergence which is nothing but another way to state the exponential decay of the error. In figure 3.0.1 the comparison between these two approaches is presented, the red line shows the convergence history, (relatively to the density variable in the L^2 norm), for the ringleb test case, that will be next introduced, for successively finer and finer grids, from 16 to 4096 elements, for a linear approximation. The green line defines the error behaviour for the same case, same variable, for the mesh of 16 elements and an increasing polynomial order, till nine. The errors are plotted on $log-log$ axis as a function of the total number of degrees of freedom N_{dof} for each trial. The figure illustrates that when the polynomial order is kept fix, the error behaves as a linear function of the number of degrees of freedom, while instead for fixed mesh and varying order a nearly exponential trend is got. For the sake of completeness to consider the heavier operation count involved by the higher approximation, we mention that

$$\begin{gathered}\text{Time } \mathbb{P}^1(4096) \approx \text{Time } \mathbb{P}^5(16)\\ o\big(E(\mathbb{P}^1)\big) = 10^{-4}, \quad o\big(E(\mathbb{P}^5)\big) = 10^{-5}.\end{gathered}$$

That is the simulation of order two on the finer mesh requires the same computational time as the necessary one to reach convergence on the coarsest mesh of 16 elements, with the sixth order polynomial, the latter clearly providing an higher accuracy.

Figure 3.0.1: Error on *log-log* axis demonstrating the algebraic convergence of the *h*-type refinement and the exponential convergence of the *p*-type refinement.

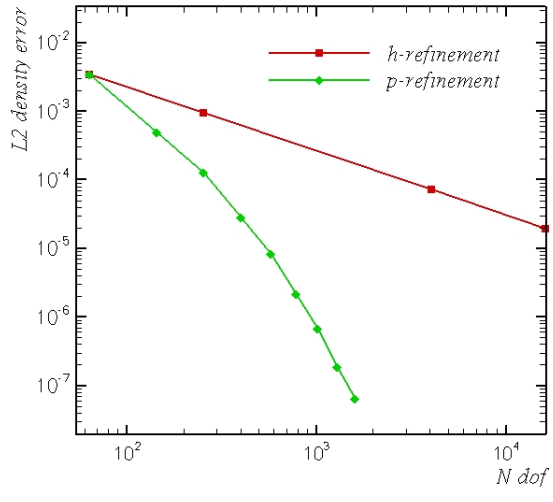

In consideration of the importance of well described flows we focused on the achievement of highly accurate schemes along with an efficient implementation and resolution. The starting point has been our accurate robust DG method which we tried to enhance with the efficiency provided by the spectral collocation approach. The effectiveness has been obtained by an improved assembly procedure of the discrete operators of the NS system, mainly by resorting to the employ of a tensor product strategy. The computational advantage achieved has further been made an important factor by means a *p-multigrid* solver, see [7]. The interpolation theory along with a quite detailed description of the adopted strategies is given in the following before an extensive assessment of the overall algorithm.

3.1 Approximation theory

Let $\mathbb{P}^n$ be the space of all polynomials of degree less or equal to n used to define the approximating function $\mathcal{I}_K(v)$ of v, with $\mathcal{I}_K(v)$ taken as a finite expansion of the form given by Def. 3, in §1.2. The quality of $\mathcal{I}_K(v)$ is of main importance especially for achieving an high-order representation. A favourable criterion for the definition of the basis is the degree of orthogo-

nality, with respect to a suitable inner product $(\cdot,\cdot)$ to be established. The discrete operators involved by this issue are the elemental mass matrix, whose $i-$th $j-$th entry is defined as usual by the inner product (φ_i, φ_j) and the stiffness matrix, namely $\left(\varphi_i^{'}, \varphi_j^{'}\right)$. The aim is to keep the conditioning number of these matrices down for increasing order n, as to avoid an unaccurate or even unstable approximation. Many different basis are available, although all of them may be recast to two main approaches, the *modal* one and the *nodal* one.
The modal space contains polynomials that are characterized by the hierarchical feature, namely for all $n \geq 0$ each component of the basis belongs to $\mathbb{P}^n$ and the higher order components are always got by enriching the lower representation,

$$\{\mathcal{B}\}_n \in \mathbb{P}^n, \qquad \{\mathcal{B}\}_n \subset \{\mathcal{B}\}_{n+1}.$$

The simplest example of such a kind of basis is given by the monomials $\{1, x, .., x^n\}$ which for higher order n provide an unaccurate and unstable behaviour. Better conditioning features can be achieved for example using the Jacobi polynomial family $\mathcal{P}_n^{\alpha,\beta}(x)$, which consists in the polynomial solutions of the singular Sturm-Liouville problem. In one dimension for $-1 \leq x \leq 1$, with parameters $\alpha, \beta > -1$, they are defined for example by

$$\mathcal{P}_n^{\alpha,\beta}(x) = \frac{(-1)^n}{n!} 2^{-\alpha-\beta}(1-x)^{-\alpha}(1+x)^{-\beta}\frac{\mathrm{d}^n}{\mathrm{d}x^n}\Big((1-x)^{\alpha+n}(1+x)^{\beta+n}\Big) \quad (3.1.1)$$

and characterized by the following useful orthogonal relationship,

$$\int_{-1}^{1}(1-x)^{\alpha}(1+x)^{\beta}\mathcal{P}_n^{\alpha,\beta}(x)\,\mathcal{P}_i^{\alpha,\beta}(x)dx = C\delta_{ni}, \quad (3.1.2)$$

where δ_{ni} stands for the usual Kronecker function and the constant C depends on the degree n and on the parameters α and β. Particular choices of these parameters retrieve some well-known Jacobi polynomials as the Legendre ($\alpha = \beta = 0$), or the Chebyshev polynomials ($\alpha = \beta = 1/2$).
A more 'physical' point of view is instead associated to the nodal space, the polynomial interpolant of order n, given a set of $n+1$ points, is computed by imposing the i-th expansion coefficient to be coincident with the value to be interpolated, *i.e.* $\mathcal{I}_n(f(x_i)) = f(x_i)$. Such an approximation makes the *nodal* value be the required solution field, as it can be observed from the lagrangian nodal relation itself defined in the following

$$\mathcal{I}_n\big(f(x)\big) = \sum_{k=1}^{n+1} f_N(x_k)\,\mathscr{L}_k(x) \quad (3.1.3)$$

where $\mathscr{L}_k$ is the $k-$th Lagrange polynomial

$$\mathscr{L}_k = \frac{\pi_{j=1}^{n+1}(x - x_j)}{\pi_{j=1}^{n+1}(x_k - x_j)}, \quad j \neq k, \tag{3.1.4}$$

which results in $\mathscr{L}_k(x_j) = \delta_{kj}$, $1 \leq k, j \leq n+1$, with δ the Kronecker function.
The conditioning number of the mass matrix for the hierarchical monomials is shown to grow as 10^n, being n the order of the polynomial expansion, and the same can be refered for the lagrangian strategy in the case of equispaced interpolation nodes for $n > 5$. The high conditioning number related to these strategies is due to the fact that the basis is becoming numerically linearly dependent for increasingly order of approximation. The Legendre polynomials along with suitably chosen nodes provide instead a stable behaviour.
Once the basis has been chosen the function f can be approximated by a locally continuous expansion of order n on each element $\Omega_e \in \mathcal{T}_h$, often this procedure is first led and related to a reference standard element as

$$\mathcal{I}_n\big(f(\xi)\big) = \sum_{i=1}^{n+1} f_i \mathcal{P}_i\big(\xi(x)\big), \tag{3.1.5}$$

where f_i are still the coefficients and $\mathcal{P}_i$ the basis components. In one dimension the $-1 \leq \xi \leq 1$ is assumed to be the reference interval, the local coordinate as been named ξ. The link between the local and the global space is established by means of a map which transforms the reference element into the actual one.
The extension of these approximations to two or three dimensions domains is straightforward only for cartesian elements, for example we can consider a reference quadrilateral with local coordinates $-1 \leq \xi_1, \xi_2 \leq 1$ and perform a standard tensor product between the selected one-dimensional functions,

$$\varphi_{ij}(\xi_1, \xi_2) = \varphi_i(\xi_1)\varphi_j(\xi_2), \quad 1 \leq i, j \leq n+1, \tag{3.1.6}$$

where φ_{ij} represents the $ij-$th two dimensional shape functions. Simplicial elements $\{x \in \mathbb{R}^d, x_i \geq 0, 1 \leq i \leq d, \sum_{i=1}^d x_i \leq 1\}$ require instead more care. Since a great part of the efficiency comes from the tensor product extension (3.1.6) a frequently used strategy is the transformation of the simplex into a cuboid introducing a *collapsed* coordinate system which makes the simplex

bounds be limited between constant values. Consider the following two-dimensional reference elements

$$T^2 = \{(\xi,\eta)| -1 \leq \xi,\eta;\ \xi+\eta \leq 0\},$$

$$Q^2 = \{(\zeta,\eta)| -1 \leq \zeta,\eta \leq 1\},$$

the node $(1,1) \in Q^2$ can be entailed to collapse on its leftmost upper corner as to get the reference triangle T^2. A suitable transformation of coordinates which maps the elements one another, that in particular makes points with constant ζ become points with constant $(\xi+\eta)$, reads

$$T(Q) : (\zeta,\eta) \rightarrow (\xi,\eta) = \begin{pmatrix} \frac{(1+\zeta)(1-\eta)}{2} - 1 \\ \eta \end{pmatrix}, \tag{3.1.7}$$

as depicted in Fig. 3.1.1. The triangular basis which spans the space T^2 needs

Figure 3.1.1: Triangle-quadrangle mapping

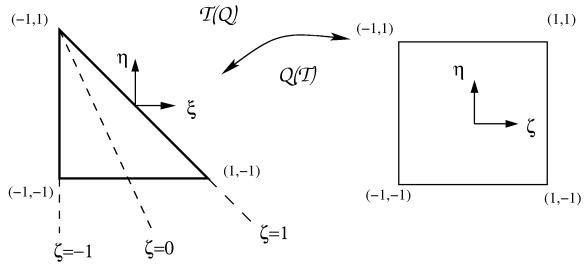

$\frac{(n+1)(n+2)}{2}$ degrees of freedom, the most straightforward choice for the basis is the hierarchical approach given by the monomials $x^i y^j$ with $0 \leq i+j \leq n$ for approximation of order n. Dubiner [18] proposed an orthogonal hierarchical basis resorting to the Jacobi polynomials for the simplex element, which is defined by means of a modified tensor product along the ζ and the η axis, exploiting the collapsed system (3.1.7). In two dimension the i,j-th shape function reads

$$\begin{aligned} \phi_{ij}(\xi,\eta) &= \varphi_i(\zeta)\varphi_{ij}(\eta) \\ &= \mathcal{P}_i^{(0,0)}(\zeta)(1-\eta)^i \mathcal{P}_j^{2i+1,0}(\eta) \end{aligned} \tag{3.1.8}$$

with $0 \leq i+j \leq n$ for an approximation in $\mathbb{P}^n$, the factor $(1-\eta)^i$ acting on $\mathcal{P}_i^{(0,0)}(\zeta)$ keeps the expansion of order i with respect to the cartesian

system. The idea can be extended to tetrahedra by employing the collapsing procedure once more.
Spectral methods usually adopt a nodal strategy for cartesian domains, *i.e.* lagrangian $p-$type elements through the zero of the Gauss-Lobatto polynomials, while for simplicial elements they resort to a modal representation, even because optimal interpolation nodes are not yet available. This kind of transformation has been used by many authors in conjunction with different numerical techniques, both the modal [46] , [33], and the nodal [23], [22] spaces have been considered.

Interpolation Nodes

The location of the nodes is of primary importance for the quality of the approximation. Equispaced nodes lead to the well-known Runge oscillations and consequently to a bad conditioning of the mass-matrix. This phenomenon is associated to the lack of information near boundaries, where this behaviour is observed, therefore the addensation of nodes in these regions allows to almost eliminate or greatly reduce the problem. The quality of the interpolation function is usually measured by means of the maximum norm $\|\cdot\|_\infty$ and the error due to the approximation of f by $p(x)$, $\|f(x) - p_n(x)\|$ is often estimated with respect to the best approximating polynomial $r_n(x)$ achieveable,

$$\|r - f\|_\infty = \min_{p \in \mathbb{P}^n} \|p - f\|_\infty. \tag{3.1.9}$$

The polynomial $p(x)$ can be seen as the projection of the function f into the space $\mathbb{P}^n$ by means of a projection operator P_n, which can be characterized in terms of the spanning basis $\mathcal{L}$,

$$\|P_n\| = \max \sum_{k=0}^{n} |\mathcal{L}_k(x)| = \Lambda_n. \tag{3.1.10}$$

The parameter Λ_n is known as the Lebesgue constant, its minimization ensures stability to the approximating function. For $n-$dimensional cartesian domains the Gauss-Lobatto points have been proven the optimal choice, while for triangular and tetrahedral geometries the optimal set is still not known. Many attempts have been done in order to get a good set of interpolation nodes, among them we recall the work of Taylor, Wingate and Vincent [25]. They presented an algorithm to compute Fekete nodes on triangles: this set is obtained by maximixing the determinant of the generalized Vandermonde

matrix associated to the selected basis $\mathcal{B}$, on the boundary the Lobatto points have been straightforwardly mantained. Another approach has been introduced by Hesthaven see [30], by means of the electrostatic interpretation of the Jacobi polynomials. He solved a minimization problem in which the positions of the nodes inside the reference triangle have been assumed as to be the natural configuration required by the electrostatic equilibrium.
Next we consider some basic concepts taken from the classical interpolation theory at the aim to guess the error associated to the discretization process itself.

3.1.1 Interpolation on affine meshes

The error involved by the approximating process $u_h \to u$ with $V_h \to V$ for conforming elements $V_h \in V$ is now being considered. The field u_h is mainly taken to be of polynomial *interpolant* kind $\Pi_h u$, the presentation is led in accordance with [12].

Theorem 1 *Let there be given a regular affine family of finite elements K, P_K, Σ_K whose reference finite element $\hat{K}, \hat{P}, \hat{\Sigma}$ undergoes to suitable assumptions on the space it belongs to. Then there exists a constant $C = C(\hat{K}, \hat{P}, \hat{\Sigma})$ indipendent of K such that*

$$\forall v \in \mathbf{H}^{k+1}(K), \quad \|v - \Pi_K v\|_{m,K} \leq C \frac{h_K^{k+1}}{\rho_K^m} |v|_{k+1,K}, \, 0 \leq m \leq k+1, \tag{3.1.11}$$

where Π_K defines the $\mathbb{P}^k$-interpolation operator.

Consider a family of regular finite elements for which the following properties holds:

$$\exists \, \sigma \text{ s.t} \quad \forall K \quad \frac{h_K}{\rho_K} \leq \sigma \quad \text{and} \quad h_k \to 0, \tag{3.1.12}$$

where h_K defines the diameter of the element K, ρ_K the diameter of the smallest ball inscribed in K. The error estimate (3.1.11) in view of the assumption (3.1.12) simplifies to

$$\|v - \Pi_K v\|_{m,K} \sim o(h_K^{k+1-m}). \tag{3.1.13}$$

Theorem 2 *In addition to the previous regularity requirements we assume that there exists an integer $k \geq 1$ such that*

$$P_k(\hat{K}) \subset \hat{P} \subset \mathbf{H}^1\left(\hat{K}\right)$$

and

$$\mathbf{H}^{k+1}\left(\hat{K}\right) \subset \mathcal{C}^s\left(\hat{K}\right)$$

where s is the maximal order of the partial derivatives involved by the reference element. If the solution of the variational problem u belongs to $\mathbf{H}^{k+1}((\Omega))$, there exists a constant C indipendent of h such that

$$\|u - u_h\|_{1,\Omega} \leq Ch^k |u|_{k+1,\Omega}, \tag{3.1.14}$$

where $u_h \in V_h$ is the numerical solution, $h = \max h_K$, $K \in \mathcal{T}_h$.

Theorem 3 *If the assumption of* Theorem 2 *holds and moreover we consider $s = 0$ along with regularity requirements on the adjoint problem, then there exists a constant C indipendent of h such that*

$$|u - u_h|_{0,\Omega} \leq Ch^{k+1} |u|_{k+1,\Omega}, \tag{3.1.15}$$

with the solution u which has still to be assumed to belong to $\mathbf{H}^{k+1}(\Omega)$.

The error upper bounds given by inequalities (3.1.14) and (3.1.15) define the best results achievable for a sufficiently smooth solution. As remarked by the hyphotesis entailed by these theorems it stems out that the higher the order of convergence, the higher the assumed regularity of the solution.

3.1.2 Interpolation on non-affine meshes

Consider the interpolation on a family of quadrangular grids, the following results hold, see [12], [19].

Lemma 1 *Let K be a non-degenerate convex quadrangle in $\mathbb{R}^2$, and $F_K \in [\mathbb{Q}^1]^2$ a unique bijective transformation such that $F_K(\hat{K}) = K$, the map is not affine. The jacobian matrix J_K of F_K and its determinant are bounded by geometrical constant,*

$$\begin{aligned} \|\det(J_K)\|_{L^\infty\left(\hat{K}\right)} &\leq ch_K^2, \\ \|J_K\|_{[L^\infty\left(\hat{K}\right)]^{(2,2)}} &\leq ch_K. \end{aligned} \tag{3.1.16}$$

Theorem 4 *Let $\{\hat{K}, \hat{P}, \hat{\Sigma}\}$ be the reference finite element with $\hat{K} = [0,1]^2$ and associated normed vector space $V(\hat{K})$. Assume that there exists an integer k such that $\mathbb{Q}^k \subset \hat{P}$ and $H^{k+1}\left(\hat{K}\right) \subset V(\hat{K})$. Let K be a qudrangle*

in $\mathbb{R}^2$ *and let* Π_K^k *be the local interpolation operator in* K*. Let the family* $\mathcal{T}_h$ *be shape regular, namely the equation* (3.1.12) *holds. Then there exists a constant* c *such that for all* h *and* $v \in H^{k+1}(\Omega)$*,*

$$\|v - \Pi_K v\|_{0,\Omega} + \sum_{m=1}^{k+1} h^m \Big(\|v - \Pi_K v\|_{m,K} \Big)^{\frac{1}{2}} \leq c h^{k+1} |v|_{k+1,\Omega}. \tag{3.1.17}$$

If V_h^k *is* H^1*-conformal,*

$$\forall h,\ \forall v \in H^{k+1}(\Omega), \quad \|v - \Pi_K v\|_{k+1,\Omega} \leq c h^k |v|_{k+1,\Omega}. \tag{3.1.18}$$

3.1.3 Elemental approximation

The procedure necessary for the achievement of the numerical solution, such as the interpolation, the quadrature and the error estimates may be easier performed using a reference space, which is then mapped into the real element. Let ξ be the local reference coordinates while $\mathbf{x}$ the global coordinates related to the domain Ω and let $F : \xi \in \widehat{K} \rightarrow \left(F_j(\xi)\right)_{j=1}^n \in \mathbb{R}^n$ be the one-to-one mapping which performs the transformation.

Definition 4 (Isoparametric families of finite element) *The family of finite elements* (K, P_K, Σ_K) *is an isoparametric family if all its elements are isoparametrically equivalent to a single reference finite element* $(\widehat{K}, \widehat{P}, \widehat{\Sigma})$*, namely a one-to-one mapping* $F_K : \widehat{K} \rightarrow \mathbb{R}^n$*,* $F_K \in (\widehat{P})^n$ *exists such that*

$$\begin{aligned} K &= F_K(\widehat{K}) \\ P_K &= \{p : K \rightarrow \mathbb{R}; \quad p = \widehat{p} \cdot F_K^{-1};\ \widehat{p} \in \widehat{P}\} \\ \Sigma_K &= \{p(F_K(\widehat{a}_i); \quad 1 \leq i \leq N\}. \end{aligned} \tag{3.1.19}$$

In the affine case the Jacobian of the mapping is constant, therefore the transforming map (3.1.19) does not alter the nature of the polynomial defined in $\widehat{P}$, while for the higher order approximation the reference polynomials are mapped into functions which are in general no more belonging to $\mathbb{P}^n$. This problem can be ignored as soon as you are working with the reference element although the same happens for the real geometry. We just remark that the invertibility of the mapping is ensured if we have a regular isoparametric family, namely eq. (3.1.12) holds.

An element is said to be *sub-parametric* when the order of the geometrical polynomials is lower than that associated to the interpolation procedure, while it is *super-parametric* in the opposite situation. In this last case the convergence may be not achieved as the discretization parameter h approaches zero. The error bounds presented in §3.1.1 are still valid for the higher order *iso-parametric* elements provided the mapping of such a kind of family is not too far from the affine one and is sufficiently regular. The discrepancy between them must be such as to yield the same interpolation error as in the affine case. The proof of the above statement can be find in Ciarlet [12].

Numerical integration

Volume and surface integrals are usually approximated by numerical integration *i.e.* quadrature formulae which compute the integral by a finite summation of the integrand functions suitably weighted. For the reference element we therefore have

$$\int_{\Omega_e} f(\mathbf{x}) d\mathbf{x} = \int_{\Omega_{ref}} f(\boldsymbol{\xi}) \frac{\partial \mathbf{x}}{\partial \boldsymbol{\xi}} d\boldsymbol{\xi}, \tag{3.1.20}$$

where $\frac{\partial \mathbf{x}}{\partial \boldsymbol{\xi}}$ defines the Jacobian of the mapping. The integrand is conveniently replaced by a lagrangian interpolant of degree $Q-1$,

$$\int_{\Omega_{ref}} f(\boldsymbol{\xi}) d\boldsymbol{\xi} = \sum_{i=1}^{Q} \omega_i f(\boldsymbol{\xi}_i) + R(f), \tag{3.1.21}$$

being ω_i the quadrature weights, ξ_i the evaluation nodes and $R(f)$ the integration error. The summation results to be exact for polynomial of order $Q-1$ for the equispaced nodes choice, although for better placements it is possible to exactly integrate higher order polynomials, it is the case of the Gaussian nodes. There are three types of Gaussian integration rules, the Gauss, the Gauss-Radau and the Gauss-Lobatto. The first uses quadrature nodes computed as zeros of a polynomial which are located only inside the reference domain, *i.e.* in one dimension $[-1,1]$, the second assumes one zero to be coincident with one of the end points, usually with the $\xi = -1$ point, while the latter exploits both the boundaries.

Gauss Lobatto quadrature

This quadrature rule evaluates the functions f of the summation (3.1.21) on non equispaced points ξ_i containing the end-points of the domain itself,

$-1 < \xi < 1$. The internal nodes are obtained as the roots of the first derivatives of Legendre polynomials of degree $n-1$, $\mathcal{L}'_{n-1}$, when we are looking for the $n-$points rule. The weights ω_i are computed by

$$\omega_{n,k} = \frac{2}{n(n-1)\mathcal{L}^2_{n-1}}(\xi_i), \quad k = 2, .., n-1, \tag{3.1.22}$$

while for $\xi = \pm 1$ we have

$$\omega_{n,1} = \omega_{n,n} = \frac{2}{n(n-1)}. \tag{3.1.23}$$

The order of accuracy provided by the Lobatto quadrature formulae is $2n-3$ when using n nodes. The extension to cartesian multidimensional domain makes use of the product of the one-dimensional rule along each direction of the domain, *e.g.* in two-dimension we get

$$\int\int_{\text{refQ}} g(\xi_1, \xi_2)\mathrm{d}\xi_1\mathrm{d}\xi_2 \sim \sum_{i=1}^{n}\sum_{j=1}^{m} \omega_i\omega_j g(\xi_i, \xi_j). \tag{3.1.24}$$

Gauss quadrature

The Gauss quadrature rule still consists of the weighted evaluation of the integrand function in well-chosen non equidistributed nodes. In this case the quadrature nodes do not have to fulfill any constrained position, this stems in an increase of the accuracy order, as a matter of fact a n-integration nodes rule guarantees to exactly integrate polynomials of degree up to $2n-1$. The integration points are the roots of the Legendre polynomials $\mathcal{L}_n(\xi)$, while the weights are given by

$$\omega_{n,i} = \frac{2}{(1-\xi^2_{n,1})\mathcal{L}'_n(\xi)^2} \quad i = 1, .., n. \tag{3.1.25}$$

The extension to multi-dimensional structured domains follows the tensorial approach presented in equation (3.1.24). For triangular element it is even possible to recast the integrand function to the reference quadrilateral (3.1.7). The Jacobian involved by this coordinate transformation introduces a linear contribution which raises the order of the function to be integrated, this would require to increase the order of the quadrature formula in the ξ_2 direction. Such a process is claimed to generate an unuseless addensation of points near the collapsed vertex. It is otherwise possible to employ accurate cubature rule whose nodes are better distributed inside the element providing an accuracy of order $2n$.

Convergence rate - Quadrature order

The approximation of the variational form on the reference element requires to consider the effect of the integration of products, of derivatives and moreover the possible presence of non-linearities due to the mapping procedure. These operations may produce a function which does belong no more to the space of polynomials $\mathbb{P}^n$. Therefore the order of accuracy of the quadrature rule should such that to correctly evaluate the highest order functions, however the involved non-linearities often make the integrand quantity somewhat unknown. Therefore an exact computation would require a scheme for rational function which is not available. The following theorem has the purpose to briefly assess the accuracy of the quadrature rule, (see paragraph 4.1, [12]). Assume we are solving a second-order elliptic boundary value problem, $\Delta u = f$, whose variational form is provided by the following bilinear forms

$$a(u,v) = \int_\Omega \sum_{i.j=1}^{n} a_{ij}\partial_i u \partial_j v \ \mathrm{d}\mathbf{x}, \quad f(v) = \int_\Omega fv \ \mathrm{d}\mathbf{x}, \quad V = H_0^1(\Omega), \quad (3.1.26)$$

with $a_{ij} \in W^{k,\infty}(\Omega)$ and $f \in W^{k,q}(\Omega)$, $q \geq 2$. The effect of the numerical integration on the rate of convergence of conforming methods does not determine an alteration of the estimates given by *Theorem 2* as stated by the following theorem.

Theorem 5 *Consider a regular triangulation of the domain Ω as done in* Theorem 1, *assume that there exists an integer $k \geq 1$ such that*

$$\widehat{P} = P_k(\widehat{K}), \quad \mathbf{H}^{k+1}\left(\widehat{K}\right) \subset \mathcal{C}^s(\widehat{K}), \quad (3.1.27)$$

where s is the maximal order of partial derivatives occuring in the definition of the set $\widehat{\Sigma}$. Provided the reference quadrature formulae are taken to exactly integrate functions in space $\mathbb{P}^{2k-2}(\widehat{K})$, then if the solution of the variational problem $u \in H_0^1(\Omega)$, there exists a constant C indipendent of h such that

$$\|u - u_h\|_{1,\Omega} \leq Ch^k\Big(|u|_{k+1,\Omega} + \sum_{i.j=1}^{n} \|a_{ij}\|_{k,\infty,\Omega}\|u\|_{k+1,\Omega} + \|f\|_{k,q,\Omega}\Big), \quad (3.1.28)$$

where $u_h \in V_h$ is the discrete solution.

The Galerkin methods require to numerically compute inner products of the form $(\cdot,\cdot)$, in particular for linear problems the minimum number of quadrature points necessary for the exact evaluation of such a product are $n+1$, while for quadratic non-linearities $3n/2+2$ points are needed. In the case of cubic non-linearities the minimum number is $2n+2$. Mainly the linear contribution is only exactly considered, therefore the associated scheme suffers of an aliasing phenomenon of the highest modes clearly due to the under-integration which may be treated by a filtering approach. Such a process is here just mentioned. Consider the following inner product

$$(\varphi,\psi)_Q = \sum_{q=1}^{Q} \omega_i \varphi_q(\xi_i)\psi(\xi_i), \tag{3.1.29}$$

with $\varphi \in \mathbb{P}^n$ and $\psi \in \mathbb{P}^{2n}$ expanded in term of Legendre polynomials and decomposed as follows

$$(\varphi_q,\psi)_Q = \Big(\varphi_q, \sum_{p=1}^{n+1} \widehat{N}_p L_p\Big)_Q + \Big(\varphi_q, \sum_{p=n+2}^{2n+1} \widehat{N}_p L_p\Big), \tag{3.1.30}$$

the exact integration of the above product is achieved by neglecting the last contribution which by definition corresponds to a null error R in (3.1.21), a cut of the selected frequencies.

Differentiation

Derivatives computation can be performed either in the physical space or in the transformed space, it however clearly requires useful effective formulae. Being $\mathcal{F}(\xi)$ the mapping from the standard region to the real one, the differentiation of $u_h(x)$ with respect to x is obtained as

$$\frac{\mathrm{d}u_h(\xi)}{\mathrm{d}x} = \frac{\mathrm{d}u_h(\xi)}{\mathrm{d}\xi}\frac{\mathrm{d}\xi}{\mathrm{d}x} = \sum_{p=1}^{n+1} \widehat{u}_p \frac{\mathrm{d}\varphi_p(\xi)}{\mathrm{d}\xi}\frac{\mathrm{d}\xi}{\mathrm{d}x}, \tag{3.1.31}$$

where φ_p is the p-th component of the expansion basis. The derivative $\frac{\mathrm{d}\varphi_p(\xi)}{\mathrm{d}\xi}$ can be computed by means of a quite directly manner for the modal Jacobi family since many analytic expressions do exist. Even the lagrangian nodal approach is endowed of general relations for the derivatives calculation, we

mention the evaluation based on the Lagrange representation provided by Funaro,

$$\mathscr{L}_i(\xi) = \frac{g_Q(\xi)}{g_Q^{'}(\xi_i)(\xi - \xi_i)}, \quad g_Q(\xi) = \prod_{j=1}^{Q}(\xi - \xi_j), \tag{3.1.32}$$

whose derivatives are given by

$$\frac{\mathrm{d}\mathscr{L}_i(\xi)}{\mathrm{d}\xi} = \frac{g_Q^{'}(\xi)(\xi - \xi_i) - q_Q(\xi)}{g_Q^{'}(\xi_i)(\xi - \xi_i^2)}. \tag{3.1.33}$$

3.2 Spectral DG method

The interest towards high-order accurate solutions of the Navier Stokes equations in aerodynamics and in many other application fields requires to focus mainly on the efficiency matters. Therefore the numerical discretization must resort to procedures that keep the operation count value down, such an aim involves the construction and the evaluation phase of the discrete operators associated to the Galerkin formulation of the system to be solved. Once the final algebraic system has been obtained effective resolution strategies are needed to rapidly approach the unknown fields. In accordance with the interpolation theory the optimal convergence can be achieved if the problem is endowed of the sufficient regularity, this aspect clearly has a central role for high accuracy levels.

After the presentation of the main issues related to the interpolation theory and to the construction of the discrete operators, such as the discrete laplacian or the discrete advection for the NS problem, we are going to present our works for the purpose outlined in the beginning of this paragraph. We have devised a spectral DG scheme for the Navier-Stokes equations solution joining the robustness and flexibility of the latter, and nonetheless the inherent accuracy already characterizing it, with the exponential behaviour provided by the spectral approaches. The overall scheme should be such that to match the higher order representation with an assembly phase and with a solution methodology as effective as possible in order to reduce the strong dependence of the computational cost on the level of approximation. In consideration of this we have built the discrete operators resorting to the use of the nodal co-location strategy typical of spectral methods, along with a tensorial computation of the approximating functions. The discrete problem

has been solved by means both of a linearized implicit method and of the new p-multigrid scheme presented in [7], that fully exploits the advantages of the reduction cost that the fair operator construction has achieved.
The numerical scheme adopted is of discontinuous Galerkin kind as introduced in the second chapter, the advective numerical flux has been obtained by the resolution of the Riemann problem through the Godunov approach, while the numerical diffusive flux has been computed through the BR2 method. The approximated solution field u_h has been represented in the nodal space, the related interpolation nodes choice is detailed in the following.
The strategy we are going to present is only concerned with structured possibly non-conforming domains, on this issue we make some discussion in order to outline the conditions in which this approach may be useful. In fact localized fluid flow features can be well resolved by means of either a selective local refinement process or of an efficient higher-order discretization. The former strategy known as adaptive mesh refinement (AMR) offers an accurate and efficient resolution in the case of structures that are limited to a part of the domain and not 'widely diffused' through all it. The inherent flexibility provided by a discretization through triangles and tetrahedra may work as well as the AMR if the field is approximated in a sufficiently accurate way. Moreover the higher schemes are shown to be competetive, if not superior, with respect to the adaptive strategies in the case of complicated structures to be defined unless higher order functions are used in the AMR techniques themselves, see [34]. Hence we focused on highly accurate results through the use of unstructured domains or non-conforming cartesian elements. We have worked on the definition of a strategy that well resolves the flow structures by an higher-order computational competitive strategy: flexible and accurate DG plus efficient tensorial co-location on cartesian domains plus effective p-multigrid resolution.

3.2.1 Co-location strategy

The efficiency we have talked about for so long finds its explication in the easiest assembly of the discrete operators permitted by the co-location of the interpolation points at the same position of the evaluation nodes. The tensor product strategy for the construction of the function results to be the mean to accomplish such an aim, the positive effect is particuraly relevant for the derivatives computation. The classical spectral methods assume the

solution to be approximated and computed in the Gauss-Lobatto nodes. For the former aspect the choice has already refered as the optimal one while for the latter it results to be responsible of under-integration. However this fact has been claimed to be negligible because the integration error has been proven to be consistent with that introduced by the approximation process itself and therefore the overall scheme should work in coherent way, [46]. We now describe the computational advantages which come from the use of the Lobatto nodes as unique set for both interpolation and quadrature.

Diagonal local-mass matrix

Consider a two dimensional cartesian reference domain Ω_{ref} spaned by the shape functions $\phi_{ij} \in \mathbb{P}^n$ computed as the tensor product of the one dimensional lagrangian functions,

$$\phi_{ij}(\boldsymbol{\xi}_k) = \varphi_i(\xi_r)\varphi_j(\eta_s) \tag{3.2.1}$$

where $\boldsymbol{\xi}_k$ is the k-th quadrature node and with $i, j = 1, .., n+1$ the local indices along the ξ and η directions respectively and with r, s the local number of the quadrature points. The link between the $2d$ and the $1d$ numberings is provided by a bijective map $k = f(i, j)$. The delta Kronecker property of the adopted functions makes the mass matrix be diagonal, for the DG this fact represents a limited saving, since the matrix has a local nature. The discrete laplacian matrix do not have a particular structure, it is a full matrix.

Discrete operator assembly

The fair evaluation of the discrete operators constitutes the key point for the efficiency matter, the advective and the diffusive terms gain important advantage from the derivatives computation. In detail if we consider a two dimensional reference element, isotropic for semplicity of notation, spaned by the shape functions $\phi_{ij} \in \mathbb{P}^n$, with $i, j = 1, .., n+1$, we get *e.g.* for the derivatives along the x direction the following semplification

$$\begin{aligned} \frac{\partial \phi_{ij}(\boldsymbol{\xi}_k)}{\partial \xi} &= \varphi_j(\eta_s)\frac{\partial \varphi_i(\xi_r)}{\partial \xi} \\ &\neq 0 \quad \text{for} \quad j = s \ \wedge \ r = 1, .., n+1. \end{aligned} \tag{3.2.2}$$

Therefore, for approximating functions belonging to $\mathbb{P}^n$ on a nd-dimensional domain, the derivatives matrix evaluation requires $nd(n+1)$ operations, for

each quadrature node on each element for each unknown equation. This value replaces the operation count of the standard approach, using two different set of nodes, which amounts to $(n+1)^2$ operations for each quadrature node on each element, for each unknown. The reduced operation count due to the tensorial approach in co-located elements is shown in Fig. 3.2.1 and it is usually named sum factorization transform. The easier jacobian assembling

Figure 3.2.1: Isoparametric mapping of order two. Circled in red the degrees of freedom involved by the node (1,1) for the derivatives calculation in the case of co-located strategy

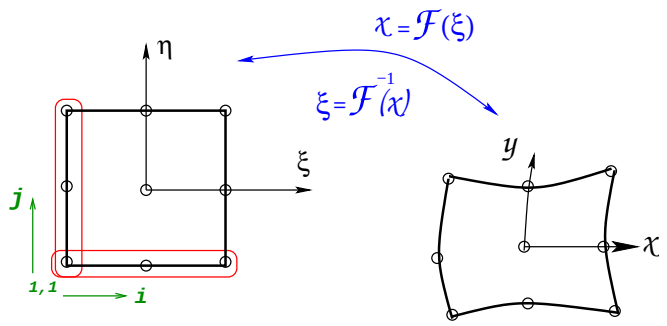

procedure *e.g.* for the advective contribution, $\int_K \mathbf{v}\cdot\boldsymbol{\nabla}\boldsymbol{\mathcal{F}}_c \,\mathrm{d}\mathbf{x}$, requires to execute only $nd^3(n+1)$ operations instead of the standard $nd(n+1)^4$ operations for each node on each element of the computational domain, clearly for each unknown equations. The viscous contribution for each element on each node passes from $(n+1)^4$ operations to $nd^4(n+1)^2$, for each block of the matrix of the sytem.

Surface contribution handling

Another important computational reduction comes from the interface contribution evaluation, which exploits the clear convenience given by the presence of nodes on the edges, (or faces in $3d$) themselves. Therefore the value of a certain field is already available and it does not require to exploit the complete expansion to be recovered. In addition the discrete operator construction mantains the favourable approach above described. Consider for example the assembly of residual and jacobian contribution of the viscous contribution

$$\int_{\Gamma_h} \nu\Big(\llbracket\mathbf{u}_h\rrbracket : \{\nabla_h\mathbf{v}_h\} + \llbracket\mathbf{v}_h\rrbracket : \{\nabla_h\mathbf{u}_h\}\Big)\,\mathrm{d}\sigma, \tag{3.2.3}$$

given by a standard residual assembly procedure it would require $(n+1)^4$ operations for each quadrature node on each face for each equation, while by the reduced process the count dicreases to $(n+1)^2$. For the jacobian contribution the reduction results to be more significant as shown for the volume integral precedengly, since it is applied to each block matrix involved for each node, for each face.
The memory requirement is minimal if derivatives are stored just for the reference element and then computed on the real domain each time they are required.
The above described strategy has been mutuated, as said, from the classical spectral methods with the attempt to enhance the performance of the numerical discretization. The first step we did has been consisted in the realization of such a *spectral* DG code and in its successive validation. The next step has been a trial towards a slightly new technique, which exploits all the discretization ingredients we have presented, but that it resorts to a different set of co-location nodes. This idea is mainly due to some experimental observation we did that will be shown in the sequel and to the associated interest in understanding the balance between accurate representation of the unknown field and its evaluation. Since the Gauss-Lobatto nodes define the optimal choice from an interpolation point of view but they are not enough to exactly integrate the NS discrete inner products, we thought to reverse the approach. We therefore used another gaussian set to provide *right* quadrature admiting this choice being optimal no more for the approximation, *i.e.* the Gauss nodes. The co-location on this set preserves the advantages of the Lobatto set choice except for the fair evaluation of the interface contribution. As a matter of fact, since there are no nodes directly located on the boundaries, internal or external, it is necessary to resort to the complete polynomial expansion based on the internal values in order to get the required field. Further description is given in the following by means of a series of test cases.

3.2.2 Inviscid Test Case

The validation of our spectral DG scheme has been led first by solving the Euler equations for some well-known two dimensional test case, in particular we considered the ringleb channel, the flow past a circle and the gaussian bump. The first problem has been exploited for the definition of the accuracy property and even for the evaluation of the computational improvement that the spectral technique mutuation provided to the algorithm. The other tests

have furtherly assessed the comparison between the two set of co-location nodes adopted and nonetheless they was the way to verify the capacity and the robustness of the code. Different computational triangulations of the domain have been used, those reported in this section are mainly the nearly coarsest possible to best outline the high accuracy relevance. Tests have been done on finer grids too.

Ringleb Test Case on Lobatto Nodes

The ringleb test case provides the analytical solution for an inviscid flow which turns around a symmetric obstacle. The solution is obtained by an hodograph method in implicit form and it reads

$$\begin{aligned} x(q,k) &= \pm\frac{1}{kq\rho}\Big(1-\frac{q^2}{k^2}^{\frac{1}{2}}\Big), \\ y(q,k) &= \frac{1}{2\rho}\Big(\frac{1}{q^2}-\frac{2}{k^2}\Big)+\frac{1}{2}J, \\ J &= \frac{1}{c}+\frac{1}{3c^3}+\frac{1}{5c^5}-\frac{1}{2}\ln\Big(\frac{1+c}{1-c}\Big), \end{aligned} \tag{3.2.4}$$

where k is a *stream-function* that can be expressed as $k=\frac{q}{\sin\theta}$ and with θ that defines the angle between the velocity vector and the vertical direction. While q is the ratio between the local velocity and the speed of sound at stagnation condition c_0, c the local speed of sound divided by c_0 and ρ the ratio between the local density value and the stagnation value. The Mach contour field is shown in Fig. 3.2.2 for an approximation obtained by a tenth order polynomial. We considered the ringleb domain with stream function $k_1=0.8$ and $k_2=1.2$ and we evaluated the error with respect to the $\mathbf{L}^2(\Omega)$ norm for different domain discretizations. The accuracy and the efficiency data of this *spectral* DG approach are listed in Tab. 3.2.1 which resumes the error in norm $\mathbf{L}^2(\Omega)$ for the computed density field, the energy and the velocity along the x-direction. The solutions are refered to grids obtained as usual by a process of successive halving of the space discretization step, trials have been done for increasing order of approximation. The rate of convergence are reported in columns number six and seven for the continuity and the momentum equations, they result to be nearly optimal values in comparison with the estimates provided by the theory. The last column shows the computational time reduction related to the modified discrete operator assembly involved by the tensorial approximation functions on the co-location

Figure 3.2.2: Mach contour field; $\mathbb{P}^{10}$ approximation, solution field achieved by co-location on Lobatto nodes.

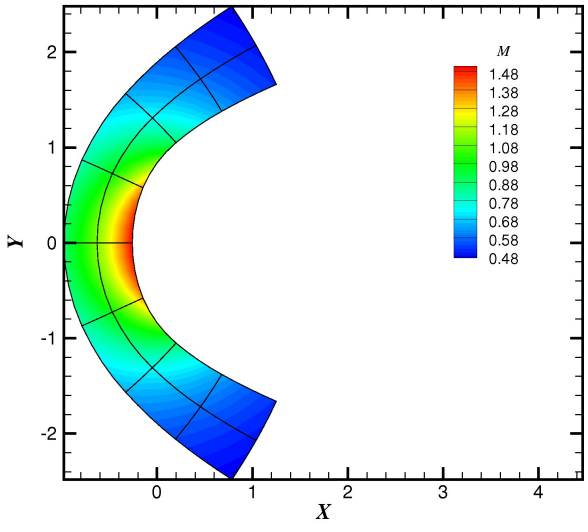

set. The percentages are relative values with respect to the time required for the operators construction before inserting the improving procedure. The enhancement is quite good even for polynomial order not too high as the forth order data show. The lack of optimality prompted the second trial with Gauss nodes as unique set either to interpolate and integrate.

Ringleb Test Case on Gauss Nodes

We therefore performed the ringleb test to adress the accuracy-efficiency trade-off using the Gauss points, less optimality from the interpolation point of view, but higher accuracy for the inner product evaluation. The results are listed in Tab. 3.2.2, the collected data are related exactly to the same conditions of the previous cases. The convergence rate is observed to almost exactly approach the expected values and however they are superior to the results provided by the tests with the Lobatto nodes. Nonetheless the computational saving is lower because of the larger number of operations related to the interface operators construction. The comparison of the behaviour of these two set is made furtherly clear by the Fig. 3.2.3 which summarizes the results of the above tables. The Gauss based algorithm allows to get

Table 3.2.1: Ringleb test case with co-location on Lobatto nodes

$\mathbb{P}^n$	Mesh	E_ρ	$E_{\rho E}$	$E_{\rho u}$	O_ρ	$O_{\rho u}$	$-\Delta\%$
3	16x8	6.82e-5	1.18e-4	2.35e-5	3.5	3.46	-78
	32x16	6.03e-6	1.08e-5	2.30e-6	3.56	3.21	
	64x32	5.10e-7	9.88e-7	2.49e-7			
4	16x8	7.23e-6	1.24e-5	2.68e-6	3.75	4.33	-84
	32x16	5.38e-7	9.12e-7	1.33e-7	4.36	4.28	
	64x32	2.62e-8	4.47e-8	6.87e-9			
5	8x4	2.07e-5	3.61e-5	1.25e-5	3.15	4.83	
	16x8	2.33e-6	3.90e-6	4.39e-7	5.92	5.74	-87
	32x16	3.86e-8	6.47e-8	8.20e-9			
6	8x4	1.83e-5	3.09e-5	5.26e-6	7.04	6.99	
	16x8	1.39e-7	2.36e-7	4.17e-8	5.58	6.19	-90
	32x16	2.92e-9	4.90e-9	5.71e-10			
8	8x4	1.76e-6	2.97e-6	4.82e-7	8.24	8.69	
	16x8	5.82e-9	9.75e-9	1.17e-9			
10	8x4	1.76e-7	2.96e-7	4.63e-8	10.51	8.14	
	16x8	1.20e-10	2.01e-10	1.64e-10			

the spectral convergence as the lin-log line shows with its linearity, while the Lobatto strategy behaves only in nearly optimal fashion. We tried to evaluate the accuracy meantime the efficiency, at this aim we present the data in Tab. 3.2.3 which contains the results for order nine and ten for both Gaussian kind of nodes. The time for the discrete operators assembly procedure is reported together with the error in norm $\mathbf{L}^2(\Omega)$ for these trials. For comparable values of the achieved errors and clearly similar accuracy, *i.e.* the $\mathbb{P}^8$ using the Gauss points choice and the $\mathbb{P}^9$ using the Lobatto, the latter approach demonstrates to give a great advantage in term of efficiency. This leads to the consideration that for sufficiently smooth field this configuration may be the right choice.

Circle test

This second test case requires to solve the inviscid Euler equations past a circle, the solution flow field should prove to be symmetric with respect to the

Table 3.2.2: Ringleb test case with co-location on Gauss nodes

$\mathbb{P}^n$	Mesh	E_ρ	$E_{\rho E}$	$E_{\rho u}$	O_ρ	$O_{\rho u}$	$-\Delta\%$
3	16x8	8.59e-6	1.53e-5	8.92e-6	4.01	3.72	-33
	32x16	5.34e-7	9.74e-7	6.75e-7	4.18	3.91	
	64x32	2.94e-8	5.53e-8	4.50e-8			
4	16x8	9.41e-7	1.66e-6	8.90e-7	5.05	4.80	-40
	32x16	2.83e-8	5.05e-8	3.19e-8	5.02	4.92	
	64x32	8.70e-10	1.56e-9	1.06e-9			
5	8x4	8.19e-6	1.40e-5	4.84e-6	6.22	6.13	
	16x8	1.10e-7	1.89e-7	6.92e-8	5.84	5.63	-46
	32x16	1.92e-7	3.29e-9	1.40e-9			
6	8x4	2.15e-6	3.65e-6	9.95e-7	6.77	6.43	
	16x8	1.97e-8	3.35e-8	1.15e-8	7.07	7.08	-50
	32x16	1.47e-10	2.50e-10	8.49e-11			
8	8x4	1.86e-7	3.15e-7	8.12e-8	8.97	8.56	
	16x8	3.71e-10	6.25e-10	2.16e-10			
10	8x4	1.74e-8	2.95e-8	7.36e-9	12.47	11.12	-66
	16x8	3.09e-12	5.58e-12	3.30e-12			

Table 3.2.3: Lobatto vs Gauss: efficiency and accuracy. Ringleb 8x4 mesh

Nodes	$\mathbb{P}^n$	Tot Tset	E_ρ	$E_{\rho E}$	$E_{\rho u}$
$\mathcal{L}$	8	27.72 s	1.76e-6	2.97e-6	4.82e-7
$\mathcal{G}$	8	70.02 s	1.86e-7	3.15e-7	8.12e-8
$\mathcal{L}$	9	30.06 s	2.39e-7	4.07e-7	7.40e-8
$\mathcal{G}$	9	96.90 s	6.39e-8	1.09e-7	3.04e-8

obstacle itself as to guarantee the entropy conservation. The computational domain has its far-limits at 20 where the *far* boundary condition is entailed while the wall is required to fulfill a *simmetric* boundary conditions. The problem has been solved using the co-location both in Gauss and in Lobatto nodes. The Gauss points allowed to reach the convergence quite strightforwardly, even almost indipendently of the grid used, while the Lobatto nodes

Figure 3.2.3: Convergence in L_2 norm as a function of the expansion order for the inviscid Ringleb test case: Gauss vs Lobatto

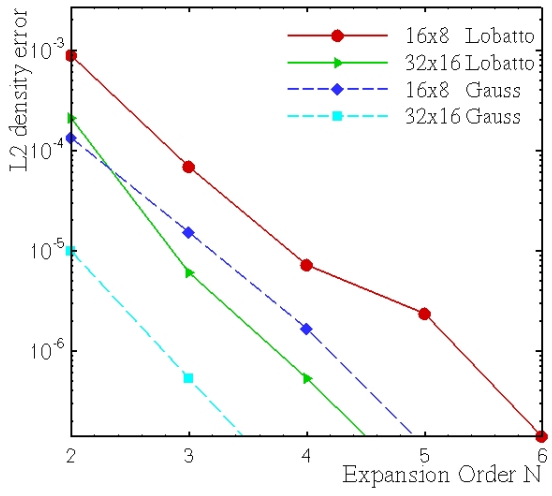

result to be a quite more delicate choice, we suggest because of the lower accuracy they provide. As a matter of fact for sufficiently accurate polynomials the problem disappears or dicreases and the solution can be obtained. The field reported in Fig. 3.2.2 is computed using Gauss nodes till order 4, and from there on using the Lobatto set, in particular the figure refers to a $\mathbb{P}^8$ approximation on a 16×8 computational mesh.

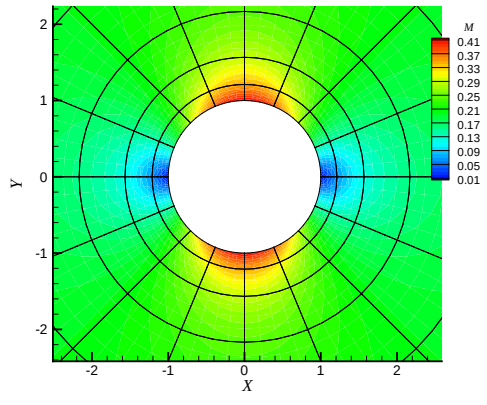

Figure 3.2.4: Mach contour for the Inviscid Circle Test Case

Bump Test Case

Another problem used for the sake of validation has been considered and here provided. The domain of this test consists in a half profile with a sinusoidal bump, the inflow is located on the left of the channel while the outflow on the right side. The reference Mach value used for the simulations amounts to 0.4. The mach flow field is reported in Fig. 3.2.5 together with its computational grid. This simulation refers to a nine-th order polynomial approximation with the co-location strategy exploiting the Lobatto nodes, although both gaussian set has been positively emploied. The considerations

Figure 3.2.5: Mach contour for the Bump Test Case, approximating function in $\mathbb{P}^8$ on the quite coarse grid shown

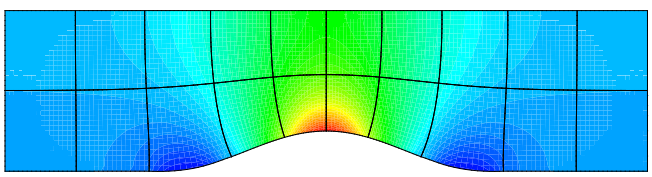

above presented and the overall behaviour of the scheme for these problems lead us to observe that for smooth enough problem, such as the motion in a channel or more generally in zones far away from strong variations, the Lobatto nodes may be advisable for their higher efficiency. However from now on we decided to use the Gauss set renouncing to a 'piece' of efficiency in virtue of the major reliability.

3.2.3 Naca0012 Test Case

The compressible Navier-Stokes equations have been considered to define the flow field around the classical Naca0012 profile. The computation has been performed on quite coarse structured grids obtained through an '$\mathcal{O}$' distribution of points around the airfoil.
The first case we considered is that of the laminar transonic flow at an angle of attack $\alpha = 10°$, freestream Mach number of 0.8, Reynolds number based on the freestream velocity of 73, with the wall temperature equal to the freestream total temperature. The *far* field is positioned at a radius of 10.

The Mach contour and the related isolines, for a polynomial approximation belonging to $\mathbb{P}^6$, are reported in Fig. 3.2.6. The adopted grid shown in figure is a 10×6 with the larger number refering to the number of elements distributed along the airfoil surface and the smaller instead defining the number of elements in the radial direction.
We successively considered the subsonic viscous flow over the Naca0012 airfoil at an angle of attack $\alpha = 0°$, free stream Mach number equal to 0.5 and a Reynolds number of 5000, such a value is near the upper limit for a steady laminar flow. The wall is assumed to be adiabatic and non-slip and it is represented by a parabolic curve. A distinguishing feature of this test case is the separation region of the flow occurring near the trailing edge which causes the formation of a small recirculation bubble that extends in the near-wake region of the airfoil, detail in Fig. 3.2.7. The solution is getting smoother and smoother with the increasing of the polynomial order of the approximating functions, indicating that the solution becomes more accurate. This behaviour may be appreciated even by observing the Tab. 3.2.4 that contains the drag coefficients, pressure and viscous componentwise, for this test case. Some reference values for these parameters are reported in the last part of the table, such values are better approached for the higher order of approximation even though the very coarse mesh used. However the accordance can be observed not to be completely achieved, the reason might be the poor geometrical representation that in fact the second order 10×8 grid offers. Hence we attempt to improve the resolution of the field solution by means of a more accurate definition of the airfoil profile, at this aim we carried out supplementary trials. In particular we used a profile of the third and a forth polynomial degree approximation, the results are resumed in the central part of the table Tab. 3.2.4 itself, showing the favourable behaviour of the better defined profile.
Further validation is provided by the following test: the study of the flow around the Naca0012 airfoil with an angle of attack of 2°, M=0.5 and Reynolds number of 5000. The performance coefficients are compared with those provided in the UNBG report for the Adigma project, MTC Test Case3. The computational mesh here shown, see Fig. 3.2.9, is just one of those tested and it is been chosen to put in evidence the performance of the code, its robustness, accuracy and efficiency. The Mach field is depicted in Fig. 3.2.9 for a $\mathbb{P}^9$ polynomial approximation, in Tab. 3.2.5 the drag and lift coefficients are listed and they might be refered to the asymptotic values presented in the above mentioned Adigma report. The $\mathbb{P}^9$ solution field is obtained by means

Figure 3.2.6: Mach contour for the Naca0012 profile M=0.8, Re=73, $\alpha = 10°$.

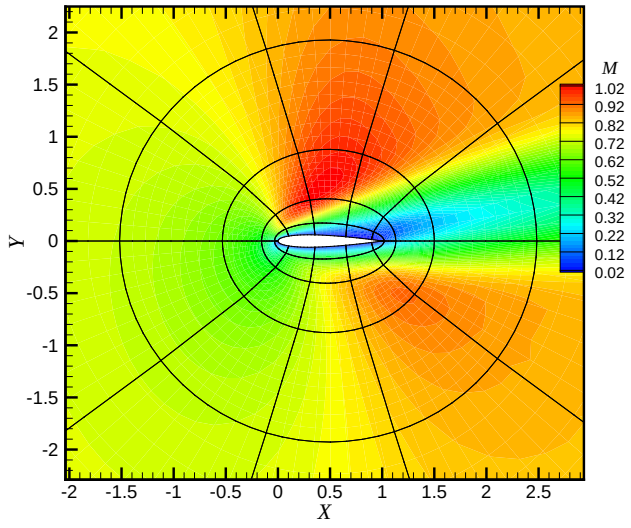

(a) Mach contour

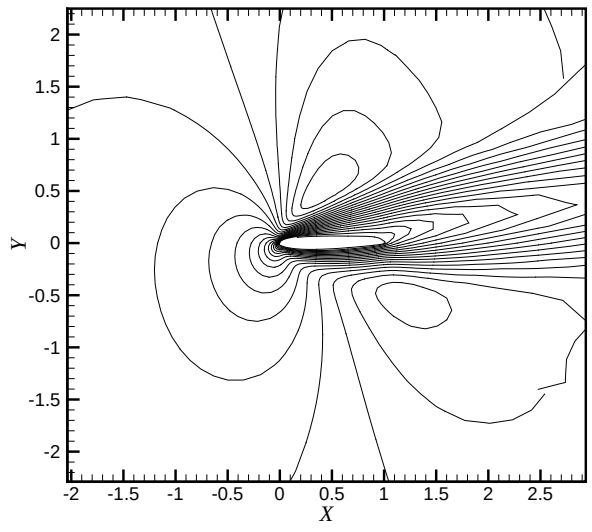

(b) Mach lines

Figure 3.2.7: Naca0012, Mach 0.5, Re=5000, $\alpha = 0°$, $\mathbb{P}^9$ approximation on a 8×4 mesh, far field at 10. Streamtrace detail: recirculation zone

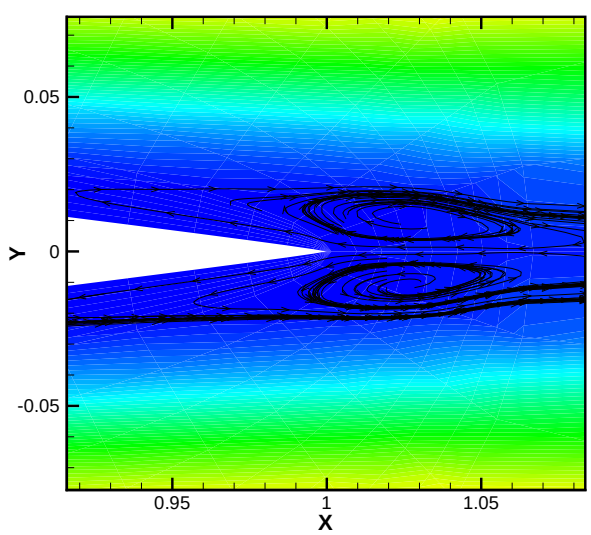

Table 3.2.4: Drag coefficient for the Naca0012 airfoil for approximation $\mathbb{P}^n$ and geometrical order of representation $\mathbb{P}^n_G$, case: M=0.5 Re=5000, $\alpha = 0°$.

Reference	$\mathbb{P}^n_G$	Grid	$\mathbb{P}^n$	$C_{D,p}$	$C_{D,v}$
	2	10x8	3	2.3698e-2	3.2228e-2
		10x8	4	2.3010e-2	3.2742e-2
		10x8	6	2.2841e-2	3.2814e-2
		10x8	8	2.2817e-2	3.2898e-2
	3	10x8	4	2.3297e-2	3.3031e-2
			5	2.2938e-2	3.2870e-2
	8	10x8	4	2.3231e-2	3.2897e-2
			5	2.2952e-2	3.2852e-2
DG ([2])		64x16	3	2.208e-2	3.303e-2
Triangle scheme ([37])		320x54		2.29e-2	3.32e-2
Cell-vertex scheme ([45])		256x64		2.27e-2	3.27e-2
Cell-centered scheme ([45])		512x128		2.235e-2	3.299e-2

Figure 3.2.8: Naca0012, Mach 0.5, Re=5000, $\alpha = 0°$, $\mathbb{P}^9$ approximation on a 8×4 computational mesh, far field located at a distance of 10.

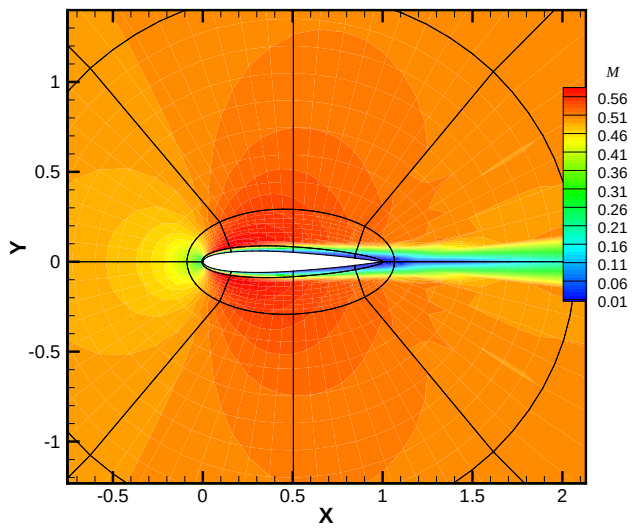

(a) Mach contour

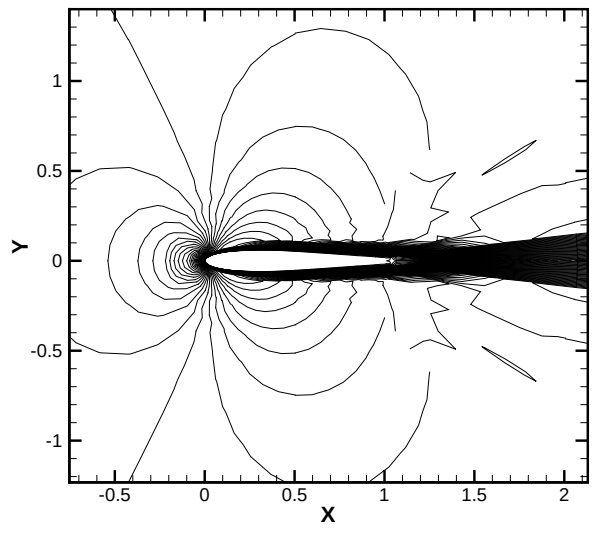

(b) Mach lines

of 3200 dof per equation while the reference field is related to a very fine grid for a $\mathbb{P}^6$ approximation with more then 250k degrees of freedom per equation, whose computation has been performed by means of eight processors. Mutuating the convergence criteria from the report, namely $|E_{C,L}| \leq 5e-3$ and $|E_{C,D}| \leq 5e-4$ for the lift and drag coefficient it is possible to add that the simulation reported in Tab. 3.2.5 shows that the $\mathbb{P}^7$ approximation would be enough to fulfill the lift required tolerance while the asymptotic drag values is reached when using the $\mathbb{P}^9$ functions. A part of the error may be due to the different geometrical profile that in fact is treated by the very fine geometry used for the reference computation and by the very poor one offered in the presented case by the 8×4 grid. In addition in Tab. 3.2.6 the same pa-

Table 3.2.5: Lift and Drag coefficient for the Naca0012 airfoil for different order of approximation, case: M=0.5 Re=5000, $\alpha = 2°$, grid 8×4.

$\mathbb{P}^n$	$C_{D,p}$	$C_{D,v}$	C_D	$C_{L,p}$	$C_{L,v}$	C_L
$\mathbb{P}^4$	2.6095e-2	3.3045e-2	5.9141e-2	6.0038e-2	5.2559e-4	6.0563e-2
$\mathbb{P}^5$	2.5699e-2	3.3209e-2	5.8909e-2	4.3912e-2	3.6511e-4	4.4277e-2
$\mathbb{P}^6$	2.5219e-2	3.3381e-2	5.8601e-2	4.5453e-2	3.8875e-4	4.5842e-2
$\mathbb{P}^7$	2.4889e-2	3.2905e-2	5.7795e-2	4.1621e-2	3.4428e-4	4.1966e-2
$\mathbb{P}^8$	2.4509e-2	3.2865e-2	5.7375e-2	4.0648e-2	3.4178e-4	4.0989e-2
$\mathbb{P}^9$	2.4331e-2	3.2693e-2	5.7024e-2	3.7085e-2	3.1850e-4	3.7404e-2
ref	2.4062 e-2	3.2635e-2	5.6697e-2	3.8368e-2	3.5992e-4	3.8728e-2

rameters are available for the $\mathbb{P}^7$ polynomial representation along with those provided by a linear functional approximation on two different finer grids. The last line still contains the reference data. The eighth order solution has been computed by means of the p-multigrid, that is going to be presented in a while, instead the second-order solution resorts to a full implicit DG scheme. They both reach an accuracy of 10^{-9} on the residual, the computation has been performed on a laptop, ram 512 Mb, whose computational times are provided for the comparison. The forth and the sixth columns define the relative error committed for the drag and the lift with respect to the asymptotic values. The balance between the achieved accuracy and required cost shows that higher order strategies may ensure accurate results together with an acceptable expense, in fact for well devised schemes they result to

Table 3.2.6: Lift and Drag coefficient for the Naca0012 airfoil, comparison between $\mathbb{P}^6$ through MG solver and $\mathbb{P}^1$ for the full implicit solution for two different grids. Case: M=0.5 Re=5000, $\alpha = 2°$. *Results obtained on 512Mb laptop*, residual down to 10^{-9}.

$\mathbb{P}^n$	Grid	C_D	$\Delta E_{C,D}$	C_L	$\Delta E_{C,L}$	Time	Solver
$\mathbb{P}^1$	64×32	5.8586e-2	3.33%	5.4457e-2	40.61%	$4m33s$	Impl
$\mathbb{P}^1$	96×48	5.7523e-2	1.45%	4.8520e-2	25.28%	$18m$	Impl
$\mathbb{P}^7$	8×4	5.7790e-2	1.92%	4.2063e-2	8.61%	$10m13s$	p-MG
ref		5.6697e-2		3.8728e-2			

be competitive approaches.

3D test: ls 89 blade

For the sake of validation a three dimensional test, which is a part of a still in progress work is also presented. The Mach contour shown in Fig. 3.2.10 and its section refer to a model simple case with Reynolds number equal to 100 and reference Mach number of 0.3 for the turbine blade "ls 89" taken in periodic configuration. The right and the left wall are entailed to satisfy the no-slip condition, the blade is assumed to be an adiabatic wall. The coarse grid shown is made of 68 elements, the span has just been halfed. The approximation is forth order accurate.

3.2.4 p-Multigrid Method

The classical iterative methods for the numerical solution of the system $A\boldsymbol{x} = \mathbf{g}$ result to be all characterized by the following behaviour: during the first iterations we have the maximum rate of convergence after these we can observe an important decreasing in the resolution effectiveness. This phenomenon is due to the efficient elimination of the oscillatory modes of the error, once these components have been removed the efficiency of the error reduction with respect to the remaining smooth components soon becomes unsatisfactory. This damping factor for the oscillatory modes is an important property of any relaxation scheme and it is named *smoothing factor* of the scheme. Such a situation can be better understood just by considering the

Figure 3.2.9: Mach contour for the Naca0012 test case with M=0.5 Re=5000, $\alpha = 2^\circ$ on the 8×4 grid. $\mathbb{P}^7$ approximation obtained through the p-multigrid, data in Tab. 3.2.6.

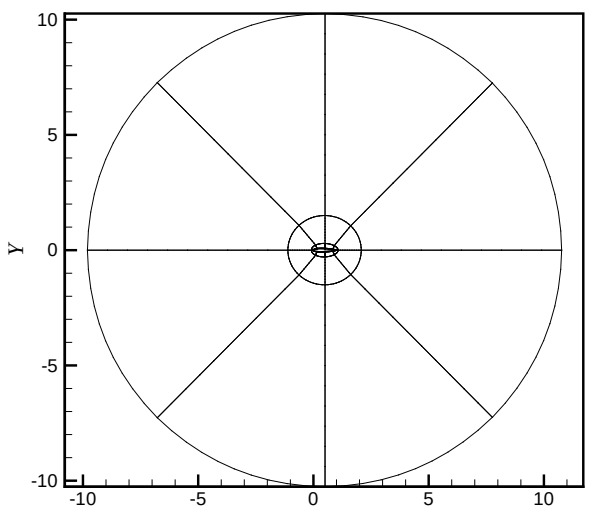

(a) Grig 8×4

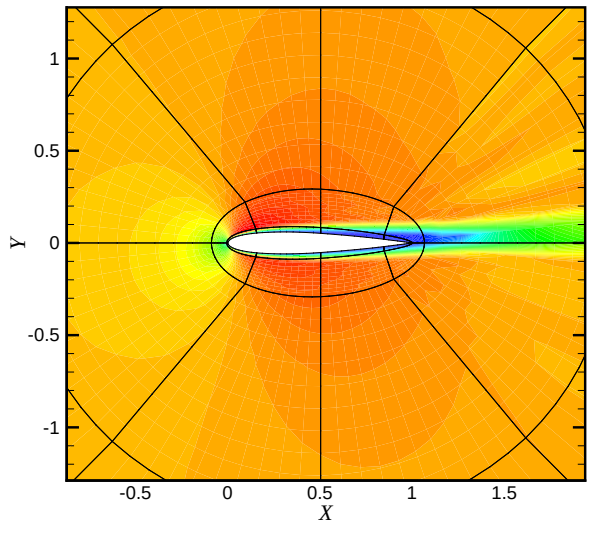

(b) Mach contour

Figure 3.2.10: Mach contour for $LS89$ blade for a grid of 68 elements for $\mathbb{P}^3$ approximation

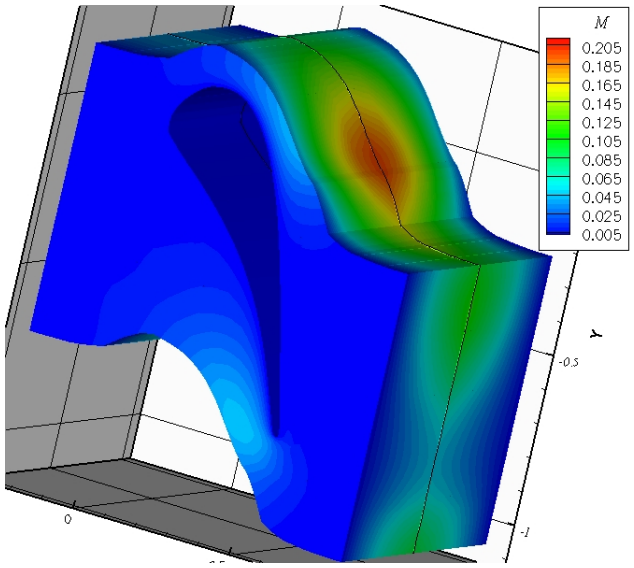

(a) Mach contour

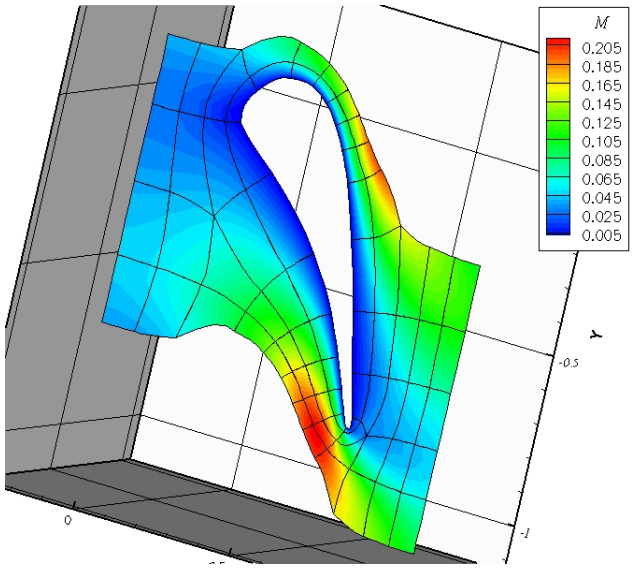

(b) Detail at the middle of the span

generic iterative method,

$$\boldsymbol{x}^{k+1} = \boldsymbol{x}^k + B\boldsymbol{r}^k,$$

where $\boldsymbol{r}^k$ defines the residual at the k-th iteration and by definition $\boldsymbol{r} = \mathbf{g} - A\boldsymbol{x}$. Subtracting this equation from the exact solution $\mathbf{u}$ gives the error of the $(k+1)$-th step,

$$\boldsymbol{e}^{k+1} = \boldsymbol{e}^k + B\boldsymbol{r}^k,$$

the change in error is made with spatially local corrections coming from the residual, since smooth modes have smooth residual the change in the error will be of the same order, originating therefore the slow convergence.
Two strategies facing this problem are mentioned, first we can look for a better guess solution using a starting coarser grid which allows to exploit the advantage coming from the more favourable convergence factor, which goes like $1 - o(h^2)$, being h the step size of the computational grid. Secondarily the fix for this selective behaviour shown in correspondence of different frequencies, may be found in the so called *correction scheme*. In this approach at the outset we relax on the original problem for some steps till the slowing down is observed. Then we somehow transfer the residual on a coarser grid where it will take a more oscillatory apparence, and hence it will be there efficiently damped by the iterative scheme. After this relaxation sweep the error so computed is transfered back to the fine mesh and used to correct the first solution. This procedure is summarized as follows

$$\begin{aligned} &\text{Solve } A\boldsymbol{x} = \mathbf{g} \Rightarrow A\boldsymbol{e} = \boldsymbol{r} : \\ &\text{relax } \ A\boldsymbol{x} = \mathbf{g} \quad \text{on } \Omega_h \rightarrow \mathbf{v}_h \\ &\text{compute } \boldsymbol{r} = \mathbf{g} - A\mathbf{v}_h \Rightarrow \text{relax } \ A\boldsymbol{e} = \boldsymbol{r} \quad \text{on } \Omega_{2h} \\ &\text{correction } \mathbf{v}_h + \boldsymbol{e}_{2h} \rightarrow \mathbf{v}_h \end{aligned} \tag{3.2.5}$$

Hence the solution of the system $A\boldsymbol{x} = \mathbf{g}$, which corresponds to $A\boldsymbol{e} = \boldsymbol{r}$, damps the oscillatory part of the error during the first few iterations on the finer grid, then the remaining smooth part responsible of the computational time increase is transformed in order to effectively be cancelled out. Such a kind of strategy has been named multigrid technique and many variants has been devised. The entire family of multigrid cycling schemes has been classified as μ-cycle method, inside it we can find the V cycle, the W cycle and the full multigrid V-cycle. The transfering mechanism between grids of

Table 3.2.7: Comparison between the full p-multigrid with or without the enhancing spectral tensorial co-location strategy.

Test case	MG	MG+TP	$-\Delta\%$
Inviscid naca0012, M=0.5, $\alpha = 0$, 16x8, $\mathbb{P}^{0\to6}$	3m 40s	1m 38s	-55%
Inviscid Circle, 16x8, $\mathbb{P}^{0\to6}$	3m 03s	1m 25s	-53%
Inviscid Bump, 12x2, $\mathbb{P}^{0\to9}$	11m 15s	3m 22s	-70%
Viscous naca0012, M=0.5, $\alpha = 0$, 16x8, $\mathbb{P}^{0\to3}$	5m 10s	3m 01s	-41%

different size is usually described by means of the so called *prolongation* and *restriction* operators $\mathscr{I}_{2h}^{h}$ and $\mathscr{I}_{h}^{2h}$.
An improved convergence may even be achieved by varing the polynomial order during the resolution process in place of the grid size, in this case the method is called p-multigrid or originally multi-order. The spectral DG precedingly introduced exploits such a kind of solution strategy, in particular the high-accurate p-multigrid presented in [7] has been used. This algorithm is based on a semi-implicit Runge-Kutta smoother for high-order polynomial approximations and on a fully implicit backward-Euler for piecewise approximations. The Tab. 3.2.7 shows the time necessary to achieve the convergence, *i.e.* the residual down to 10^{-10}, for some of test cases already introduced for the number of levels outlined, $\mathbb{P}^{(\cdot)\to(\cdot)}$. The first value is the time required by the p-multigrid itself to reach the solution field, while the second is refered to the computational load required by the same p-multigrid scheme exploiting the tensorial strategy on co-located elements detailed in §3.2. The computational enhancement is expressed by the relative percentages reported in the last column. The listed values are related to trials performed on a laptop, $512Mb$ and 1.5GHz clock frequency.

Chapter

4 Semi-implicit RK for the INS eqs

In this chapter the solution of the incompressible Navier-Stokes equations is considered. After a first characterization of the problem from a mathematical and numerical point of view, some existing algorithms are described. In the second part the new semi-implicit solution strategy is presented and its accuracy has been assesed by means of a series of numerical model cases.

4.1 Incompressible NS equations

The Navier-Stokes equations are the governing partial differential equations for the motion of many fluids, they originally stated only the conservation of the momentum although they now usually define the mass conservation too. If we consider an isothermal Newtonian fluid with constant properties the Navier-Stokes system written in terms of the primitive variables, velocity and pressure, can be compactly written as

$$\begin{aligned} &\frac{\partial \mathbf{u}}{\partial t} + \mathbf{u} \cdot \nabla \mathbf{u} = \nu \boldsymbol{\Delta} \mathbf{u} - \nabla p + \mathbf{g} \\ &\nabla \cdot \mathbf{u} = 0, \qquad \mathbf{u} = 0 \quad \text{on} \quad \partial\Omega, \end{aligned} \tag{4.1.1}$$

where p is the kinematic pressure field, $\mathbf{u}$ the velocity field, ν the kinematic viscosity and $\boldsymbol{g}$ the body force. Boundary condition of pure Dirichlet kind has been provided in this introduction for the sake of semplicity. The solution process of the INS equations results to be more complicated, both theoretically and computationally, than that related to compressible fluid flows, the reason should mainly refered to the mathematical nature of the problem itself. It is an incomplete parabolic system in which the pressure and the velocity field are strongly coupled. Another source of difficulty comes from the inherent non-linearity which may be responsible for instability phenomena. In order to better understand the feature of the problem we are dealing with, we consider the non-dimensional form of the NS equation, as

$$\frac{\partial \mathbf{u}}{\partial t} + \mathbf{u} \cdot \nabla \mathbf{u} = \frac{1}{\mathrm{Re}} \boldsymbol{\Delta} \mathbf{u} - \nabla p, \tag{4.1.2}$$

being Re, the Reynolds number $\mathrm{Re} = \rho \mathbf{u} L/\mu$, the dimensionless number that expresses the ratio of convection to diffusion. The limiting cases are the Stokes flow for vanishing Reynolds number and the inviscid Euler case in the opposite situation.
An alternative form of the Navier-Stokes problem can be obtained by rewriting the equations in terms of the velocity $\mathbf{u}$ and the vorticity $\omega = \boldsymbol{\nabla} \times \mathbf{u}$, therefore by assuming the fluid to be endowed of constant properties the system reads

$$\begin{aligned} \frac{\mathrm{D}\omega}{\mathrm{D}t} &= (\boldsymbol{\nabla} \cdot \omega)\mathbf{u} + \nu \boldsymbol{\Delta} \omega \quad \text{in } \boldsymbol{\Omega}, \\ \boldsymbol{\Delta} \mathbf{u} &= -\boldsymbol{\nabla} \times \mathbf{u} \quad \text{in } \Omega, \\ \boldsymbol{\nabla} \cdot \mathbf{u} &= 0 \quad \text{in } \Omega, \\ \omega &= \boldsymbol{\nabla} \times \mathbf{u} \quad \text{in } \Omega. \end{aligned} \tag{4.1.3}$$

This formulation results to be more general than the standard vorticity-streamfunction which instead is limited to two-dimensional cases.
The further understanding of the peculiarities of the NS equations is nextly provided by the decomposition of the original problem in subproblems each of them taking into account a different aspect of the whole system. In detail the linear Stokes equations are first considered just to deal with the pressure-velocity coupling. Afterwards the steady NS by reintroducing the nonlinear contribution of the advective component, at the end the discretization in time process is discussed.

The Stokes Problem

The steady Stokes equations accounts for the diffusive behaviour of the motion of a general fluid flow, often called creeping flow, and they can be written as

$$\begin{aligned} -\nu \boldsymbol{\Delta} \mathbf{u} + \nabla p &= \mathbf{g} \quad \text{in } \Omega \\ \nabla \cdot \mathbf{u} &= 0 \quad \text{in } \Omega \\ \mathbf{u} &= 0 \quad \text{on } \partial\Omega. \end{aligned} \tag{4.1.4}$$

This equations results to be useful either for theoretical analysis purposes or for numerical method assesments, they gain advantage from the absence of the convective contribution in allowing to only investigate the div-grad coupling without the complication induced by the non-linearity effect. The

variational form of the Stokes problem can then be obtained as usual by considering the integral form of the equations. Multipling them by a suitable test function and by performing an integration by parts, the resulting equations read as follows

$$\begin{aligned} \nu \int_\Omega \boldsymbol{\nabla}\mathbf{u} : \boldsymbol{\nabla}\mathbf{v} \, \mathrm{d}\mathbf{x} - \int_\Omega p\boldsymbol{\nabla}\cdot\mathbf{v} \, \mathrm{d}\mathbf{x} = \int_\Omega \boldsymbol{g}\cdot\mathbf{v} \, \mathrm{d}\mathbf{x} \quad \forall \mathbf{v} \in V \\ \int_\Omega q\boldsymbol{\nabla}\cdot\mathbf{u} \, \mathrm{d}\mathbf{x} = 0 \quad \forall q \in Q \end{aligned} \tag{4.1.5}$$

with $V = H_0^1(\Omega)$, Hilbertian space of order one with null trace on the boundary and with $Q = L_0^2(\Omega)$. The zero subscript stands for the null average of q on the domain Ω which entails the pressure to be uniquely defined. The existence matter can be treated by resorting to the decomposition of the original problem in subparts simpler to consider [44]. We first take into account the bilinear form $\nu(\boldsymbol{\nabla}\mathbf{v}, \boldsymbol{\nabla}\mathbf{u})$ which can be proven to be coercive, this property along with the fact that the application of the right hand side of the momentum equation of the (4.1.5) $\mathbf{v} \to (\boldsymbol{g}, \mathbf{v})$ is linear and continuous makes the viscous problem $\nu(\boldsymbol{\nabla}\mathbf{v}, \boldsymbol{\nabla}\mathbf{u}) = (\mathbf{v}, \boldsymbol{g})$ admit a unique solution, (the result is obtained by virtue of the Lax-Milgram theorem). For the remaining part of the first equation in (4.1.5) *i.e.* $(p, \boldsymbol{\nabla}\cdot\mathbf{v})$ let L be an element of V' then this functional identically vanishes on V_{div} if there exists a unique function $p \in L^2(\Omega)$ up to an additive constant such that

$$L(\mathbf{v}) = (p, \boldsymbol{\nabla}\cdot\mathbf{v}), \quad \forall \mathbf{v} \in V,$$

with $V_{\mathrm{div}} := \{H_0^1(\Omega), \boldsymbol{\nabla}\cdot\mathbf{u} = 0\}$. These two steps are resumed in the following theorem:

Theorem 6 *Let Ω be a bounded domain in $\mathbb{R}^{\mathrm{d}}$ with a Lipschitz continuous boundary and for each $\boldsymbol{g} \in L^2(\Omega)^d$ let $\mathbf{u}$ be the solution to $\nu(\boldsymbol{\nabla}\mathbf{v}, \boldsymbol{\nabla}\mathbf{u}) = (\mathbf{v}, \boldsymbol{g})$, then there exists a function $p \in L^2(\Omega)$, which is unique up to an additive constant, such that*

$$\nu(\boldsymbol{\nabla}\mathbf{v}, \boldsymbol{\nabla}\mathbf{u}) - (p, \boldsymbol{\nabla}\cdot\mathbf{v}) = (\boldsymbol{g}, \mathbf{v}).$$

Another interesting approach to the Stokes problem is obtained by starting from the weak form provided by the (4.1.5) compactly considered as

$$\begin{aligned} a(\mathbf{u}, \mathbf{v}) + b(\mathbf{v}, p) = (\boldsymbol{g}, \mathbf{v}) \quad \forall \mathbf{v} \in V \\ b(\mathbf{u}, p) = 0 \qquad \forall p \in Q, \end{aligned} \tag{4.1.6}$$

for which there still exists a unique solution, with the pressure defined up to a constant. As before the pressure field can be uniquely computed by modifing the space in which it is looked for, namely entailing the pressure to have a zero average, $p \in L^2_0(\Omega)$; alternatively one can decide to fix its value in one point. The proof of the fact that the solution field $(\mathbf{u}, p)$ of the weak form of the linear NS equations (4.1.6) is also the solution of the original differential problem has been led by density arguments.
The solution of the Stokes problem can even resort to interesting variational statements which once more reveal the strong pressure-velocity link and their mutual constrained evolution. In particular the solution field $(\mathbf{u}, p)$ can be achieved from the minmax problem related to the linear NS system itself, namely a minimization problem plus a constraint,

$$\begin{aligned} \mathcal{L}(\mathbf{v}, q) &:= \frac{1}{2} a(\mathbf{v}, \mathbf{v}) + b(\mathbf{v}, q) - (\boldsymbol{g}, \mathbf{v}), \quad \mathbf{v} \in \mathbf{V},\ q \in Q, \\ \mathcal{L}(\mathbf{u}, p) &:= \min_{v \in \mathbf{V}} \max_{q \in Q} \mathcal{L}(\mathbf{v}, q). \end{aligned} \tag{4.1.7}$$

The extremum, which is the solution we are looking for, represents the minimizer over all $\mathbf{u}$ and the maximizer over all p taken in L^2 of the functional $\mathcal{L}$ given in (4.1.7) which is nothing but an alternative way of writing the Stokes equations.
The discretization process is then performed by considering the Galerkin approximation of the system (4.1.6), *i.e.* find $\mathbf{u}_h \in \mathbf{V}_h$ and $p_h \in Q_h$, eq. (2.3.2), such that

$$\begin{aligned} a(\mathbf{u}_h, \mathbf{v}_h) + b(\mathbf{v}_h, p_h) &= (\boldsymbol{g}, \mathbf{v}_h) \quad \forall \mathbf{v}_h \in \mathbf{V}_h \\ b(\mathbf{u}_h, p_h) &= 0 \qquad \forall p_h \in Q_h, \end{aligned} \tag{4.1.8}$$

where the approximated pressure and velocity solutions are taken to be of the polynomial form presented in the preliminary definition in §1.2 by Def. 3, with $\boldsymbol{\varphi}_i$, $i = 1, N_{\mathrm{DOFu}}$ the basis for the velocity and $\boldsymbol{\psi}_j$, $j = 1, N_{\mathrm{DOFp}}$ for the pressure. The algebraic system associated to the discrete formulation given above by the (4.1.8) is usually written as

$$\begin{bmatrix} A & B^T \\ B & 0 \end{bmatrix} \begin{pmatrix} \mathbf{u}^{n+1} \\ \boldsymbol{p}^{n+1} \end{pmatrix} = \begin{pmatrix} f^{n+1} \\ 0 \end{pmatrix}, \tag{4.1.9}$$

the matrix are componentwise defined by comparison with the preceding expressions as

$$A_{ij} = a(\boldsymbol{\varphi}_i, \boldsymbol{\varphi}_j),\ B_{li} = b(\boldsymbol{\varphi}_i, \boldsymbol{\psi}_l),\ f_i = (\boldsymbol{f}, \boldsymbol{\varphi}_i), \tag{4.1.10}$$

where the bilinear form are directly obtained from the (4.1.5) and the (4.1.6) comparison. The matrix A is usually called stiffness matrix, while B^T the discrete gradient operator and B the discrete divergence operator. The solution of the system (4.1.9) undergoes to requirements on the matrix in order to prevent its singularity. In particular the classical finite element strategy requires the satisfaction of the well known inf-sup condition. In practice the allowable functional spaces for the pressure and the velocity approximation to be stable are defined. This condition is usually ensured by a mixed interpolation approach, in particular the velocity is chosen to belong to a richer space than that accomodating the pressure field. In the finite volume method the stability is instead obtained by employing staggered grids for the two unknown variables. The violation of such a requirement leads to unstable and oscillating solutions, in particular it gives rise to spurious pressure modes. Other stabilization techniques have been devised which allow to use equal order of approximation, such a kind of methods are going to be described in the next sections along with the most adopted solution strategies for the resolution of the Navier-Stokes equations. For the discontinuous Galerkin method the inf-sup or LBB condition is not required hence restriction on the basis functions has not to be entailed. Once the solvability of the system (4.1.10) has been somehow achieved it is possible to compute the solution field $(\mathbf{u}, p)$, which is formally obtained as

$$\begin{aligned} \mathbf{u} &= A^{-1}(\boldsymbol{g} - B^T \boldsymbol{p}), \\ BA^{-1}B^T \boldsymbol{p} &= BA^{-1}\boldsymbol{g}. \end{aligned} \tag{4.1.11}$$

The Navier Stokes problem

The weak form of the NS equations can be obtained just by re-introducing the non-linear advective part into the (4.1.6), namely

$$\begin{aligned} a(\mathbf{u}, \mathbf{v}) + c(\mathbf{u}; \mathbf{u}, \mathbf{v}) + b(\mathbf{v}, p) &= (\boldsymbol{g}, \mathbf{v}) \quad \forall \mathbf{v} \in \mathbf{V} \\ b(\mathbf{u}, p) &= 0 \qquad \forall p \in Q, \end{aligned} \tag{4.1.12}$$

where the trilinear form $c(\cdot;\cdot,\cdot)$ is related to the non-linear convective term, the Hilbert spaces for the discrete solution are chosen as before as $\mathbf{V} = H_0^1(\Omega)$ and $Q = L_0^2(\Omega)$. Similarly to what has been done for the Stokes problem we can reformulate the steady NS system as made up of two sub-steps, the first one that neglects the pressure contribution and a second one that accounts for

it. This procedure still allows to make some considerations on the existence of the solution. For the former sub-part,

$$a(\mathbf{u},\mathbf{v}) + c(\mathbf{u};\mathbf{u},\mathbf{v}) = (\boldsymbol{g},\mathbf{v}) \quad \forall \mathbf{v} \in V_{\text{div}} \tag{4.1.13}$$

being V_{div} the subspace of $\mathbf{V}$ of divergence free functions, it has been proven that if $\mathbf{u}$ solves this equation then there exists a p such that $(\mathbf{u}, p)$ is a solution to the original problem (4.1.12). The converse is also true, namely if $(\mathbf{u}, p)$ is a solution of the NS system then $\mathbf{u}$ solves the above equation, the proofs can be found in [44]. Finally for the sake of completness it remains only to consider the unsteady contribution which makes the Navier-Stokes equations (4.1.1) read as follows:

$$\begin{aligned}(\mathbf{u}(t),\mathbf{v})_{,t} + a(\mathbf{u}(t),\mathbf{v}) + c(\mathbf{u}(t);\mathbf{u}(t),\mathbf{v}) + b(\mathbf{v},p(t)) &= (\boldsymbol{g}(t),\mathbf{v}) \\ b(\mathbf{u}(t),p) &= 0\end{aligned} \tag{4.1.14}$$

for all $\mathbf{v}(t) \in \mathbf{V}$ and $p(t) \in Q$, in $t \in [0,T]$, with $\mathbf{u}(0) = \mathbf{u}_{0,h}$. The solution of (4.1.14) has been proved to exist by Leray in 1934 and Hopf in 1951 by means of considerations similar to those presented previously for the Stokes problem and the steady Navier-Stokes. On the other hand the uniqueness still remains an open question for the three dimensional case whereas in two-dimension the solution has shown to belong to $C^0([0,T];H_{\text{div}})$ and to be unique. Under additional assumptions it is also possible to demonstrate the existence of more regular solutions.
The discrete Galerkin approximation of the unsteady NS can be reached by considering two suitable subset $\mathbf{V}_h \in \mathbf{V}$ and $Q_h \in Q$ where the solution $(\mathbf{u}_h(t), p_h(t))$ is assumed to be an expansion such the one introduced by Def. 3. Extensive analysis has been carried on about the discretization in order to recover suitable error estimates such as

$$||\mathbf{u}(t) - \mathbf{u}_h(t)||_0 \leq C_1(t)h^k, \qquad ||p(t) - p_h(t)||_0 \leq C_2(t)h^{k-1}, \tag{4.1.15}$$

for $k = 2, .., 5$, clearly provided the finite dimensional spaces have been chosen with the associated approximability property. Such bounds must undergo to requirements on the initial data, these values have to fulfill a compatibility condition on the boundary, in particular if the $H^3(\Omega)$-norm of $\mathbf{u}(t)$ remains bounded up to $t = 0$ the external force field $\boldsymbol{g}$ and the initial velocity field must be such that

$$\boldsymbol{\nabla} p_0 = \boldsymbol{g} + \nu \boldsymbol{\Delta} \mathbf{u}_0 \quad \text{on } \partial\Omega, \tag{4.1.16}$$

with p_0 solution to the Neumenn problem

$$\begin{aligned} \boldsymbol{\Delta} p_0 &= -\boldsymbol{\nabla} \cdot [(\mathbf{u}_0 \cdot \boldsymbol{\nabla})\mathbf{u}_0)] \quad \text{in } \Omega \\ \frac{\partial p_0}{\partial n} &= \nu \boldsymbol{\Delta} \mathbf{u}_0 \cdot n \quad \text{on } \partial\Omega, \end{aligned} \tag{4.1.17}$$

with $\mathbf{g} \in H_{\text{div}}$. In fact such a condition can not easily be checked , therefore the only condition to satisfy is the solenoidality condition for the initial velocity field,

$$\begin{aligned} \boldsymbol{\nabla} \cdot \mathbf{u}_0 &= 0 \quad \text{in } \Omega \\ \boldsymbol{n} \cdot \mathbf{u}_0 &= \boldsymbol{n} \cdot \boldsymbol{w}_0 \quad \text{in } \Gamma_D, \end{aligned} \tag{4.1.18}$$

where Γ_D defines the portion of the boundary on which the normal velocity $\boldsymbol{n} \cdot \boldsymbol{w}_0$ condition is specified. The normal condition reported above states that no impulsive changes in the normal directions are permissible unless the violation of the div-free requirement, meantime the impulsive changes result admissible for the tangential component. Such a situation is responsible of the vortex sheet phenomenon on the no-slip boundaries. The initial pressure has instead no initial conditions to satisfy, it stems that its value is determined by the velocity field itself.
We hence got the discrete in space, but still continuous in time, algebraic form of the NS equations that reads

$$\begin{aligned} M\frac{d\mathbf{u}}{dt}(t) - A\mathbf{u}(t) + C(\mathbf{u}(t))\mathbf{u}(t) + B^T\boldsymbol{p}(t) &= \mathbf{g}(t) \\ B\mathbf{u}(t) &= \mathbf{0}, \end{aligned} \tag{4.1.19}$$

with $\mathbf{u}(0) = \mathbf{u}_0$ and whose matrices are componentwise given by

$$\begin{aligned} M_{ij} &= \int_\Omega \boldsymbol{\varphi}_i \cdot \boldsymbol{\varphi}_j \, \mathrm{d}\mathbf{x}, \qquad A_{ij} = a(\boldsymbol{\varphi}_i, \boldsymbol{\varphi}_j), \quad B_{li} = b(\boldsymbol{\varphi}_i, \boldsymbol{\psi}_l), \\ C(\mathbf{W})_{ij} &= \sum_{m=1}^{N\text{dof}\mathbf{u}} \int_\Omega (\boldsymbol{\varphi}_m \cdot \boldsymbol{\nabla})\boldsymbol{\varphi}_j \cdot \boldsymbol{\varphi}_i \, \mathrm{d}\mathbf{x}, \qquad f_i = (\boldsymbol{f}, \boldsymbol{\varphi}_i), \end{aligned} \tag{4.1.20}$$

where $\boldsymbol{\varphi}_i$ is the $i-$th basis function for the velocity belonging to $\mathbf{V}_h$ and $\boldsymbol{\psi_j}$ the j-th function for the pressure taken in Q_h.
After performing a suitable time discretization and a linearization for the convective part we get the final algebraic system $A\mathbf{x} = \mathbf{b}$, to be numerically solved; before starting the discussion about this we shortly recall how to handle the time variations.

Time Discretization Process

The time discretization process can be performed by means of suitable finite difference schemes or simply by considering the time just as it were another variable. In this work we will exploit only the first approach and a brief description of the schemes that will be used is provided. The NS equations discretized in space can be advanced in time using for example the single step θ-scheme, therefore the system (4.1.19) becomes

$$\begin{aligned} M\frac{\mathbf{u}^{k+1}-\mathbf{u}^k}{\Delta t} + C(\mathbf{u}_\theta^{k+1})\mathbf{u}_\theta^{k+1} - A\mathbf{u}_\theta^{k+1} + B^T p^{k+1} &= \mathbf{g}_\theta^{k+1} \\ B\mathbf{u}^{k+1} &= 0. \end{aligned} \tag{4.1.21}$$

The superscript n identifies the present instant time t, while $n+1$ the subsequent instant $t+\Delta t$, $\mathbf{u}_\theta^{k+1} = \theta\mathbf{u}^{k+1} + (1-\theta)\mathbf{u}^k$ and similarly $p_\theta^{k+1} = \theta p^{k+1} + (1-\theta)p^k$ and $\mathbf{g}_\theta^{k+1} = \mathbf{g}(\theta t^{k+1} + (1-\theta)t^k)$, $0 \le \theta \le 1$ are the values of these variables evaluated at an intermediate instant between the old time t^k and the new one t^{k+1}. The level of implicitness is provided by the value of the parameter θ which characterizes the scheme from an accuracy and stability point of view. For example with $\theta = 1/2$ we get the Cranck-Nicolson scheme which is second order accurate, while other values of θ yield just a first order accuracy, for $\theta = 0, 1$ we have the well-known forward and backward Euler time stepping. Implicit schemes give nonlinear settings which can be dealt with the standard Newton linearization process. One way to avoid the computational effort of fully implicit scheme is to resort to *semi-implicit* methods, *e.g.* evaluating the advective term as $C(\mathbf{u}_\theta^k)\mathbf{u}_\theta^{k+1}$, or even to the straightforward explicit approach *i.e.* $C(\mathbf{u}_\theta^k)\mathbf{u}_\theta^k$. The latter choice is often associated with a spectral collocation method. The main advantages of an explicit scheme are the easy parallelization of the code and the small memory requirement, although they pay off through the restricive stability condition.

Higher accuracy can be achieved using a multistep technique which is based on the use of wider stencils during the time derivatives discretization process, this amounts to consider higher order Taylor expansions. Among these schemes we mention the *backward difference formulae*, shortly BDF,

$$\frac{\mathrm{d}\mathbf{u}}{\mathrm{d}t} \approx \frac{\gamma_0\mathbf{u}^{k+1} - \sum_{q=0}^{j-1}\alpha_q\mathbf{u}^{k-q}}{\Delta t} \tag{4.1.22}$$

with $\gamma_0 = \sum_{q=0}^{j-1}\alpha_q$ for consistency. Such schemes are recognised to be *stiffly stable*, namely absolutely stable in the left immaginary plane in the stability

diagram and accurate for all components around the origin. These schemes are implicit but it is also possible to use a mixed explicit/implicit treatment of the advective/diffusive contributions. In addition we also mention that the BDF schemes are endowed of a larger stability region than that associated to either Adams-Bashforth or Adams-Moulton of corresponding order.
An increasing accuracy can be obtained also using a compact stancil just by performing more than one functional evaluation of the discrete operator for each time step, as the Runge Kutta (RK) schemes do, the general form reads

$$\begin{aligned} U_h^0 &= U_h^k \\ U_h^{(i)} &= \sum_{k=0}^{i-1} (\alpha_{ik} U_h^{(k)} + \Delta t \beta_{ik} L(U_h^{(k)})), \quad i = 1, 2, ..s \\ U_h^{k+1} &= U_h^{(s)}, \end{aligned} \tag{4.1.23}$$

for a scheme of s stages, with parameters α_{ik} and β_{ik} fulfilling stability and accuracy conditions. This method does not require an initialization or start-up procedure and the time step can be altered dynamically. The new semi-implicit algorithm subsequently presented in this chapter adopted an additive semi-implicit RK scheme, we postpone its description at the aim to join it with the method itself, refer to ([50]).

4.2 INS solution strategies

The Navier-Stokes system discretized in space and time $A\mathbf{x} = \mathbf{b}$ requires suitable strategies to be effectively solved. As we have already reported in the preceding section, classical continuous methods, like the finite element method and the spectral method, undergo to the satisfaction of the compatibility condition which leads to stable computation and, under suitable assumptions, allows these methods to achieve good convergence results. However even schemes violating the inf-sup condition can be employed successfully by resorting to stabilization technique. The different available strategies can be divided into two main categories, the methods which mantain the pressure-velocity coupling and those which perform a decomposition of the original problem in order to try to deal with sub-problems easier to solve. The latter way of proceeding results to be most effective for problems characterized by high Reynolds number values, as a matter of fact in this cases the velocity error scales with $\nu \Delta t$, smaller the higher the Re number.

In the remainder of this paragraph we will consider either coupled or splitted strategies, trying to outline the most important peculiarities of each of them. In particular we are first going to show some stabilization methods whose main purpose is to suitably introduce a perturbation in the continuity equation in order to prevent the singularity of the resolution matrix or its instability. Next the description of the splitting methods, *i.e.* projection, pressure Poisson, fractional-step, or even operator splitting follows.
A quite complete survey about the incompressible Navier-Stokes equations is provided by [35] while a very extensive source is given by Gresho and Sani, [26], see also [27], [28], [29]. We have also made reference to [31].

4.2.1 Incompressibility constraint relaxation

The solution of the Navier-Stokes equations can be performed without resorting to staggered grids or mixed interpolating functions for the velocity and the pressure, in fact such a strategies may be a little cumbersome mainly for example when adaptivity is performed. Therefore a suitable perturbation can be introduced at the aim to achieve a stabilization of our problem, $A\boldsymbol{x} = \boldsymbol{b}$,

$$\begin{bmatrix} C & B^T \\ B & \epsilon \boldsymbol{R} \end{bmatrix} \begin{pmatrix} \mathbf{u} \\ p \end{pmatrix} = \begin{pmatrix} \mathbf{f} \\ \epsilon \boldsymbol{r} \end{pmatrix} \tag{4.2.1}$$

where the matrix C has been assumed to sum up the unsteady contributions, the advective and the diffusive terms, while B and B^T has instead mantained the previously defined meaning. The quantity $\epsilon \boldsymbol{R}$ defines the stabilization matrix, with ϵ representing a tuning parameter of the perturbation entity, $\epsilon \boldsymbol{r}$ a possible perturbation of the right hand side. The most adopted procedures are listed below

$$\boldsymbol{\nabla} \cdot \mathbf{u} = \epsilon \boldsymbol{\Delta} p, \tag{4.2.2a}$$

$$\boldsymbol{\nabla} \cdot \mathbf{u} = -\frac{1}{\lambda} p, \tag{4.2.2b}$$

$$\boldsymbol{\nabla} \cdot \mathbf{u} = -c \frac{\partial p}{\partial t}. \tag{4.2.2c}$$

the first approach performs a pure stabilization of the pressure while the others respectively resort to the modification of the mass conservation based on a more mathematical and physical point of view. These methods, namely the pressure stabilization, the penalty and the artificial compressibility are detailed in the following.

Pressure stabilization

The introduction of a second order laplacian contribution in the continuity equation (4.2.2a) constitutes a pure smoothing procedure of the pressure. This idea, originally presented by Brezzi and Pitkaranta (1984), comes directly from the observation that applying the divergence operator on the dynamic equation we get a laplacian pressure contribution, therefore our perturbation matrix R in weak form resembles the stiffness matrix, although in this case for the pressure variable,

$$R_{ij} = \epsilon \sum_K h_K^2 \int_{\Omega_K} \boldsymbol{\nabla}\Psi_i \cdot \boldsymbol{\nabla}\Psi_j \, \mathrm{d}\mathbf{x}. \tag{4.2.3}$$

The perturbation R is often made to depend on the local mesh size h_K of each element K of the domain Ω_K, the ϵ parameter is a positive user-defined constant. Its value clearly influences the accuracy of the overall scheme, as a matter of fact too large values of this parameter may lead to a non-divergence free velocity field, namely a *stable* but not *accurate* computation, on the other hand too small ϵ does not allow to effectively stabilize the equations. Many techniques have been devised to establish how large this parameter should be, even by means of considerations on local properties. Among them we just mention the use of optimal bubbles to enrich the velocity approximation inside each element of the domain, the additional degrees of freedom are eliminated before the element assembly. From an accuracy point of view we can say that the perturbation introduced is only first order accurate and therefore there is no gain in using higher order approximation, although some generalizations have also been devised. The strategy proposed by Hughes and Franca for higher accurate solutions consists in adding mesh-dependent Galerkin least-squares perturbation terms, an element by element stabilization which allows to decrease the continuity demand.

Penalty Methods

The incompressibility relaxation through the introduction of the missing pressure variable is known as penalty formulation, if we take the pressure from the (4.2.2b) and we substitute it inside the momentum equation we can directly compute the solenoidal velocity we are looking for,

$$\frac{\partial \mathbf{u}}{\partial t} + \mathbf{u} \cdot \nabla \mathbf{u} = \nu \boldsymbol{\Delta} \mathbf{u} + \nabla(\lambda \boldsymbol{\nabla} \cdot \mathbf{u}) + \mathbf{g}. \tag{4.2.4}$$

The pressure can finally be obtained from the modified continuity equation itself. The dynamic momentum equation we are now dealing with results to be 'penalised' by the amount of the infringement of the constraint itself. The penalty parameter λ is responsible for the accuracy of the scheme, the larger values give the greater accuracy but they also render the system more difficult to solve; in the limit of the infinite approach the original problem is retrieved. The penalty method can be understood as a way of solving constrained variational problems in approximated way. If we recall the Stokes problem in its variational form,

$$\mathcal{L}(\mathbf{v}, q) = \frac{1}{2}\int_\Omega (\nu \boldsymbol{\nabla}\mathbf{v} : \boldsymbol{\nabla}\mathbf{v} - \boldsymbol{g}\cdot\mathbf{v})\ \mathrm{d}\mathbf{x} - \int_\Omega q\boldsymbol{\nabla}\cdot\mathbf{v}\ \mathrm{d}\mathbf{x}$$
$$\mathcal{L}(\mathbf{u}, p) = \min_{v\in V}\max_{q\in Q}\mathcal{L}(\mathbf{v}, q).$$

with the pressure p acting as a Lagrange multiplier, in this framework the penalty approach reads

$$\widetilde{\mathcal{L}}(\mathbf{v}) = \frac{1}{2}\int_\Omega \nu\boldsymbol{\nabla}\mathbf{v} : \boldsymbol{\nabla}\mathbf{v} - \boldsymbol{g}\cdot\mathbf{v}\ \mathrm{d}\mathbf{x} + \frac{1}{2}\lambda^2\int_\Omega (\boldsymbol{\nabla}\cdot\mathbf{v})^2\ \mathrm{d}\mathbf{x},$$

equivalent to the solution of $\nu\boldsymbol{\Delta}\mathbf{u} + \boldsymbol{g} + \lambda\boldsymbol{\nabla}(\boldsymbol{\nabla}\cdot\mathbf{u}) = 0$, namely by virtue of (4.2.4) the steady Stokes equations. This formulation is characterized by an initial spurious transient, a penalty shock wave, a phase in which the pressure adjusts itself to ensure the incompressibility. This stiff behaviour prevents the use of explicit methods for the solution process, while implicit stiffly stable BDF methods make the transient disappears. The penalty method is quite attractive since easily achieves the pressure elimination, but it is not without drawbacks, even serious. First it is not known how the parameter should be chosen, furthermore the solution of the modified momentum equation is not straightforward since *e.g.* the penalty matrix $B^TQ^{-1}B$ discretizing the $\nabla(\lambda\boldsymbol{\nabla}\cdot\mathbf{u})$ term for continuous approach results to be global, (Q is a pressure mass matrix, B^T the discrete gradient operator and B the discrete divergence operator). The numerical solution is quite stiff because of the large λ parameter required, finally we remark the sacrification of the global incompressibility constraint.

Artificial Compressibility

A compressible fluid characterized by a low Mach number can be considered to be nearly incompressible, therefore the methodology tipically used for

the compressible cases can thought to be exploited for the solution of the incompressible equations themselves. The mass conservation for compressible flows reads

$$\frac{\partial \rho}{\partial t} + \boldsymbol{\nabla} \cdot (\rho \mathbf{u}) = 0 \tag{4.2.5}$$

or if manipulated by means of the linearized equation of state,

$$\frac{\partial p}{\partial t} + c_0^2 \rho_0 \boldsymbol{\nabla} \cdot \mathbf{u} = 0. \tag{4.2.6}$$

Such an equation is easily achieved starting from the solenoidality requirement just by introducing the unsteady pressure term which allows to recover the hyperbolic nature missing in the original incompressible set. This methods are most efficiently numerically attacked using implicit procedure since the artificial speed of sound seriously limit the time step to very small values. A new application of this idea has been performed by Bassi *et al.* , see [6]. The artificial compressibility term has been introduced only for the construction of the interface fluxes. The formulation is therefore always a consistent approximation of the NS equations indipendently of the amount of the artificial compressibility introduced. The evolution of the pressure and of the velocity fields seemed to have been enhanced by the stronger link established between them by the unique numerical flux function $\widehat{\mathrm{F}}$, used both for the pressure and the velocity,

$$\widehat{\mathrm{F}}\left(\mathbf{u}_h^+, p^+; \mathbf{u}_h^-, p^-\right) = \hat{\mathrm{F}}(\mathbf{u}_*, p_*)$$

with $\mathbf{u}_*$ and p_* denoting the solution of the Riemann problem.

4.2.2 Projection methods

Projection methods are a time marching technique which allows to simplify the system (4.1.1) as a series of decoupled elliptic equations for the velocity and the pressure. Two main steps can be defined, first we compute a prediction of the velocity by resorting to a pressure-guessed field, then we calculate the correction needed to achieve the right velocity by considering what has not been correctly taken into account or has been neglected previously. The theoretical background of this approach is the Helmholtz decomposition principle which states that the space $L^2(\Omega)$ can be decomposed into the direct

sum of H_{div} and $\mathcal{G}$,

$$\begin{aligned} \mathcal{G} &= \{\mathbf{w} \in [L^2(\Omega)]^d \ : \ \mathbf{w} = \nabla q \, , \ q \in H^1(\Omega)\}, \\ H_{\text{div}} &= \{\mathbf{v} \in [L^2(\Omega)]^d \ : \ \boldsymbol{\nabla} \cdot \mathbf{v} \in L^2(\Omega)\}. \end{aligned} \tag{4.2.7}$$

Therefore any vector $\mathbf{u}$ may be thought as made up of a solenoidal part and an irrotational one, $\mathbf{u} = \mathbf{v} + \mathbf{w}$. Since the divergence part is more complicated to compute the usual procedure is to find the irrotational part and by means of this to correct the guessed field $\mathbf{u}$ which is not div-free. Before introducing the main projection algorithms we present the projection applied to the Navier-Stokes equations. Nextly the description of the derived equation used for the computation of the irrotational contribution, which comes in place of the continuity constraint, partially following the approach presented by Gresho and Sani.

Navier-Stokes equations projection

The projection strategy for the NS equations can be illustrated as follows: first consider the momentum equation

$$\frac{\partial \mathbf{u}}{\partial t} + \nabla p = \nu \boldsymbol{\Delta} \mathbf{u} - \mathbf{u} \cdot \boldsymbol{\nabla} \mathbf{u} \equiv \boldsymbol{g}, \tag{4.2.8}$$

then apply it the divergence operator directly entailing the resulting expression to be zero. In this way we get $\boldsymbol{\Delta} p = \boldsymbol{\nabla} \cdot \boldsymbol{g}$ and from this one at least formally we can therefore recover the pressure as

$$\begin{aligned} p = \boldsymbol{\Delta}^{-1} \boldsymbol{\nabla} \cdot \boldsymbol{g} \Rightarrow \boldsymbol{\nabla} p &= \boldsymbol{\nabla} \boldsymbol{\Delta}^{-1} \boldsymbol{\nabla} \cdot \boldsymbol{g} \\ \frac{\partial \mathbf{u}}{\partial t} &= (I - \boldsymbol{\nabla} \boldsymbol{\Delta}^{-1} \boldsymbol{\nabla} \cdot) \boldsymbol{g}. \end{aligned} \tag{4.2.9}$$

We now introduce two operators, $\mathscr{P} = I - \boldsymbol{\nabla} \boldsymbol{\Delta}^{-1} \boldsymbol{\nabla} \cdot$ and $\mathscr{Q} = I - \mathscr{P} = \boldsymbol{\nabla} \boldsymbol{\Delta}^{-1} \boldsymbol{\nabla} \cdot$, which are orthogonal, meantime the first solenoidal and the second irrotational. These properties make the operator $\mathscr{P}$ projects onto the null space of div and $\mathscr{Q}$ onto the null space of curl. Returning to the equation (4.2.8) and exploiting the operators $\mathscr{P}$ and $\mathscr{Q}$ we can write

$$\begin{aligned} \frac{\partial \mathbf{u}}{\partial t} &= \mathscr{P} \boldsymbol{g}(\mathbf{u}) = \boldsymbol{g} - \boldsymbol{\nabla} p \\ &\Rightarrow \boldsymbol{g} = \mathscr{P} \boldsymbol{g} + \mathscr{Q} \boldsymbol{g}, \end{aligned} \tag{4.2.10}$$

which defines the orthogonal decomposition of $\boldsymbol{g}$. In practice $\mathscr{P}$ 'strip off' the gradient part of $\boldsymbol{g}$ revealing its div-free part as stated by the Helmoltz decomposition principle. The projection procedure can be summarized by the following steps:

1. Guess the pressure gradient somehow

2. Solve the momentum equation for an intermediate velocity field which is not div-free because of the non-exact pressure, for example for the Stokes case with the simple backward Euler time-stepping we have

$$\frac{\tilde{u}^{k+1} - u^k}{\Delta t} + A\tilde{u}^{k+1} + B^T p^k = f,$$

   where A and B^T are the discrete stiffness and gradient operator as defined in (4.1.10).

3. Project the intermediate velocity onto the div-free subspace resorting to an elliptic equation for the pressure,

$$BB^T(p^{k+1} - p^k) = (B\tilde{u}^{k+1} - Bu)/\Delta t$$

   remind that B is the discrete divergence operator, which in this step has been used to entail the mass conservation constraint.

4. Compute the velocity and update the pressure,

$$u^{k+1} = \tilde{u}^{k+1} - \Delta t B^T(p^{k+1} - p^k)$$

These projection methods are intended only for time accurate simulations not for quickly time marching to steady solutions via large Δt, nevertheless they also allow to achieve steady state via 'accurate' time marching.
The projection strategy has been used in many ways originating many different methods, one of the characterizing feature may perhaps be the starting point. We can hence distinguish between the schemes first performing the time discretization which allows to achieve a simpler partial differential equation and those that treat before the space approximation which deal with a system of ordinary differential equations. Before describing some of these algorithms we introduce the elliptic equation for the pressure involved by the divergence-free velocity requirement, called the pressure Poisson equation.

4.2.3 Pressure Poisson equation

The pressure Poisson equation PPE is derived from the Navier-Stokes equations to replace the incompressibility constraint. This substitution often requires the introduction of higher order derivatives and moreover it makes the right BCs quite difficult to implement.
We can simply obtain the PPE equation by a differentiation process, as the application of the divergence operator to the equation of motion. This operation has obviously to manage with existence issues, as a matter of fact it is allowed only if the initial problem is smooth enough to make the divergence of the momentum equation have sense. Clearly the new formulation of our problem does not allow to achieve all the solution the original form provides. Since there are many alternative ways to write the viscous and even the advective terms many formulations of the PPE equation are available, these forms although equivalent in the continuum they can give rise to different discrete equation and hence different algorithms. Here we limited ourselves to mention some of those most useful for some considerations.
The straightforward application of the incompressibility condition to the momentum equation gives the following PPE equation

$$\boldsymbol{\Delta} p = \nabla \cdot \left(\nu \boldsymbol{\Delta} \mathbf{u} + \boldsymbol{g} - \mathbf{u} \cdot \nabla \mathbf{u} - \frac{\partial \mathbf{u}}{\partial t} \right), \tag{4.2.11}$$

as this formulation is not easy to implement, a simplified working form can be reached just by cancelling out all the terms that vanish because of the solenoidality constraint $\boldsymbol{\nabla} \cdot \mathbf{u} = 0$, *i.e.*

$$\boldsymbol{\Delta} p = \nabla \cdot (\boldsymbol{g} - \mathbf{u} \cdot \nabla \mathbf{u}). \tag{4.2.12}$$

Unfortunately this formulation results in the ill-posedness of the scheme and in the non-uniqueness of the solution as detailed in [26], paragraph 3.10.3. As a matter of fact it is shown that this Poisson equation requires the divergence to satisfy a transient heat equation, which it is not always the case. To observe this fact we just have to subtract the (4.2.12) from the divergence of the (4.2.9),

$$\frac{\partial (\boldsymbol{\nabla} \cdot \mathbf{u})}{\partial t} = \nu \boldsymbol{\Delta} (\boldsymbol{\nabla} \cdot \mathbf{u}).$$

Therefore if the initial and boundary conditions are different than zero at the starting time then spurious solutions can be found. A better situation is

achieved retaining the 'seemingly' zero viscous term when imposing the zero divergence on the velocity field

$$\boldsymbol{\Delta} p = \nabla \cdot (\boldsymbol{g} + \nu \boldsymbol{\Delta} \mathbf{u} - \mathbf{u} \cdot \nabla \mathbf{u}). \tag{4.2.13}$$

The boundary condition for the pressure field must be such that to ensure the imposition of $\boldsymbol{\nabla} \cdot \mathbf{u} = 0$ on the boundary Γ, unfortunately not all the formulations allow to entail physical boundary conditions in agreement with this requirement. A consistent Neumann boundary conditions for the PPE is achieved for example by appling the normal to the momentum equation, *e.g.* for the second order pressure equation (4.2.13) we have

$$\frac{\partial p}{\partial n} = \boldsymbol{n} \cdot \Big(\boldsymbol{g} + \nu \boldsymbol{\Delta} \mathbf{u} - \mathbf{u} \cdot \nabla \mathbf{u} - \frac{\partial \mathbf{u}}{\partial t} \Big). \tag{4.2.14}$$

The divergence free velocity field is to be satisfied on the closure of the domain Ω at the initial time, namely the boundary Γ has to fulfill $\boldsymbol{n} \cdot \mathbf{u}_0 = \boldsymbol{n} \cdot \boldsymbol{w}_0$, (normal Dirichlet BC), being $\boldsymbol{w}_0$ the imposed velocity at $t = 0$. Normal impulsive changes in velocity would require a discontinuous normal velocity that violates the div-free requirement on the boundary.

4.2.4 Explicit Projection Methods

Explicit methods evaluate all the steady operators of an equation at the current istant time t_k, therefore their implementation results to be quite easy and directly parallelizable, they although pay for their semplicity by stability restrictions on the time step. This stability values must somehow be estimated either from theoretrical analysis or more often from euristic arguments. Usually the advancing in time of such a kind of methods is slow because only small steps are allowed, additionally the restriction on the Δt can in fact be more severe owing to accuracy issues.
One explicit strategy devised by Chan and subsequently by Gresho performs a cost reduction by updating the pressure less frequently than once per time step, therefore the expensive PPE is solved less frequently than the backward Euler would do. Their approach can be summarized by the following steps:

- Solve the advection-diffusion part using the stability restriction computed for a certain number of steps resorting to an approximated pressure gradient guessed via linear extrapolation.

- Project the computed velocity to the div-free space in order to get the 'true' velocity.

- Solve the PPE to recover the pressure.

- Define the pressure time step via local error estimates.

The major time step found in the forth step is based only on considerations that ignore the subcycling procedure.

4.2.5 Semi-implicit Projection Methods

Semi-implicit methods can be viewed as the attempt to get a good compromise between the explicit and the implicit approach, at this aim the viscous term is treated implicitly in order to avoid the stroger stability restriction related to this part of the equation, while the advective contribution is considered explicitly so to easily achieve a linearized form. This kind of methods provide a cost-effective balance between 'expensive' implicit methods and the 'unstable' explicit schemes. The principal problem with the projection methods (implicit, semi-implicit but not explicit), is the spurious boundary layer induced by the viscous component wherever the BC of Dirichlet type is specified for the tangential velocity, at worst we have an $o(\sqrt{\nu\Delta t})$ boundary for the pressure and $o(1)$ for the normal gradient of the pressure.
A semi implicit scheme presented by Gresho and Chan reads as follows

- Solve the momentum equation

$$\begin{aligned} \frac{\partial \mathbf{u}^*}{\partial t} &= \nu \boldsymbol{\Delta} \mathbf{u}^* - \mathbf{u}^* \cdot \boldsymbol{\nabla} \mathbf{u}^* + \boldsymbol{g} - \boldsymbol{\nabla} p_0 \\ \mathbf{u}^* &= \widetilde{\boldsymbol{w}} \qquad \text{on} \quad \Gamma_D, \end{aligned} \tag{4.2.15}$$

  being $\mathbf{u}^*$ the intermediate velocity field to be computed and $\widetilde{\boldsymbol{w}}$ an intermediate boundary condition to be imposed. At the outset the pressure has been somehow guessed.

- Project $\mathbf{u}^*$ to the div-free subspace at $t = T$

$$\mathbf{u}(x, T) = \mathscr{P}\mathbf{u}^*(x, T), \tag{4.2.16}$$

which corresponds to

$$\begin{aligned} \mathbf{u}^* &= \mathbf{u} + \boldsymbol{\nabla}\varphi, \quad \boldsymbol{\nabla}\cdot\mathbf{u} = 0 \quad \text{in } \Omega. \\ \boldsymbol{n}\cdot\mathbf{u} &= \boldsymbol{n}\cdot\boldsymbol{w} \quad \text{on } \Gamma_D \\ &\Rightarrow \boldsymbol{\nabla}\cdot\mathbf{u}^* = \boldsymbol{\Delta}\varphi. \end{aligned} \tag{4.2.17}$$

Comparison of equations (4.2.16) and (4.2.17) confirms that $\mathscr{P} = I - \boldsymbol{\nabla}\boldsymbol{\Delta}^{-1}\boldsymbol{\nabla}\cdot$ as stated in the relation (4.2.9), section §4.2.2.

- Finally recover $\mathbf{u}$ and p from the (4.2.17) and the PPE equation:

$$\begin{aligned} \boldsymbol{\Delta}p &= \boldsymbol{\nabla}\cdot(\boldsymbol{g} - \mathbf{u}^*\cdot\boldsymbol{\nabla}\mathbf{u}^*) \\ \partial p/\partial n &= \boldsymbol{n}\cdot(\nu\boldsymbol{\Delta}\mathbf{u} - \mathbf{u}\cdot\boldsymbol{\nabla}\mathbf{u} - \partial\boldsymbol{w}/\partial t) \quad \text{on } \Gamma_D. \end{aligned} \tag{4.2.18}$$

The optimal, *i.e.* second-order, boundary conditions, for either the intermediate velocity field and the final one, can be obtained from a Taylor series expansion. We consider the approximation for $\mathbf{u}$ and $\mathbf{u}^*$, *e.g.* $\mathbf{u}(t) = \mathbf{u}_0 + t\dot{\mathbf{u}}_0 + t^2/2\ddot{\mathbf{u}}_0 + o(t^3)$ we substitute $\dot{\mathbf{u}}_0$ and $\ddot{\mathbf{u}}_0$ with the time derivatives of the steady part of the NS equations, namely

$$\begin{aligned} \dot{\mathbf{u}}_0 = \dot{\mathbf{u}}_0^* &= \nu\boldsymbol{\Delta}\mathbf{u}^* - \mathbf{u}^*\cdot\boldsymbol{\nabla}\mathbf{u}^* + \boldsymbol{g} - \boldsymbol{\nabla}p_0 \equiv \boldsymbol{f} \\ \ddot{\mathbf{u}}_0 = \left.\frac{\partial\boldsymbol{f}(\mathbf{u})}{\partial t}\right|_{t=0}, &\qquad \ddot{\mathbf{u}}_0^* = \left.\frac{\partial\boldsymbol{f}(\mathbf{u}^*)}{\partial t}\right|_{t=0}. \end{aligned}$$

Finally after subtracting the expansions related to the two velocity field $\mathbf{u}^* - \mathbf{u} = t^2/2\boldsymbol{\nabla}p_0 + o(t^3)$, we just introduce the boundary data and we get the Dirichlet BC for $\mathbf{u}^*$,

$$\widetilde{\boldsymbol{w}} = \boldsymbol{w} + \frac{t^2}{2}\boldsymbol{\nabla}\dot{p}_0\ |_{\Gamma_D}\ . \tag{4.2.19}$$

Some more manipulations involving the above expansions applied to the Poisson equation in the (4.2.17) give the second order condition for $\boldsymbol{\varphi}$, namely

$$\varphi = \frac{T^2}{2}\dot{p}_0, \tag{4.2.20}$$

however these expressions are in fact not exploited since they require the use of $\dot{p}_0$ which is not easily computed. For this reason simpler conditions are usually adopted, $\widetilde{\boldsymbol{w}} = \boldsymbol{w}$. We point out that the projected velocity $\mathbf{u}$ does not satisfy the exact Dirichlet boundary condition as a matter of fact

$\boldsymbol{\tau} \cdot \mathbf{u} \neq \boldsymbol{\tau} \cdot \boldsymbol{w}$, with $\boldsymbol{\tau}$ defining the unit tangent vector. The slip-velocity due to this fact and the imposed Dirichlet boundary conditions, result to be responsible of a phenomenon called *vortex sheet*. To better understand the link between BC and vorticity production it can be worth to consider the scalar vorticity ω on the boundary and its flux, which are defined by

$$\omega = \frac{\partial u_\tau}{\partial n} - \frac{\partial u_n}{\partial \tau} \tag{4.2.21}$$

$$\mathscr{F} = -\nu \frac{\partial \omega}{\partial n} = -\nu \boldsymbol{\Delta} u_\tau, \tag{4.2.22}$$

with the last equality of the equation (4.2.22) obtained by exploiting the continuity constraint. Since the flux $\mathscr{F}$ is related to the tangential viscous term we can consider the tangential contribution of the momentum equation,

$$\mathscr{F} = -\nu \boldsymbol{\Delta} u_\tau = \tau \cdot \Big(\boldsymbol{f} - \frac{D\mathbf{u}}{Dt} - \boldsymbol{\nabla} p \Big) \tag{4.2.23}$$

and subsequently we integrate it in time:

$$\begin{aligned} \int_0^T \mathscr{F} \mathrm{dt} &= \underbrace{\int_0^T \Big(\boldsymbol{f} - \frac{D\mathbf{u}}{Dt} \Big) \mathrm{dt}}_{g} - \int_0^T \frac{\partial p}{\partial \tau} \mathrm{dt} \\ &= g - \int_0^T \Big(\frac{\partial p_0}{\partial \tau} + t \frac{\partial \dot{p}_0}{\partial \tau} + \frac{t^2}{2} \frac{\partial^2 \ddot{p}_0}{\partial \tau^2} + ... \Big) \mathrm{dt} \\ &= g - \Big(T \frac{\partial p_0}{\partial \tau} + \frac{T^2}{2} \frac{\partial \dot{p}_0}{\partial \tau} + \frac{T^3}{6} \frac{\partial^2 \ddot{p}_0}{\partial \tau^2} + ... \Big). \end{aligned} \tag{4.2.24}$$

This last equation shows how imposing more accurate boundary conditions such as the (4.2.19) allows to increase the accuracy of vorticity injection.
As final remark, these methods are intended only for 'time accurate' simulations not for quickly time-marching to steady-state solutions.

4.2.6 Pressure correction schemes

The class of projection methods contemplates the so called pressure correction schemes, which still perform the splitted computation of the velocity and the pressure fields. The algorithm consists of two steps, in its simplest form the first one solves the viscous and the advective parts of the momentum equation while the second considers the divergence-free velocity constraint.

In the following equations the non-incremental version of the pressure correction method is presented,

$$\begin{aligned} \frac{1}{\Delta t}(\tilde{\mathbf{u}}^{k+1}-\mathbf{u}^{k})-\nu\boldsymbol{\Delta}\tilde{\mathbf{u}}^{k+1}+\mathbf{u}^{*}\cdot\nabla\tilde{\mathbf{u}}^{k+1}&=\mathbf{g}^{k+1}, \\ \tilde{\mathbf{u}}^{k+1}\mid_{\Gamma}&=\mathbf{0}, \end{aligned} \tag{4.2.25a}$$

$$\left\{ \begin{array}{ll} \frac{1}{\Delta t}(\mathbf{u}^{k+1}-\tilde{\mathbf{u}}^{k+1})+\nabla p^{k+1}=\mathbf{0} & \\ \nabla\cdot\mathbf{u}^{k+1}=0, & \mathbf{u}^{k+1}\cdot n\mid_{\Gamma}=0 \end{array} \right\}, \tag{4.2.25b}$$

where $\tilde{\mathbf{u}}$ is the predicted velocity and $\mathbf{u}^{*}$ the value related to the discretization of the advective part. As it can be observed the first substep (4.2.25a) accounts for the viscous and the advective components, while the equation (4.2.25b) enforces incompressibility. In [27] accuracy results are shown, in particular this scheme gives a first order for the velocity, (measured in the $\mathbf{H}^{1}(\Omega)$ norm) and only of one half for the pressure, (in the $\mathbf{L}^{2}(\Omega)$ norm). This sub-optimal performance is due to the spurious unphysical boundary condition that the equation (4.2.25b) involves, namely $\nabla p^{k+1}\mid_{\Gamma}=0$.
The pressure and velocity fields may better interplay one another just by not neglecting ∇p^{k} in the equation (4.2.25a), therefore the improved scheme which exploits a BDF2 scheme (4.1.22) for the time discretization reads

$$\begin{aligned} \frac{1}{2\Delta t}(3\tilde{\mathbf{u}}^{k+1}-4\mathbf{u}^{k}+\mathbf{u}^{k-1})-\nu\boldsymbol{\Delta}\tilde{\mathbf{u}}^{k+1}+\mathbf{u}^{*}\cdot\nabla\tilde{\mathbf{u}}^{k+1}+\nabla p^{k}&=\mathbf{g}^{k+1}, \\ \tilde{\mathbf{u}}^{k+1}\mid_{\Gamma}&=\mathbf{0}, \end{aligned} \tag{4.2.26a}$$

$$\left\{ \begin{array}{ll} \frac{1}{2\Delta t}(3\mathbf{u}^{k+1}-3\tilde{\mathbf{u}}^{k+1})+\nabla(p^{k+1}-p^{k})=\mathbf{0} & \\ \nabla\cdot\mathbf{u}^{k+1}=0, & \mathbf{u}^{k+1}\cdot\boldsymbol{n}\mid_{\Gamma}=0 \end{array} \right\}, \tag{4.2.26b}$$

this scheme is known as incremental pressure correction method. Convergence results exhibit a second order accuracy for the velocity in the $\mathbf{H}^{1}(\Omega)$ norm and only of order one for the pressure in the $\mathbf{L}^{2}(\Omega)$ norm. This is still a symptom of the numerical boundary layer induced by the spurious boundary conditions associated even with this scheme,

$$\nabla p^{k+1}\cdot\mathbf{n}\mid_{\Gamma}=\nabla p^{k}\cdot\mathbf{n}\mid_{\Gamma}.$$

A cure was proposed in the rotational incremental pressure correction scheme, the idea is to enforce the continuity constraint thoroughly the scheme,

$$\begin{aligned} \frac{1}{2\Delta t}(3\tilde{\mathbf{u}}^{k+1}-4\mathbf{u}^{k}+\mathbf{u}^{k-1})-\nu\boldsymbol{\Delta}\tilde{\mathbf{u}}^{k+1}+\mathbf{u}^{*}\cdot\nabla\tilde{\mathbf{u}}^{k+1}+\nabla p^{k}&=\mathbf{g}^{k+1} \\ \tilde{\mathbf{u}}^{k+1}\mid_{\Gamma}&=\mathbf{0} \end{aligned} \tag{4.2.27a}$$

$$\left\{ \begin{array}{l} \frac{1}{2\Delta t}(3\mathbf{u}^{k+1} - 3\tilde{\mathbf{u}}^{k+1}) + \nabla\phi^{k+1} = 0 \\ \nabla \cdot \mathbf{u}^{k+1} = 0, \quad \mathbf{u}^{k+1} \cdot \mathbf{n} \mid_{\Gamma} = 0 \\ \phi^{k+1} = p^{k+1} - p^{k} + \nu\nabla \cdot \tilde{\mathbf{u}}^{k+1} \end{array} \right\}, \tag{4.2.27b}$$

this formulation considers the viscous term in rotational form *i.e.* it resorts to the identity $\boldsymbol{\Delta}\mathbf{u} \equiv \nabla(\nabla\cdot\mathbf{u}) - \nabla\times\nabla\times\mathbf{u}$. To better understand this approach it can be useful to look at the momentum equation that the rotational scheme in fact solves,

$$\frac{1}{2\Delta t}(3\mathbf{u}^{k+1} - 4\mathbf{u}^{k} + \mathbf{u}^{k-1}) - \nu\nabla\times\nabla\times\mathbf{u}^{k+1} + \mathbf{u}^{*}\cdot\nabla\mathbf{u}^{k+1} + \nabla p^{k} = \mathbf{g}^{k+1}, \tag{4.2.28}$$

as it can be seen just by recomposing the substeps (4.2.27a)-(4.2.27b) to retrieve the full statement of momentum conservation. The foundamental aspect is that the (4.2.28) displays no spurious boundary layers, since now the Neumann BC is

$$\left.\frac{\partial p}{\partial n}\right|_{\Gamma}^{k+1} = (\mathbf{g}^{k+1} - \nu\nabla\times\nabla\times\mathbf{u}^{k+1}) \cdot n \mid_{\Gamma} . \tag{4.2.29}$$

This pressure boundary condition results to be consistent and stable and even more reliable than the exact BC,

$$\frac{\partial p_e}{\partial n} = \boldsymbol{n} \cdot \nu\boldsymbol{\Delta}\mathbf{u},$$

which is obtained from the momentum equation projected in the normal direction. As a matter of fact the rotational form (4.2.29) allows to better control the boundary divergence flux directly by means of the time step. Hence it prevents its accumulation during the integration, which may cause instability phenomena. This behaviour can be appreciated by considering the exact boundary condition and using the Taylor expansion of the curl of the vorticity,

$$\frac{\partial p_e^{k+1}}{\partial n} = \nu\Big(\frac{\partial \mathcal{D}^{k+1}\mathbf{u}}{\partial n} - \omega_s^{k+1}\Big) \Rightarrow \frac{\partial \mathcal{D}^{k+1}\mathbf{u}}{\partial n} = \frac{1}{\nu}\frac{\partial p_e^{k+1}}{\partial n} + \omega_s^{k} + \Delta t\frac{\partial \omega_s^{k}}{\partial t} + ..$$

with $\mathcal{D}\mathbf{u} = \boldsymbol{\nabla}\cdot\mathbf{u}$ and $\omega_s = \boldsymbol{\nabla}\times\omega\cdot\boldsymbol{n}$. If we use the laplacian form of the Neumann condition the above equation becomes

$$\frac{\partial \mathcal{D}^{k+1}\mathbf{u}}{\partial n} \propto \frac{\partial \mathcal{D}^{k}\mathbf{u}}{\partial n} + \Delta t\frac{\partial \omega_s^{k}}{\partial t}$$

which shows the increase of divergence flux in time, if instead we consider the form (4.2.29) we get a direct control on the divergence through each time step,

$$\frac{\partial \mathcal{D}^{k+1}\mathbf{u}}{\partial n} \propto \Delta t \frac{\partial \omega_s^k}{\partial t}.$$

Although the enhancement got by the use of the correct boundary condition, the rate of convergence of the rotational scheme is not optimal yet, the convergence of the pressure numerically results half order less than what one should expect and it has also been proven analitically. It remains that the tangential part of the velocity is not correctly imposed, Guermond shows that the optimal order is got back when you are using smooth, *i.e.* circular domains.
In conclusion the dual splitting strategy of the above scheme is presented, it is enough to reverse the pressure role with that of the velocity within the predictor-corrector steps. First the momentum equation for the pressure with the viscous component, which has but guessed, is solved

$$\begin{aligned} &\frac{1}{2\Delta t}(3\tilde{\mathbf{u}} - 4\mathbf{u}^k + \mathbf{u}^{k-1}) - \nu\nabla \times \nabla \times \mathbf{u}^k + \mathbf{u}^* \cdot \nabla \tilde{\mathbf{u}}^{k+1} + \nabla p^{k+1} = \mathbf{g}^{k+1} \\ &\boldsymbol{\nabla}\tilde{\mathbf{u}} = 0, \qquad \tilde{\mathbf{u}} \cdot \boldsymbol{n} = 0 \quad \text{on } \partial\Omega \end{aligned} \tag{4.2.30}$$

then a velocity correction is computed

$$\begin{aligned} \frac{3\mathbf{u}^{k+1} - 3\tilde{\mathbf{u}}}{2\Delta t} &= \nu\boldsymbol{\Delta}\mathbf{u}^{k+1} + \nu\nabla \times \nabla \times \mathbf{u}^k \\ \mathbf{u}^{k+1} &= 0 \quad \text{on } \partial\Omega. \end{aligned} \tag{4.2.31}$$

The div-curl form of the viscous term has been used in accordance with the achievement of physical boundary conditions for the pressure, the overall behaviour is exactly the same of the above described pressure correction scheme.
A consistent splitting scheme fully second order is also been proposed by Guermond and Shen starting from the ideas provided by the pressure-correction scheme. They compute the pressure as the Galerkin projection of the momentum equation tested against the gradient of a function belonging to $\mathbf{H}^1(\Omega)$,

$$\int_\Omega \boldsymbol{\nabla} q \cdot \boldsymbol{\nabla} p \, \mathrm{d}\mathbf{x} = \int_\Omega \boldsymbol{\nabla} q \cdot (\mathbf{g} + \mathbf{u} \cdot \boldsymbol{\nabla}\mathbf{u} + \nu\boldsymbol{\Delta}\mathbf{u}) \, \mathrm{d}\mathbf{x}, \quad \forall q \in \mathbf{H}^1(\Omega) \tag{4.2.32}$$

therefore the overall scheme is given by the following steps,

$$\begin{aligned} \frac{1}{2\Delta t}(3\mathbf{u}^{k+1} - 4\mathbf{u}^{k} + \mathbf{u}^{k-1}) - \nu\boldsymbol{\Delta}\mathbf{u}^{k+1} + \mathbf{u}^{*}\cdot\nabla\mathbf{u}^{k+1} + \nabla\bar{p}^{k} = \mathbf{f}^{k+1}, \\ \mathbf{u}^{k+1}\mid_{\Gamma} = \mathbf{0}, \qquad \text{on } \partial\Omega, \end{aligned} \tag{4.2.33}$$

$$\begin{aligned} (\boldsymbol{\nabla} q, \boldsymbol{\nabla}\psi) = \Big(\boldsymbol{\nabla} q, \frac{3\mathbf{u}^{k+1} - 4\mathbf{u}^{k} + \mathbf{u}^{n-1}}{2\Delta t}\Big), \quad \forall q \in \mathbf{H}^{1}(\Omega), \\ p^{k+1} = \psi^{k+1} + \bar{p}^{k} - \nu\boldsymbol{\nabla}\cdot\mathbf{u}^{k+1}, \end{aligned} \tag{4.2.34}$$

with $\bar{p} = 2p^{k} - p^{k-1}$ defining an extrapolation of order two of the pressure, the rotational form have clearly been exploited.

4.2.7 Fractional step methods

Another class of methods that adressed the splitting of the unknwon pressure and velocity fields, is known as fractional step. These schemes still compute the solution of the incompressible NS equations by considering the viscous part and the incompressible constraint separately, in order to handle in each step just one feature. An elliptic advection-diffusion problem first and an inviscid problem afterwards for the pressure variable.
Guermond and Quartapelle introduced in 1997, (see [29]), a stable incremental fractional step method in which a semi-implicit approximation of the non-linear part of the NS equations is used to avoid any time-step restiction. Their alghoritm reads

$$\begin{aligned} \Big(\frac{\mathbf{u}_h^{k+1} - \mathbf{u}_h^{k}}{\delta t}, \boldsymbol{v}_h\Big) + a(\mathbf{u}_h^{k+1}, \boldsymbol{v}_h) + b(\mathbf{u}_h^{k}, \mathbf{u}_h^{k+1}, \boldsymbol{v}_h) = (\boldsymbol{g}^{k+1}, \boldsymbol{v}_h) - (\nabla\bar{p}_h, \boldsymbol{v}_h) \\ (\nabla(p_h^{k+1} - p_h^{k}), \nabla q_h) = -\frac{(\nabla\cdot\mathbf{u}_h^{k+1}, q_h)}{\delta t}, \end{aligned} \tag{4.2.35}$$

the bilinear form $a(\cdot,\cdot)$ defines the viscous contribution while the trilinear form $b(\cdot,\cdot,\cdot)$ is related to the inertial part. This scheme yields a first order accuracy in time in the natural norm.
An explicit fractional-step matrix-free approach is presented in [39] where the combination of a classical fractional-step scheme along with an artificial compressibility strategy is exploited, a second order convergence for an

oscillation free pressure is achieved. The first step consists in solving the momentum equation without taking care of the pressure term and by performing a Taylor expansion of the steady part of the equation,

$$\mathbf{u}^* - \mathbf{u}^k = \Delta t(-\mathbf{u}\cdot\boldsymbol{\nabla}\mathbf{u} + \nu\boldsymbol{\Delta}\mathbf{u})^k + \frac{\Delta t^2}{2}\mathbf{u}\cdot\boldsymbol{\nabla}(\mathbf{u}\cdot\boldsymbol{\nabla}\mathbf{u} + \boldsymbol{\nabla}P + \nu\boldsymbol{\Delta}\mathbf{u})^k, \quad (4.2.36)$$

with the second order term acting as a stabilization. The subsequent step amounts to the computation of the pressure:

$$\left(\frac{1}{\beta^2}\right)^k (p^{k+1} - p^k) = -\Delta t(\boldsymbol{\nabla}\cdot\mathbf{u}^k + \theta_1\boldsymbol{\nabla}\cdot\mathbf{u}^* - \Delta t\theta_1(\boldsymbol{\Delta}p^k)), \quad (4.2.37)$$

the parameter θ_1 is the positive factor needed to enhance the pressure stability while the β is the finite artificial compressible wave speed replacing the true velocity c in the compressible mass conservation $\frac{1}{c^2}\frac{\partial p}{\partial t} = \nabla\cdot\mathbf{u}$. Its value has a crucial role in the overall stability of the scheme and it is computed by considering the advective and diffusive velocity of the flow itself. The local time step of the simulation is got as $\Delta t = h/(|\mathbf{u}_{\text{conv}}| + \beta)$ multiplied by a safety factor. Finally the intermediate velocity $\mathbf{u}^*$ is corrected by accounting for the interplay with the pressure field

$$\mathbf{u}^{k+1} = \mathbf{u}^* - \Delta t\boldsymbol{\nabla}p^k. \quad (4.2.38)$$

The second order accuracy is achieved by replacing $\boldsymbol{\nabla}p^k$ in the third step (4.2.38) with $\boldsymbol{\nabla}(p^{k+1} - p^k)$ and implementing a *dual time stepping* procedure as follows

$$\begin{aligned} \mathbf{u}^{k+1} &= \mathbf{u}^* - \Delta t\boldsymbol{\nabla}(p^k - p^m) - \Delta t\frac{\Delta\mathbf{u}_R}{\Delta\tau} \\ \Delta\mathbf{u}_R &= \frac{3\mathbf{u}^k - 4\mathbf{u}^m + \mathbf{u}^{m-1}}{2} \end{aligned} \quad (4.2.39)$$

where $\Delta\mathbf{u}_R$ defines the real time variation of $\mathbf{u}$ which is second order in time, m is the real time label and k the local iteration within each real time step in implicit approach.

4.2.8 Algebraic operator splitting

The splitting strategy can be applied either to the differential form directly or to the algebraic system obtained after performing some kind of space-time

discretization, both strategies give rise to schemes that can be traced back to the framework of projection methods. In this paragraph the algebraic point of view is presented, for this purpose we consider the linear system $A\boldsymbol{x}^{k+1} = \boldsymbol{b}^{k+1}$ associated to the discretized NS equations in space and in time, which reads

$$\begin{bmatrix} C & D^T \\ D & 0 \end{bmatrix} \begin{bmatrix} \mathbf{u}^{k+1} \\ p^{k+1} \end{bmatrix} = \begin{bmatrix} \mathbf{f}^{k+1} \\ \mathbf{g}^{k+1} \end{bmatrix}. \tag{4.2.40}$$

The matrices read $C = \frac{1}{\Delta t}M + S$, $S = K + B(\mathbf{u}^k)$, $\mathbf{f} = \boldsymbol{F}^{k+1} + \frac{1}{\Delta t}M\mathbf{u}^k$ and $\mathbf{g}^{k+1} = \mathbf{0}$, D^T defines the discrete gradient operator and D the adjoint operator of D^T, $M = (\varphi_i, \varphi_j)$ is the mass matrix and $K = [a(\varphi_i, \varphi_j)]$ the stiffness matrix. The solution field $(\mathbf{u} - p)$ can formally be retrieved as

$$\begin{aligned} \mathbf{u}^{k+1} &= C^{-1}(\mathbf{f}^{k+1} - D^T p^{k+1}) \\ DC^{-1}D^T p^{k+1} &= DC^{-1}\mathbf{f}^{k+1} - \mathbf{g}^{k+1}, \end{aligned} \tag{4.2.41}$$

actually two quite expensive steps. The pursued improving strategy is that of performing a splitted computation by means of an approximated lower-upper factorization, in this presentation the Yosida method has been considered, see [42]. The original system (4.2.40) is therefore numerically adressed by the LU rewriting of the matrix A which directly stems in the decoupling of the variables we are looking for,

$$\begin{bmatrix} C & D^T \\ D & 0 \end{bmatrix} = \begin{bmatrix} C & 0 \\ D & -DC^{-1}D^T \end{bmatrix} \begin{bmatrix} I & C^{-1}D^T \\ 0 & I \end{bmatrix}. \tag{4.2.42}$$

In detail we have:

$$\begin{aligned} C\mathbf{u}^{*,k+1} &= \mathbf{f}^{k+1} \\ -DC^{-1}D^T p^{k+1} &= \mathbf{g}^{k+1} - D\mathbf{u}^{*,n+1} \\ C\mathbf{u}^{k+1} &= C\mathbf{u}^{*,k+1} - D^T p^{k+1}, \end{aligned} \tag{4.2.43}$$

the first step allows to compute the intermediate not constrained velocity field $\mathbf{u}^*$, the second step corresponds to the discrete laplacian equation entailing the incompressibility and finally the third step perfoms the correction on the velocity field $\mathbf{u}^*$ due to the pressure field in order to ensure $\boldsymbol{\nabla} \cdot \mathbf{u} = 0$.
Inexact factorizations suitably approximate C^{-1} in order to get better performances, different choices are available, for the sake of their presentation

C^{-1} is substituted by H_1 in the lower triangular matrix of the factorization and by H_2 in the upper one making the original matrix be as

$$\begin{bmatrix} C & CH_2D^T \\ D & D(H_2 - H_1)D^T \end{bmatrix}. \tag{4.2.44}$$

In the case the two matrices are coincident $H_1 = H_2 \neq C^{-1}$, we have a mass preserving scheme, while if they differ from one another we are dealing with a quasi-compressibility method. The Yosida method takes $H_1 = \Delta t M^{-1}$ and $H_2 = C^{-1}$ mantaining unchanged the momentum equation, the approximation matrix H_1 is the first order truncation of the Neumann expansion of C^{-1} itself. In [42] an extensive analysis has been led on the well-posedness and on the stability along with a thoroughly study of the splitting error, enforced by numerical results.
The improvement of the scheme has been achieved by means of a pressure correction strategy similarly to that introduced in §4.2.6, where the equation (4.2.27b) provides the end of step pressure $p_{\text{end}}^{k+1} = p^{k+1} - \nu \boldsymbol{\nabla} \cdot \mathbf{u}^{*,n+1}$. The modified matrix factorization that accomplished such an aim reads

$$\begin{bmatrix} C & 0 \\ D & -DH_1D^T \end{bmatrix} \begin{bmatrix} I & H_2D^TR \\ 0 & Q \end{bmatrix}, \tag{4.2.45}$$

where the matrix Q defines the pressure correction and the R establishes the link between the pressure and the final velocity. High-order accuracy is pursued through the requirement of null error splitting, the expression of this matrix can be found in [21]. In this paper the spectral discretization is joined with an higher order LU approximation of the matrix A, the Yosida4 method together with a forth order discretization in time produce a solution with an accuracy of $(\Delta t)^4$ for the velocity in the discrete L^2-norm and of $(\Delta t)^{7/2}$ for the pressure. A complete theoretical analysis and numerical assessment establish the accuracy, a forth order in time has been achieved.

4.3 New Semi-implicit DG method

The goal of this chapter is to present our new algorithm for the numerical solution of the incompressible NS equations. In the previous sections we described some existing strategies facing the Navier-Stokes problem, at the aim to introduce the main ideas that have been exploited for its solution. After this we first of all outline the key points that we tried to keep fix during

the definition process of the scheme, these concepts are of main importance for the right physical and mathematical understanding of the flow behaviour. In particular we remind that the pressure surely plays a central role as its value allows to keep the flow div−free everywhere for each instant by adjusting itself istantaneously in time. This fact is tightly linked to the div-grad coupling between the velocity and the pressure itself, as a thoroughly mathematical study of the system can show. This variable must clearly be treated implicitly to make its change possible in time, overcoming the original lack for hyperbolicity with respect to its contribution. Owing to the $(\mathbf{u} - p)$ relationship we also have to adopt the same kind of time treatment for the continuity equation. As regards the solution strategies they can all be recast to either coupled or splitted approach, refering to the differential or to the algebraic point of view. Summarizing we can define the splitting methods as a decomposition of the problem into simpler parts, easier to consider, in this framework the projection, the pressure correction and the fractional step methods may be accomodated. This way of proceeding involves the definition of an equation for the pressure which often necessitates of unphysical pressure BCs. Instead relaxing the continuity equation allows to modify the system structure and hence to compute the overall solution field directly, such a procedure presents however the critical managing of the perturbation term.
In our solution strategy the interplay between the pressure and the velocity has been modeled by means of the changes of the field towards convergence carried on by the natural evolution involved by the discontinuous scheme itself. The discretization of the problem has been done trying to entail the minimum level of implicitness necessary to achieve the solvability of the algebraic system. Such an approach performs therefore a semi-implicit treatment of the INS, in which the exlicit contribution acts almost as 'forcing' part for the implicit one. The meaning of this statement will be better explained in the following. The additive Runge-Kutta method introduced in [50] has been used to suitably evaluate the different contributions of the system.

4.3.1 The algorithm

We moved from the idea that if we were able to solve the original scheme directly someway, without resorting to any trick, as mixed interpolation or staggered grids, or to stabilization techniques, we should compute a pressure field p^{k+1} at the istant t^{k+1} such that the associated velocity field is solenoidal.

The simplest semi-discrete scheme resuming this concept and that set our starting point up, reads as follows

$$\begin{aligned} \frac{\partial \mathbf{u}}{\partial t} + \mathbf{u}^k \cdot \nabla \mathbf{u}^k - \nu \boldsymbol{\Delta} \mathbf{u}^k + \nabla p^{k+1} &= \mathbf{0} \\ \nabla \cdot \mathbf{u}^{k+1} &= 0, \end{aligned} \tag{4.3.1}$$

where as usual the superscript k defines the current istant time t^k and the k+1 the next time $t^{k+1} \equiv t^k + \Delta t$. The temporal accuracy issue requires the use of a scheme that well addresses both the implicit and the explicit dynamic. This goal has been achieved by means of an additive semi-implicit Runge-Kutta method, in particular we refer to the *ASIRK* schemes presented in [50], this approach seemed the one that better could suit our algorithm. Consider the first-order ordinary differential equations involved by some spatial discretization procedure given by

$$\frac{\mathrm{d}\mathbf{u}}{\mathrm{d}t} = \boldsymbol{f}(\mathbf{u}) + \boldsymbol{g}(\mathbf{u}), \tag{4.3.2}$$

where $\mathbf{u}$ is the vector of discretized flow field variables. The right hand side has been somehow additively splitted into two parts, $\boldsymbol{f}$ and $\boldsymbol{g}$, the former explicitly evaluated and the latter implicitly. A general r-stage additive semi-implicit Runge-Kutta methods integrates the system (4.3.2) as

$$\begin{aligned} \mathbf{u}^{n+1} &= \mathbf{u}^n + \sum_{j=1}^{r} w_j \boldsymbol{k}_j \\ \boldsymbol{k}_i &= h\Big\{ \boldsymbol{f}\Big(\mathbf{u}^n + \sum_{j=1}^{i-1} b_{ij}\boldsymbol{k}_j\Big) + \boldsymbol{g}\Big(\mathbf{u}^n + \sum_{j=1}^{i-1} c_{ij}\boldsymbol{k}_j + a_i \boldsymbol{k}_i\Big)\Big\}, \end{aligned} \tag{4.3.3}$$

for $i = 1, .., r$, with $h = \Delta t$ the time step size and a_i, b_{ij}, c_{ij}, w_j the RK parameters determined by Zhong through stability and accuracy requirements. A more computationally efficient semi-implicit RK scheme is provided by the semi-implicit extension of the Rosenbrock RK method, which avoids the expensive use of the nonlinear solver required by the implicit approach for the nonlinear part $\boldsymbol{g}$,

$$\Big[\boldsymbol{I} - h a_i \boldsymbol{J}\Big(\mathbf{u}^n + \sum_{j=1}^{i-1} d_{ij}\boldsymbol{k}_j\Big)\Big]\boldsymbol{k}_i = h\Big\{\boldsymbol{f}\Big(\mathbf{u}^n + \sum_{j=1}^{i-1} b_{ij}\boldsymbol{k}_j\Big) + \boldsymbol{g}\Big(\mathbf{u}^n + \sum_{j=1}^{i-1} c_{ij}\boldsymbol{k}_j\Big)\Big\} \tag{4.3.4}$$

for $i = 1, .., r$, with $\boldsymbol{J}$ the Jacobian matrix of the term $\boldsymbol{g}$. Most of the Rosenbrock methods use $a_i = a$ and $d_{ij} = 0$, we implemented the so called $ASIRK - 3B$ scheme.
We first consider the dynamic equation to define its 'implicitness' level, in particular we separately account for the inertial and viscous contribution and for the pressure term as

$$\int_K \varphi \frac{\partial \mathbf{u}}{\partial t} \, \mathrm{d}\mathbf{x} + \int_K \varphi \cdot \boldsymbol{\nabla} p \, \mathrm{d}\mathbf{x} + \mathcal{R}_u = 0, \tag{4.3.5}$$

being $\mathcal{R}_u$ the former part. We then integrate by parts elementwise the pressure contribution,

$$\int_K \varphi \cdot \boldsymbol{\nabla} p \, \mathrm{d}\mathbf{x} = \int_{\partial K} \varphi \, \widehat{p} \cdot \boldsymbol{n} \, \mathrm{d}\sigma - \int_K p \boldsymbol{\nabla} \varphi \, \mathrm{d}\mathbf{x}, \tag{4.3.6}$$

which by virtue of a counter-integration also reads

$$\int_{\partial K} \varphi (\widehat{p} - p) \boldsymbol{n} \, \mathrm{d}\sigma + \int_K \varphi \boldsymbol{\nabla} p \, \mathrm{d}\mathbf{x}. \tag{4.3.7}$$

The pressure volume integral is the only part we advise numerically to necessarily evaluate in implicit form. By virtue of the discretization performed till now we can propose the INS system in the following formulation,

$$\begin{aligned} \mathscr{G}_p &= 0, \\ \int_K \varphi \, \frac{\partial u}{\partial t} \, \mathrm{d}\mathbf{x} + \mathscr{G}_u + \mathscr{R}_u &= 0, \\ \int_K \varphi \, \frac{\partial v}{\partial t} \, \mathrm{d}\mathbf{x} + \mathscr{G}_v + \mathscr{R}_v &= 0. \end{aligned} \tag{4.3.8}$$

The $\mathscr{G}$ terms are those to be implicitly treated, while the $\mathscr{R}$ explicitly, respectively in the first equation of the system which is clearly the continuity constraint and in the momentum conservation, the implicit part of the latter has been just defined, *i.e.*

$$\mathscr{G}_u = \int_K \varphi \frac{\partial p}{\partial x}\Big|_{\mathrm{int}} \, \mathrm{d}\mathbf{x}, \qquad \mathscr{G}_v = \int_K \varphi \frac{\partial p}{\partial y}\Big|_{\mathrm{int}} \, \mathrm{d}\mathbf{x}. \tag{4.3.9}$$

The next step is the definition of the overall ingredients necessary to achieve the discrete continuity equation, that as said is naturally implicitly considered. In order to establish the necessary link with the momentum equation

we first apply the Rosenbrock approach to the constraint itself as follows

$$\mathscr{G}(\mathbf{u}^{k+1}, p^{k+1}) \sim \mathscr{G}(\mathbf{u}^{k}) + \frac{\partial \mathscr{G}}{\partial \mathbf{u}^{\pm}} \Delta \mathbf{u}^{\pm} + \frac{\partial \mathscr{G}}{\partial p^{\pm}} \Delta p^{\pm}. \tag{4.3.10}$$

Such a procedure represents the mean to couple in the sense of minimum 'implicitness' level the pressure and the velocity field, as a matter of fact it allows to outline how the different parts have to be accounted for. At this purpose we turn to the weak integral form of the continuity,

$$\int_{\partial K} \varphi \, \widehat{\mathbf{u}}_n^{k+1}(p^{\pm}, \mathbf{u}^{\pm}) \, \mathrm{d}\sigma - \int_K \mathbf{u}^{k+1} \cdot \boldsymbol{\nabla} \varphi \, \mathrm{d}\mathbf{x} = 0, \tag{4.3.11}$$

where as usual the $\widehat{\mathbf{u}}_n$ stands for the normal numerical flux vector responsible of the discontinuity handling in the DG discrete approach. The boundary integral is then treated by means of the Rosenbrock method $\widehat{\mathbf{u}}_n^{k+1} = \widehat{\mathbf{u}}_n^{k} + J$, with J the Jacobian of the numerical flux vector, which enables the discontinuity to introduce the necessary variations that make the evolution of the whole field be possible,

$$\widehat{\mathbf{u}}_n^{k+1} = \widehat{\mathbf{u}}_n^{k} + \frac{\partial \widehat{\mathbf{u}}_n}{\partial p^{\pm}} \Delta p^{\pm} + \frac{\partial \widehat{\mathbf{u}}_n}{\partial \mathbf{u}^{\pm}} \Delta \mathbf{u}^{\pm}, \tag{4.3.12}$$

similarly for the volume integral.
Further understanding of the algorithm may perhaps be provided by considering the algebraic point of view, at this aim we look for the definition of the components of the algebraic final system $A\mathbf{u} = \boldsymbol{b}$. Therefore in more detail we first focus on the dynamic equation for the $x-$contribution

$$\mathbf{M} \frac{\Delta U}{\Delta t} + R_u + \mathbf{M}_x \Delta P = 0, \tag{4.3.13}$$

being R_u the residual of the momentum equation along the $x-$axis for the explicit contribution, with $\mathbf{M}$ defining the usual mass matrix and $\mathbf{M}_x$ the matrix associated to the discretization of the internal pressure gradient contribution,

$$\mathscr{G}_u = \int_K \varphi \frac{\partial p}{\partial x}\Big|_{\text{int}} \, \mathrm{d}\mathbf{x} \rightarrow \mathbf{M}_{ij,x} = (\varphi_i, \varphi_{j,x}).$$

We point out that (U, V, P) represent the degrees of freedom of the problem, the coefficient of the polynomial expansion to be computed as to achieve the

required solution. The discrete continuity equation is obtained by the *ad-hoc* inclusion of variations of the velocity and pressure fields coming from the momentum itself, in particular we begin by introducing the matrix associated to the continuity inside this framework,

$$\begin{bmatrix} A & B & C \\ M_x & M & 0 \\ M_y & 0 & M \end{bmatrix} \begin{pmatrix} \Delta P \\ \Delta U \\ \Delta V \end{pmatrix} = \begin{pmatrix} R_p \\ R_u \\ R_v, \end{pmatrix} \tag{4.3.14}$$

being R_p the residual of the continuity, its components are given by

$$\begin{aligned} A_{ij} &= \int_{\partial k} \varphi_i \frac{\partial \widehat{\mathbf{u}}_n}{\partial p^{\pm}} \varphi_j^{\pm} \, \mathrm{d}\sigma \\ B_{ij} &= \int_{\partial k} \varphi_i \frac{\partial \widehat{\mathbf{u}}_n}{\partial u^{\pm}} \varphi_j^{\pm} \, \mathrm{d}\sigma - \int_K \varphi_{i,x} \cdot \varphi_j \, \mathrm{d}\mathbf{x} \\ C_{ij} &= \int_{\partial k} \varphi_i \frac{\partial \widehat{\mathbf{u}}_n}{\partial v^{\pm}} \varphi_j^{\pm} \, \mathrm{d}\sigma - \int_K \varphi_{i,y} \cdot \varphi_j \, \mathrm{d}\mathbf{x}. \end{aligned} \tag{4.3.15}$$

The variations $\Delta u^{\pm}$ and $\Delta v^{\pm}$ as well as $\Delta \mathbf{u}$ in (4.3.11) to be inserted into the (4.3.14) can be thought as the summation of two contribution, one deriving from the pressure evolution while the other from the velocity field, which are being mutually interchanging information. As regards this matter we have

$$\begin{aligned} \frac{\Delta \mathbf{u}}{\Delta t} &= M^{-1}\big(R_u + M_x \Delta P\big), \\ \frac{\partial \widehat{\mathbf{u}}_n}{\partial u^{\pm}} \Delta u^{\pm} &= \frac{\partial \widehat{\mathbf{u}}_n}{\partial u^{\pm}} \big(M^{-1} R_u \Delta t + M^{-1} M_x \Delta P \Delta t\big), \end{aligned} \tag{4.3.16}$$

the latter part is the internal implicit pressure given by the (4.3.9). The discrete continuity system is then provided as said by accounting for the contributions of the momentum, in view of this the system to be solved reduces to the following

$$\begin{bmatrix} A & B & C \end{bmatrix} \begin{pmatrix} \Delta P \\ \Delta U \\ \Delta V \end{pmatrix} = \begin{pmatrix} R_p \\ R_u \\ R_v \end{pmatrix}. \tag{4.3.17}$$

Accordingly equation (4.3.17) is equivalent to the following resolution equation

$$\Big(A + B M^{-1} M_x \Delta t + C M^{-1} M_y \Delta t\Big) \Delta P = B\big(M^{-1} R_u \Delta t\big) + C\big(M^{-1} R_v \Delta t\big) + R_p. \tag{4.3.18}$$

We mention that the discretization has been performed by means of orthonormal basis, a choice that favourably affects the previous expression,

$$\Big(A + BIM_x\Delta t + CIM_y\Delta t\Big)\Delta P = B\big(IR_u\Delta t\big) + C\big(IR_v\Delta t\big) + R_p. \quad (4.3.19)$$

4.3.2 Numerical Results

We now illustrate the convergence properties of the semi-implicit scheme we have just presented. We first considered the Kim and Moin and the travelling waves model problems to define the behaviour with respect to the space-time discretization process. The double shear layer problem has also been solved for the purpose of validation.

Time-Space Convergence

In this section results of convergence studies for the above described DG *ASIRK* scheme are presented. The order of the algorithm is estimated first by means of the Kim and Moin problem, see [32], in which a diffusion of the wave field can mainly be observed and then by a similar case in which along with the diffusion towards homogeneity we have the traveling of the waves themselves, see [38]. The error can be expressed by the following standard expression

$$E \approx C_1 h^p + C_2 \Delta t^k \quad (4.3.20)$$

where p defines the rate of convergence in space while k in time. The definition of these values are not straightforwardly achieved in the case of a component, either the spatial or the temporal, being predominant. In this matter we outline the fact that for these problems the overall error is dominated by the spatial error and this makes the accuracy in time more critical to be evaluated.

Kim and Moin test case

This test case has been proposed by Kim and Moin and it considers the Navier-Stokes equations problem inside the unit square domain $\Omega = (0.25, 1.25)\times(0.5, 1.5)$, with the analytical solution provided in the following

$$\begin{aligned} u &= -\cos(2\pi x)\sin(2\pi y)e^{-8\pi^2\nu t}, \\ v &= \ \ \sin(2\pi x)\cos(2\pi y)e^{-8\pi^2\nu t}, \\ p &= -0.25(\cos(4\pi x) + \cos(4\pi y))e^{-16\pi^2\nu t}, \end{aligned} \quad (4.3.21)$$

with Reynolds number equal to 100 and Dirichlet boundary conditions which set $u = 0\ \forall (x, y) \in \Gamma$ and $v = -\sin(2\pi x)e^{-8\pi^2\nu t}$ for $y_\Gamma = 0.5, 1.5$ and $v = \cos(2\pi y)e^{-8\pi^2\nu t}$ for $x_\Gamma = 0.25, 1.25$. In Tab. 4.3.1 we show the error in norm $L^1(\Omega)$ for the pressure and the velocity along the $x-$axis for finer and finer grids, whose step size h has been successively halfed. The trials are related to polynomial order ranging from one to six and RK schemes of the second or the third order. The rate of convergence can be observed to be nearly in accordance with the expected theoretical values. The time step of these runs has been defined by means of relations accounting for the diffusive and the advective behaviour, for each order of approximation, such as

$$\Delta t \leq \frac{\Delta x^2}{2n+1},$$

being n the polynomial order and Δt and Δx the steps in time and in space. The temporal accuracy characterization requires instead the evaluation of the exponent k in the equation (4.3.20). The frequent predominance of the spatial dynamic may be overcome by using a very fine grid for which the spatial discretization becomes less significant, perhaps allowing to outline the time changes. Another attempt in this direction, we suggest may be provided by the following procedure: we first compute the field for a given mesh with a very little time step for which the leading error should be the one in space, than for runs with larger time step on the same mesh this error is suitably penalised. In this way the temporal behaviour should be revealed, the Tab. 4.3.2 contains the data related to such a strategy, the rate of convergence both for the pressure and the velocity results are shown to be equal to one, although the use of the third order RK scheme.

Traveling waves test case

The following exact traveling wave solution of the NS equations holds

$$\begin{aligned} u(x, y, t) &= 1 + 2\cos(2\pi(x - t))\sin(2\pi(y - t))e^{-8\pi^2\nu t} \\ v(x, y, t) &= 1 - \sin(2\pi(x - t))\cos(2\pi(y - t))e^{-8\pi^2\nu t} \\ p(x, y, t) &= -(\cos(4\pi(x - t)) + \cos(4\pi(y - t)))e^{-16\pi^2\nu t}, \end{aligned}$$

with $\mathrm{Re} = 100$ on a doubly periodic unit square. The Tab. 4.3.3 shows the error behaviour for different time steps, in particular the scheme seems to be limited to the first order, as already pointed out precedengly. The

Table 4.3.1: Convergence rate for the Kim and Moin Test Case: DG approximation in $\mathbb{P}^n$ plus $ASIRK - 3B(\cdot,\cdot)$.

$\mathbb{P}^n$	h	L^1_p-error	Order p	L^1_u-error	Order u
1	8×8	0.20e-1	-	0.38e-1	-
$(2,2)$	16×16	0.55e-2	1.85	0.86e-2	2.14
	32×32	0.13e-2	2.08	0.20e-2	2.10
	64×64	0.34e-3	1.93	0.51e-3	1.97
2	4×4	0.25e-1	-	0.68e-1	-
(3,3)	8×8	0.22e-2	3.50	0.88e-2	2.94
	16×16	0.27e-3	3.02	0.11e-2	3.00
3	4×4	0.26e-2	-	0.81e-2	-
$(3,3)$	8×8	0.17e-3	4.07	0.52e-3	3.96
	16×16	0.12e-4	3.82	0.31e-4	4.06
4	4×4	0.32e-3	-	0.13e-2	-
$(3,3)$	8×8	0.19e-4	4.07	0.44e-4	4.88
	16×16	0.58e-5	1.71	0.12e-5	5.19
5	4×4	0.67e-4	-	0.15e-3	-
$(3,3)$	8×8	0.17e-5	5.30	0.21e-5	6.15
6	4×4	0.46e-4	-	0.21e-4	-
$(3,3)$	8×8	0.58e-6	6.30	0.15e-6	7.12

increase of the order can be noticed for time steps values approaching the reference, in agreement with the error evaluation above exposed, the temporal dynamics is newly overshadowed. Different orders of approximation have been considered, with additive Runge-Kutta of order two and three, they all gave a first order accuracy in time. We mention that these simulations are characterized by a very small residual on the continuity equation, almost at the outset it assumes values of order 10^{-6} at worst, with that related to the momentum equations some order higher. Furher verification has been led even exploiting very fine grids, the results are in accordance with those just presented, only the errors of the 128×128 grid in Tab. 4.3.4 are here reported.

Table 4.3.2: Time accuracy for the Kim and Moin problem on a 16×16 grid and $RK\,(3,3)$, reference time step $\Delta t = 1e-5$

$\mathbb{P}^n$	Δt	L^1_p-error	Order p	L^1_u-error	Order u
1	1e-3	0.25e-3	-	0.27e-3	-
	5e-4	0.12e-3	1.05	0.13e-3	1.05
	2.5e-4	0.63e-4	0.93	0.67e-4	0.96
	1.25e-4	0.30e-4	1.07	0.32e-4	1.06
	6.25e-5	0.13e-4	1.09	0.14e-4	1.19

Double Shear Layer problem

This problem involves a doubly periodic pair of shear layers, the domain of this inviscid NS test is provided by the square $\Omega = (0, 2\pi) \times (0, 2\pi)$ and it is endowed of the following initial conditions,

$$u(x,y,0) = \left\{ \begin{array}{ll} \tanh\left(\frac{2y-\pi}{2\rho}\right) & \text{if } y \leq \pi, \\ \tanh\left(\frac{3\pi-2y}{2\rho}\right) & \text{if } y > \pi, \end{array} \right\}$$
$$v(x,y,0) = \delta \sin(x),$$

with parameters $\rho = \frac{\pi}{15}$ and $\delta = 0.05$. Numerical accuracy is assessed in qualitative way by looking at conservation of the kinetic energy and of the enstrophy, (*i.e.* one-half the square of the vorticity). At this aim the Tab. 4.3.5 and the Tab. 4.3.6 report the values of these quantities for order of approximation of one and three. The data obtained for this problem when solving by means of a full implicit scheme with the jacobian matrices computed analitically, without any approximation, are also listed for the sake of comparison with the semi-implicit strategy approach. The conservation can be estimated through the relative percentage provided for each trial, the value is clearly refered to the variable itself at $t = 0$. The behaviour can also be appreciated in Fig. 4.3.1. The contours of Fig. 4.3.2 allow to appreciate the accuracy of higher order schemes, the $\mathbb{P}^3$ and $\mathbb{P}^5$ are compared at the istant time of 4 seconds and at 8 seconds. The dicreasing of spurious structures is observed.

Table 4.3.3: Convergence rate in time for the traveling waves problem, order of approximation $\mathbb{P}^n$, $ASIRK(\cdot,\cdot)$, grid $(\cdot \times \cdot)$.

$\mathbb{P}^n$	Δt	L^1_p-error	Order p	L^1_u-error	Order u
ref $\Delta t = 1e-5$					
	1e-3	0.29e-3	-	0.34e-3	-
	5.e-4	0.14e-3	1.05	0.17e-3	1.00
$\mathbb{P}^1$	2.5e-4	0.71e-4	0.97	0.85e-4	1.00
(2,2)	1.25e-4	0.34e-4	1.06	0.40e-4	1.08
8x8	6.25e-5	0.15e-4	1.17	0.18e-4	1.15
	3.125e-5	0.63e-5	1.25	0.75e-5	1.26
	1.5625e-5	0.16e-5	1.97	0.20e-5	1.90
ref $\Delta t = 2.5e-5$					
2	1e-3	0.48e-5	-	0.34e-5	-
(3,3)	5e-4	0.36e-6	3.73	0.16e-5	1.08
	1e-4	0.97e-7	-	0.25e-6	-
	5.e-5	0.34e-7	1.51	0.84e-7	1.57
1	1e-3	0.57e-3	-	0.27e-3	-
(3,3)	5e-4	0.28e-3	1-02	0.13e-3	1.04
	2.5e-4	0.13e-3	1.10	0.65e-4	1.00
	1.25e-4	0.61e-4	1.09	0.29e-4	1.16
	6.25e-5	0.24e-4	1.34	0.12e-4	1.26
	3.125e-5	0.69e-4	1.79	0.32e-5	1.90

Table 4.3.4: Time accuracy for traveling waves problem on a very fine mesh.

$\mathbb{P}^n$	Δt	L^1_p-error	Order p	L^1_u-error	Order u
ref $\Delta t = 1.25e-5$					
$\mathbb{P}^1$−3,3	1e-4	0.33e-3	-	0.79e-5	-
128x128	5e-5	0.14e-3	1.23	0.35e-5	1.17

Table 4.3.5: Enstrophy conservation implicit vs semi-implicit

	T	Implicit	Δ%	Semi-implicit	Δ%
$\mathbb{P}^1$	0	2.02323	-0.00	2.01784	-0.00
	4	1.92202	-5.74	1.88568	-6.54
	8	1.54202	-24.37	1.49457	-25.93
$\mathbb{P}^3$	0	2.02790	-0.00	2.02788	-0.00
	4	2.03051	+0.12	2.02903	-0.05
	8	1.95911	-3.39	1.94808	-3.9

Table 4.3.6: Kinetic Energy conservation implict vs semi-implicit

	T	Implicit	Δ%	Semi-implicit	Δ%
$\mathbb{P}^1$	0	0.867912	-0.00	0.867917	-0.00
	4	0.867579	-0.03	0.867317	-0.06
	8	0.863875	-0.46	0.863536	-0.50
$\mathbb{P}^3$	0	0.867917	-0.00	0.867917	-0.00
	4	0.867950	$4 \cdot 10^{-3}$	0.867916	$-1 \cdot 10^{-4}$
	8	0.867789	0.01	0.867863	$-6 \cdot 10^{-3}$

Figure 4.3.1: Conservation satisfaction for the kinetic energy and for the enstrophy for the double shear layer problem. Implicit-semi implicit comparison for polinomial order 1,3,5.

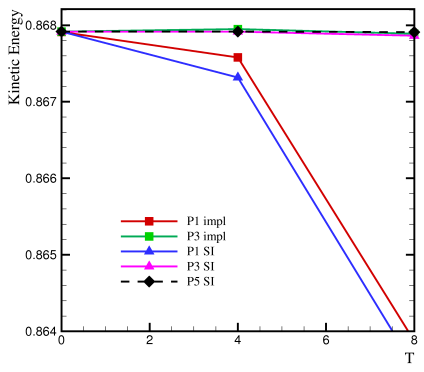

(a) Kinetic Energy Conservation

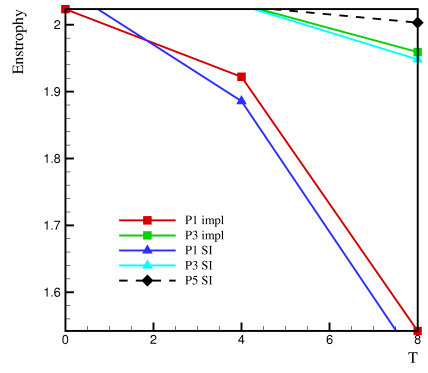

(b) Enstrophy conservation

Figure 4.3.2: Vorticity lines for a 64×64 grid, levels from -7 to 7 by 20

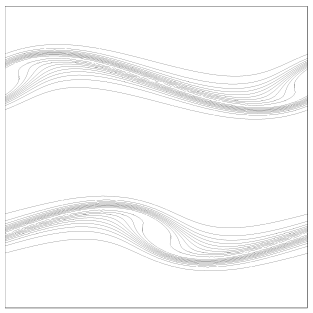

(a) $\mathbb{P}^3$, T=4s

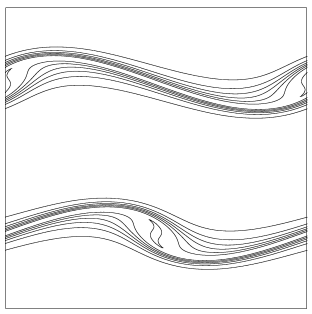

(b) $\mathbb{P}^5$, T=4s

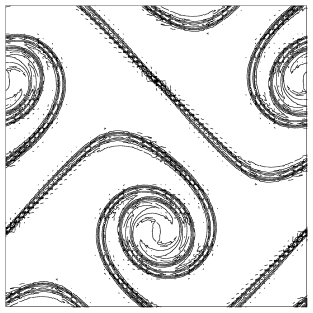

(c) $\mathbb{P}^3$ T=8s

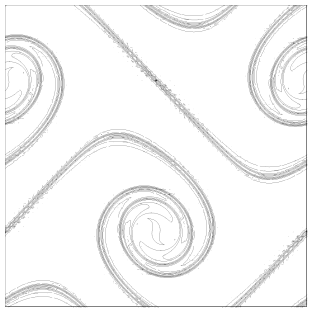

(d) $\mathbb{P}^5$ T=8s

Chapter

5 Conclusions

A spectral discontinuous Galerkin scheme has been presented and shown to achieve highly accurate solutions along with interesting computational performances. The use of tensorial nodal basis functions in co-located elements along with a p- multigrid scheme accomplished such an aim. The co-location strategy resorting to Gauss nodes despite not being the optimal choice from an approximation point of view proved to stem in a more reliable and robust behaviour. The definition of the smoothness level remains a critical point especially for the Gauss-Lobatto choice. This set can be advised for the solution in zones far away from strong changes, where they can ensure the better accuracy-efficiency trade-off. The definition of an algorithm for hybrid grids is the subject of present and nearly future works, already implemented although not described here.

A new semi-implicit INS solution algorithm has been devised resorting to an unusual discretization approach. The interlink between the pressure and the velocity field is obtained entailing the minimum level of implicitness and making the exchange of informations towards convergence being available and used as soon as they are computed. The discontinuity evolution provides the mean for the variables evolution. The algorithm does not involve the introduction of approximations, as neither linearizations nor perturbations have been required, nor spurious boundary conditions are needed. The convergence study shows the expected order for the spatial error, meantime the temporal accuracy seems to be limited to the first order. A peculiar characteristic is the sudden achievement of an almost vanishing continuity residual which someway complicates the evolution of the error itself, maybe preventing the achievement of the right order. However the scheme demonstrated to be able to reach good solution field, we just mention the quality of the double shear vorticity field. Nonethless we remark the memory saving. The behaviour is still under investigation, the propagation of the initial error is one of the aspect we are studing.

Bibliography

[1] D. N. Arnold, F. Brezzi, B. Cockburn, and D. Marini, *Unified analysis of discontinuous Galerkin methods for elliptic problems*, SIAM J. Numer. Anal., 39 (2001), pp. 1749–1779.

[2] F. Bassi and S. Rebay, *A high-order accurate discontinuous finite element method for the numerical solution of the compressible Navier-Stokes equations*, J. Comput. Phys., Vol.131, pp. 267-279 (1997).

[3] ——, *High-order accurate discontinuous finite element solution of the 2D Euler equations*, J. Comput. Phys., Vol.138, pp. 251-285 (1997).

[4] F. Bassi, A. Crivellini, S. Rebay and M. Savini, *Discontinuous Galerkin solution of the Reynolds-averaged Navier-Stokes and $k-\omega$ turbulence model equations*, Computers and Fluids 34 (2005) pp. 507-540.

[5] F. Bassi, A. Crivellini, D.A. Di Pietro, and S. Rebay, *An implicit high-order discontinuous Galerkin for steady and unsteady incompressible flows*, Computer and Fluids 36, pp. 794–815 (2006).

[6] ——, *An artificial compressibility flux for the discontinuous Galerkin approximation of the incompressible Navier-Stokes equations*, J. Comp. Phys., 218, pp. 1529–1546 (2007).

[7] F. Bassi, A. Ghidoni, S. Rebay and P. Tesini, *High-order accurate p-multigrid discontinuous finite element solution of the Euler equations*, J. Numer. Meth. Fluids

[8] W.L. Briggs, Van E. Henson and S.F. Cormick, *A Multigrid Tutorial*, 2nd edition, Siam (2000).

[9] D.L. Brown, R. Cortez and M.L. Minion, *Accurate Projection Methods for the Incompressible Navier-Stokes equations*, J. Comp. Phys., 168, pp. 464–499 (2001).

[10] E. Burman and M. A. Fernández, *A finite element method with edge oriented stabilization for the time-dependent Navier-Stokes equations: Space discretization and convergence*, Num. Math., (2005).

[11] M.H. Chen, B. Cockburn and F. Reitich, *High-order RKDG Methods for Computational Electromagnetics*, J. Comp. Phys., 22 and 23, pp. 205–226 (2005).

[12] P.G. Ciarlet, *Finite Element Method for Elliptic Problems*, no. 40 in Applied Mathematics, Siam 2002.

[13] B. Cockburn, G. Kanschat, and D. Schötzau, *The local discontinuous Galerkin method for the Oseen equations*, Math. Comp., 73 (2003), pp. 569–593.

[14] ——, *The local discontinuous Galerkin method for linearized incompressible fluid flow: a review*, Computers & Fluids, 34 (2005), pp. 491–506.

[15] B. Cockburn, G. Kanschat, D. Schötzau, and C. Schwab, *Local discontinuous Galerkin methods for the Stokes system*, SIAM J. Numer. Anal., 40 (2002), pp. 319–343.

[16] B. Cockburn and C.W. Shu, *Runge-Kutta Discontinuous Galerkin Methods for the Convection-Dominated Problems*, J. Comp. Phys., 16, pp. 173–261 (2001).

[17] G. Dhatt and G. Touzot, *The Finite Element Method Displayed*, Wiley, 1984

[18] M. Dubiner, *Spectral methods on triangles and other domains*, J. Sci Comp., 6 (1991), pp-345

[19] A. Ern and J. L. Guermond, *Theory and Practice of Finite Elements*, no. 159 in Springer Series in Computational Mathematics, Springer-Verlag, Berlin, 2004.

[20] C. Eskilsson and S. Sherwin, *An introduction to spectral/hp element methods for hyperbolic problems*, Lecture Series 2006-01, von Karman Institute for Fluid Dynamics.

[21] P. Gervasio, F. Saleri and A. Veneziani, *Algebraic fractional-step schemes with spectral methods for the incompressible Navier-Stokes equations*,J. Comput. Phys., 214 (2006), pp. 347-365.

[22] F.X. Giraldo, *High-order triangle-based discontinuous Galerkin methods for hyperbolic equations on a rotating sphere*,J. Comput. Phys., 214 (2006), pp. 447-465.

[23] F.X. Giraldo and T. Warburton, *A nodal-triangle based spectral element method for the shallow water equations on the sphere*, J. Comput. Phys., 207 (2005), pp. 129–150.

[24] V. Girault and P.-A. Raviart, *Finite Element Methods for Navier-Stokes Equations*, vol. 5 of Springer Series in Computational Mathematics, Springer-Verlag, Berlin, 1986.

[25] M. A Girault and B.-A. Wingate and R. E. Vincent, *An Algorithm for Computing Fekete Points in the Triangle* , SIAM J. Numer.Anal., vol. 38, no. 5, pp. 1707–1720 (2000).

[26] P.M. Gresho and R.L. Sani, *Incompressible Flow and the Finite Element Method*, vol. 1 Advection-Diffusion, vol. 2, John Wiley & Sons, Ltd., 2000

[27] J. L. Guermond, P. Minev and J. Shen, *An overview of projection method for incompressible flows*, no. 195, Computs. Methods Appl. Mech. Engrg. (2006), pp. 6011-6045.

[28] J. L. Guermond, P. Minev and J. Shen, *Error analysis of Pressure-Correction schemes for the time dependent Stokes equations with open boundary conditions*, SIAM J. Numer. Anal., 43 (2005), pp. 239–258.

[29] J. L. Guermond and L. Quartapelle, *Calculation of Incompressible Viscous Flows by an Unconditionally Stable Projection FEM*, J. Comput. Phys., 132 (1997), pp. 12-33.

[30] J.S. Hesthaven, *From Electrostatics to Almost Optimal Nodal Sets for Polynomial Interpolation in a Simplex*, SIAM J. Numer. Anal., 35, No. 2, (1998), pp. 655–676.

[31] G. E. Karniadakis and S. Sherwin, *Spectral/hp Elemnt Methods for Computational Fluid Dynamics*, Numerical Mathematics and Scientific Computation, Oxford Science Pubblications, 2005.

[32] J. Kim and P. Moin, *Application of a fractional step method to the incompressible Navier-Stokes equations*, J. Comput. Phys., 59 (1985), pp. 308-323.

[33] R.M. Kirby, T.C. Warburton, I. Lomtev and G.E. Karniadakis, *Discontinuous Galerkin spectral/hp method on hybrid mesh*, Applied Numerical Mathematics, 33 (2000),pp. 393–405.

[34] L. Jamenson, *AMR vs High Order Scheme* , J. Comput. Phys., 18 (2003)

[35] H.P. Langtangen, K.A. Mardal and R. Winther, *Numerical Methods for Incompressible Viscous Flow*, Advances in water Resources, 25 (2002), pp. 1125-1146.

[36] J.-G. Liu and C.-W. Shu, *A high-order discontinuous Galerkin method for 2D incompressible flows*, J. Comput. Phys., 160 (2000),pp. 577–596.

[37] D.J Mavriplis and A. Jameson, *Multigrid solution of the Navier-Stokes equations on triangular meshes*, AIAAJ. 28,No.8,1415 (1990).

[38] M.L. Minion and D.L. Brown, *Performance of Under-resolved Two.Dimensional Incompressible Flow Simulation II*, J. Comput. Phys., 138 (1997),pp. 734–765.

[39] P. Nithiarasu and O.C. Zienkiewicz, *Analysys of an explicit and matrix free fractional-step method for incompressible flows*, Comput. Methods Appl. Mech. Engrg, 195 (2006),pp. 5537–5551.

[40] R. Pasquetti and F. Rapetti, *Spectral Element Methods on Unstructured Meshes Comparisons andRecent Advances*, J. of Scientific Computing Vol.27 (2006).

[41] ——, *Spectral elemnt methods on triangles and quadrilaterals; comparisons and applications*,J. Comput. Phys., 198 (2004),pp. 349–362.

[42] A. Quarteroni, F. Saleri and A. Veneziani, *Analysis of the Yosida method for the incompressible Navier-Stokes equations*, J. Math Pures Appl. 78, pp. 473-503 (1999).

[43] A. Quarteroni, F. Saleri and A. Veneziani, *Factorization methods for the numerical approximation ofthe Navier-Stokes equations*, Comput. Methods Appl. Mech. Engrg. 188(1-3), pp. 505-526 (2000).

[44] A. Quarteroni and A. Valli, *Numerical Approximation of Partial Differential Equations*, no. 23 in Springer Series in Computational Mathematics, Springer-Verlag, Berlin, 1994.

[45] R. Radespiel and R.C. Swanson, *'An investigation on Cell Centered and Cell Vertex Multigrid schemes for the Navier-Stokes equations '*,AIAA Paper No89-0453, (1989, unpublished).

[46] S.J. Sherwin and G.E. Karniadakis, *A triangular spectral element method; applications to the incompressible Navier-Stokes equations*, Computer Methods in Applied Mechanics and Engineering 123, 1995, pp. 189-229.

[47] P. Sŏlín, K. Segeth and I. Doležel, *Higher Order Finite Element Methods*, Studies in Advanced Mathemathics, Chapman and Hall CRC, Florida, 2004.

[48] R.J. Spiteri and S.J.Ruuth, *A New Class of Optimal High-Order Strong Stability-Preserving Time Discretization Method* , SIAM J. Numer. Anal., 40 (2002), pp. 469–491.

[49] M.A. Taylor, B.A. Wingate and R.E. Vincent, *An algorithm for computing Fekete points*, SIAM J. Numer. Anal., 38 (2000), pp. 1707–1720.

[50] Xiaolin Zhong, *Additive Semi-Implicit Runge-Kutta Methods for Computing High-Speed Nonequilibrium Reactive Flows*, J. Comput. Phys., 128, pp. 19-31 (1996)